Elena – Daniela Ion

SOLUTION SYNTHESIS OF NANOPARTICLES IN MULTICOMPONENT OXIDE SYSTEMS

Doctoral Dissertation

SINTEZA NANODELCEV V VEČKOMPONENTNIH OKSIDNIH SISTEMIH IZ RAZTOPIN

Doktorska disertacija

Supervisor: Asst. Prof. Dr. Barbara Malič

Co-supervisor: Prof. Dr. Iztok Arčon

June 2008

MEDNARODNA PODIPLOMSKA ŠOLA JOŽEFA STEFANA
JOŽEF STEFAN INTERNATIONAL POSTGRADUATE SCHOOL
Ljubljana, Slovenia

Index

Abstract

The study of $PbZrO_3$ (PZ), $PbTiO_3$ (PT) and $La_2Zr_2O_7$ (LZ) prepared by alkoxide sol-gel synthesis is described.

PZ and PT sols were prepared from lead acetate, zirconium and titanium n-butoxide, in n-butanol and hydrolysed with R_w (molar ratio of water per lead acetate) between 2 and 15 in neutral medium and $R_w = 15$ in alkaline medium. Different R_w were used to find the correlations between the hydrolysis conditions, morphology and homogeneity of PZ and PT.

The partial charge of Zr in the partially hydrolysed PZ product is higher than that of Ti in corresponding PT sample, which means that the former is more reactive. The partial charges of the OH groups are similar in all cases, with negative values; therefore the OH groups are nucleophilic enough to initiate further condensation. We assume that condensation stops predominantly due to the steric hindrance.

At low R_w dense and at high R_w porous gel fragments are obtained, and at R_w 15 and alkaline pH about 10 nm sized particles. The organic groups in the former decompose upon heating with intermediate carbonaceous residues, forming a locally reducing atmosphere and segregation of lead from the amorphous matrix. In contrast, the porous structure of R_w 15 powders allows a one-step oxidation of organic groups. The dried PT powders are composed of a porous network of nano-particles regardless of the hydrolysis conditions.

The morphology of the dried powders is retained upon heating. The PZ and PT powders crystallize in perovskite phase upon heating at 700 ^oC and 500 ^oC, respectively.

The LZ sol was prepared from dehydrated lanthanum nitrate and zirconium n-butoxide in 2-methoxyethanol. A strongly exothermic reaction between the nitrates and organic groups yielded a friable, porous powder which crystallized in pyrochlore phase upon heating to 800 ^oC. The powder, heated at 900 ^oC contained 70 nm sized particles and could be sintered to 97.9 % relative density at 1400 ^oC, about 200 ^oC below the usually reported temperatures for air-sintering of this material.

The structural evolution from the sol to the amorphous dried and heat treated PZ and LZ powders was investigated. In the PZ sol, the lead environment is dominated by two Pb-O-Zr links, while the Zr environment is populated by six Zr-O-Zr links. In the dried powders, one of the two Pb-O-Zr links is retained while Zr - Zr correlations are retained regardless the hydrolysis conditions. In the powder heated at 400 ^oC / 1h there is no Pb-Zr correlation, while the Zr - Zr correlations remain almost unchanged.

La environment in both La nitrate solution and LZ sol is similar to that of lanthanum nitrate hydrate. Zr environment is populated by six Zr-O-Zr links and it remains almost unchanged in the transition from the sol to the dried and heated amorphous powder. La-O-Zr links have not been established. Zr local environments are similar in both PZ and LZ sols and amorphous powders. Upon synthesis of the respective sols the Zr-O-Zr links are established and they are stable in the investigated temperature range. In both cases the reaction between individual metal compounds proceeds as a solid-state reaction.

Povzetek

Delo opisuje študij $PbZrO_3$ (PZ), $PbTiO_3$ (PT) in $La_2Zr_2O_7$ (LZ), pripravljenih z alkoksidno sol-gel sintezo.

Sola PZ in PT smo pripravili iz svinčevega acetata, cirkonijevega in titanovega butoksida v n-butanolu in ju hidrolizirali z molskim razmerjem voda / svinčev acetat (R_w) med 2 in 15 v nevtralnem in alkalnem mediju. Namen je bil razumeti zvezo med pogoji hidrolize, morfologijo in homogenostjo PZ in PT.

Delni naboj cirkonija v hidroliziranem solu PZ je višji od delnega naboja titana v PT, kar pomeni, da je PZ bolj reaktiven kot PT. Delni naboj hidroksilnih skupin je tako v PZ kot v PT negativen, kar v obeh primerih omogoča nadaljnjo reakcijo polikondenzacije. Sklepamo, da se polikondenzacija ustavi predvsem zaradi steričnih ovir.

Morfologija prahov PZ je odvisna od pogojev hidrolize: pri R_w 2 nastanejo gosti in pri R_w 15 porozni gelski drobci, medtem ko pri R_w 15 in alkalnem pH delci, veliki okrog 10 nm. Organske skupine v vzorcu, pripravljenem pri nizkem R_w, med segrevanjem razpadejo v dveh stopnjah, pri čemer vmesni razpadni produkti ustvarijo lokalno redukcijsko atmosfero, ki omogoči segregacijo kovinskega svinca iz amorfne matrice. Nasprotno organske skupine v vzorcih, pripravljenih pri R_w 15, razpadejo v eni stopnji. Sušeni prahovi PT so sestavljeni iz nanodelcev ne glede na pogoje hidrolize.

Prahovi ohranijo tudi po segrevanju morfologijo sušenih prekurzorjev. Prahova PZ in PT po segrevanju pri 700 ^oC oziroma 500 ^oC kristalizirata v perovskitni fazi.

Sol LZ je bil pripravljen iz dehidratiziranega lantanovega nitrata in Zr butoksida v 2-metoksietanolu. V močno eksotermni reakciji med nitratnimi in organskimi skupinami je nastal drobljiv, porozen prah, ki je po segrevanju pri 800 ^oC kristaliziral v piroklorni fazi. Prah, segret pri 900 ^oC, je vseboval 70 nm velike delce. Keramika je dosegla 97.9 % relativno gostoto po sintranju pri 1400 ^oC, kar je približno 200 ^oC nižje od običajnih temperatur sintranja za to keramiko.

Nadalje smo se v delu namenili raziskati lokalno urejenost v solih, amorfnih sušenih ter segretih prahovih PZ in LZ. V solu PZ sestavljata okolico svinca dve vezi Pb-O-Zr, medtem ko je v okolici Zr šest vezi Zr-O-Zr. V sušenem prahu se ena od vezi Pb-O-Zr ohrani, vezi Zr-O-Zr pa ostanejo nespremenjene. V prahu, segretem pri 400 ^oC, ne zaznamo več zveze med Pb in Zr, medtem ko so vezi Zr-O-Zr skoraj nespremenjene.

Okolica La atomov v raztopini La nitrata in v solu LZ je podobna okolici samega lantanovega nitrata hidrata. Okolico Zr v solu LZ sestavlja šest Zr-O-Zr vezi. Podobno okolico Zr atomov prah LZ ohrani tudi po sušenju in segrevanju pri 500 ^oC. Vezi La-O-Zr nismo opazili.

Lokalna urejenost Zr atomov v solih in amorfnih prahovih PZ in LZ je podobna. Med sintezo solov se ustvarijo vezi Zr-O-Zr, ki se ohranijo tudi v amorfnih prahovih. V obeh primerih poteče kristalizacija ciljne spojine z reakcijo med posameznima kovinskima oksidoma, torej z reakcijo v trdnem stanju.

’’’’’’’

Abbreviations

Acronyms

2MOE	=	2-Methoxyethanol
ACC	=	Accelerating Voltage
CIP	=	Cold Isostatic Pressing
DTA	=	Differential Thermal Analysis
EGA	=	Evolved Gas Analysis
EXAFS	=	Extended X-ray Absorption Fine Structure
FE-SEM	=	Field Emission – Scanning Electron Microscopy
ICP-AES	=	Inductive Coupled Plasma – Atomic Emission Spectrometry
iPrOH	=	Isopropanol
IR	=	Infra Red Spectrometry
JCPDS	=	Joint Committee on Powder Diffraction Standards
LN	=	Lanthanum Nitrate
LZ	=	Lanthanum Zirconate
MPB	=	Morphotropic Phase Boundary
NMR	=	Nuclear Magnetic Resonance
P.I.	=	Polydispersity Index
PCS	=	Photon Correlation Spectroscopy
$Pb(OAc)_2$	=	Lead Acetate
PT	=	Lead Titanate
PZ	=	Lead Zirconate
PZT	=	Lead Zirconate Titanate
SSA	=	Specific Surface Area
SEM	=	Scanning Electron Microscopy
TG	=	Thermogravimetry
$Ti(nOBu)_4$	=	Titanium n-Butoxide
WD	=	Working Distance
XANES	=	X-ray Absorption Near Edge Spectroscopy
XRD	=	X-ray Diffraction
YSZ	=	Yttria Stabilised Zirconia
$Zr(nOBu)_4$	=	Zirconium n-Butoxide

Symbols

δ	=	Partial charge
D_{10}	=	10^{th} percentile of the particles size distribution determined by laser granulometry
D_{50}	=	Median particle size determined by laser granulometry
D_{90}	=	90^{th} percentile of the particles size distribution determined by laser granulometry
d_{BET}	=	Diameter calculated from SSA
D_X	=	Theoretical density
F_{ag}	=	Agglomeration factor
ρ	=	Density
ρ_r	=	Relative density
R_w	=	Molar ratio of water per lead acetate
σ^2	=	Debye Waller factor
χ_i	=	electronegativity of an atom i in a molecule
χ_i^o	=	electronegativity of a neutral atom

1 Introduction

"Solution synthesis" includes a wide group of synthetic processes used to prepare advanced materials. Basically such synthesis should ensure homogeneity on the molecular or nanometer level, thus greatly reducing the diffusion distances compared to those of the solid state synthesis and resulting in shorter reaction times and lower reaction temperatures.

In solution synthesis of multicomponent oxide powders starting components are usually dissolved and react in liquid phase forming an intermediate product. This is then transformed to a solid precursor which is usually amorphous, and its morphology depends on the choice of the reactants and the reaction conditions. In subsequent heat-treatment steps, which may include drying, thermolysis of functional organic groups, reaction of component species, and crystallization, a crystalline product with the stoichiometry of the target material is obtained, and usually at a lower temperature than those required for the solid-state synthesis (Livage *et al.*, 1990; Brinker *et al.*, 1990; Malic, 2003).

1.1 Alkoxide based sol-gel route for powder synthesis

In the last twenty years, there has been an intensive research of the solution synthesis of ceramic powders. The alkoxide–based sol-gel processing has attracted attention due to potential advantages of control of stoichiometry, homogeneity, chemical purity and lower particle size in comparison to the solid-state synthesis (Livage *et al.*, 1988; Brinker *et al.*, 1990; Hench *et al.*, 1990; Chandler *et al.*, 1993). Metal alkoxides, the key precursors of this synthesis route, have the following molecular formula: $M(OR)_n$
where M = metal atom, OR = alkoxide group and R an alkyl or aryl group, n = oxidation state of the M.

Transition metal alkoxides are known for their very high reactivity toward nucleophilic reagents such as water which is explained (Livage *et al.*, 1988) by:

- their low electronegativity which leads to a high electrophilic character of the metals,
- the possibility of the coordination expansion.

Therefore they must be handled very carefully, in a dry environment, in order to avoid uncontrolled reaction with water.

The hydrolysis of metal cations in aqueous solution has been extensively studied since the beginning of the 20th century (Brinker *et al.*, 1990).

The hydrolysis reaction occurs by the addition of a water molecule to the metal alkoxide with the formation of a reactive M-OH hydroxo group. A three step mechanism is proposed in the literature (Eq. 1.1-1) (Livage *et al.*, 1988).

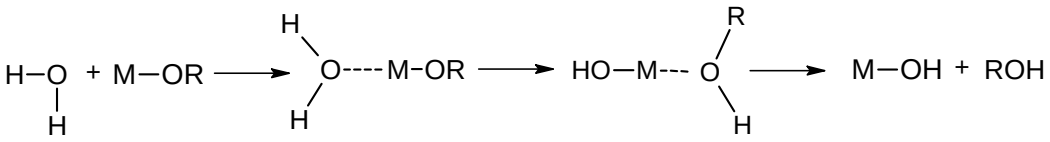

Eq. 1.1-1

The first step is a nucleophilic addition of the water molecule to the positively charged metal atom M. The next step is a transition state where the coordination of M has increased by one. Next, a proton is transferred from the water molecule to the negatively charged oxygen of the OR leading to an intermediate state and in the third step the leaving group is the most positively charged species.

The charge distribution governs the thermodynamics of this reaction which is highly favoured when:

- the nucleophilic character of the entering molecule and the electrophilic character of the metal atom are strong,
- the nucleofugal character of the leaving molecule is high.

On the other hand the nucleophilic substitution depends also on the non-saturated coordination of the metal atom; if N and n are maximum coordination number of the metal in a metal oxide and its oxidation state, respectively, the larger the (N-n), the lower the activation energy of the nucleophilic addition; and on the ability of the proton to be transferred to the intermediate: the more acidic the proton the lower the

activation energy associated with the transfer.

The second chemical reaction is condensation which can occur as soon as hydroxo groups are generated (Eq. 1.1-2).

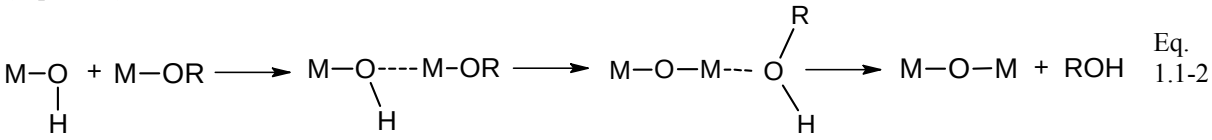

Eq. 1.1-2

The mechanism is basically the same as for hydrolysis with M replacing H in the entering group. Consequently the thermodynamics and kinetics are governed by the same parameters as for hydrolysis. Depending on the experimental conditions three mechanisms are to be considered:

- alcoxolation: a bridging oxo group is formed through the elimination of an alcohol molecule,
- oxolation: a bridging oxo group is formed through the elimination of a water molecule,
- olation occurs, when the full coordination of the metal atom is not satisfied in the alkoxide: a bridging hydroxo group is formed through the elimination of a solvent molecule. This can be either water or alcohol, depending of the water concentration in the medium.

A good rule of thumb for the sol-gel chemist is given in Table 1.1-1. It suggests that, depending on the relative hydrolysis and condensation rates, different products may be obtained: colloids in the case of slow hydrolysis and slow condensation, gels when hydrolysis is fast, and precipitates, when condensation is fast.

Table 1.1-1. Products obtained according to the relative rates of hydrolysis and condensation.

Hydrolysis rate	Condensation rate	Result
Slow	Slow	Colloids/ Solids
Fast	Slow	Polymeric gels
Fast	Fast	Colloidal gel or gelatinous precipitate
Slow	Fast	Controlled precipitation

1.1.1 Homogeneity *vs.* heterogeneity in multicomponent systems

1.1.1.1 Hydrolytic route

In the preparation of multicomponent gels by an alkoxide-based route, comprising A^{2+} and B^{4+} ions, with an overall stoichiometry A/B=1, Kakihana (Kakihana, 1996) proposed the following steps (Figure 1.1-1).

The first step of the synthesis involves mixing of two metal alkoxides, $A(OR)_2$ and $B(OR')_4$, in a suitable organic solvent to prepare a precursor solution. This is followed by the addition of water to obtain a gel. The degree of chemical homogeneity of the resulting gel is strongly affected by the reactivity of each alkoxide species towards hydrolysis. Moreover, chemical reactivity between the two metal alkoxides can lead to formation of a number of new chemical species.

In case (1) (Figure 1.1-1), where no reaction between the two metal alkoxides occurs, chemical homogeneity of the resulting gel will strongly depend upon the reactivity of individual metal alkoxides toward water. When hydrolysis and condensation rates of different metal alkoxides are different, clusters form in the sol, which give rise to inhomogeneities in the resulting gel. When metal alkoxides have very different rates of hydrolysis, segregation of the fastest hydrolysable species occurs during the hydrolysis-condensation process, which in turn makes it difficult to prepare a homogeneous gel with the required stoichiometry. Such problems can be overcome by using chemically modified alkoxides to control the hydrolysis rate of the highly reactive alkoxides. For instance, replacement of one of the alkoxide ligands in $Ti(OC_4H_9)_4$ and $Zr(OC_3H_7)_4$ by acetic acid slows the rate of hydrolysis and condensation, so that the gelation time is increased from a few minutes to a few days (Sanchez *et al.*, 1988).

In case (2) (Figure 1.1-1), the two metal alkoxides react with each other stoichiometrically to form a heterometallic alkoxide with exactly the target A/B ratio according to the following reaction (Eq. 1.1-3):

$$A(OR)_2 + B(OR')_4 \rightarrow AB(OR)_2(OR')_4 \qquad \text{Eq. 1.1-3}$$

The heterometallic alkoxide can then be hydrolysed with a controlled amount of water as if it were a single molecule, thereby favouring the formation of mixed metal-oxygen bonds –A–O–B– between the two metals. Subsequent polymerization may yield a multicomponent gel with the correct stoichiometry. Successful example of this approach includes the synthesis of $BaTiO_3$ (Campion *et al.*, 1991), where the

heterometallic alkoxides produced by the stoichiometric reactions of individual alkoxides, are hydrolysed and by condensation they form homogenous multicomponent gels. This molecular route results in powders having much higher purity and compositional homogeneity and requires lower sintering temperatures than those prepared by other wet chemical methods.

In case (3) (Figure 1.1-1), a mixture of molecular species with different metal stoichiometries is formed, therefore chemical inhomogeneity already exists in the precursor solution. Thus a gel created upon hydrolysis may exhibit heterogeneity depending upon the degree of mixing of the different metallic species and the relative rate of hydrolysis of the individual molecular species formed in the initial precursor solution. The compositional homogeneity is accordingly attained only after high temperature processing.

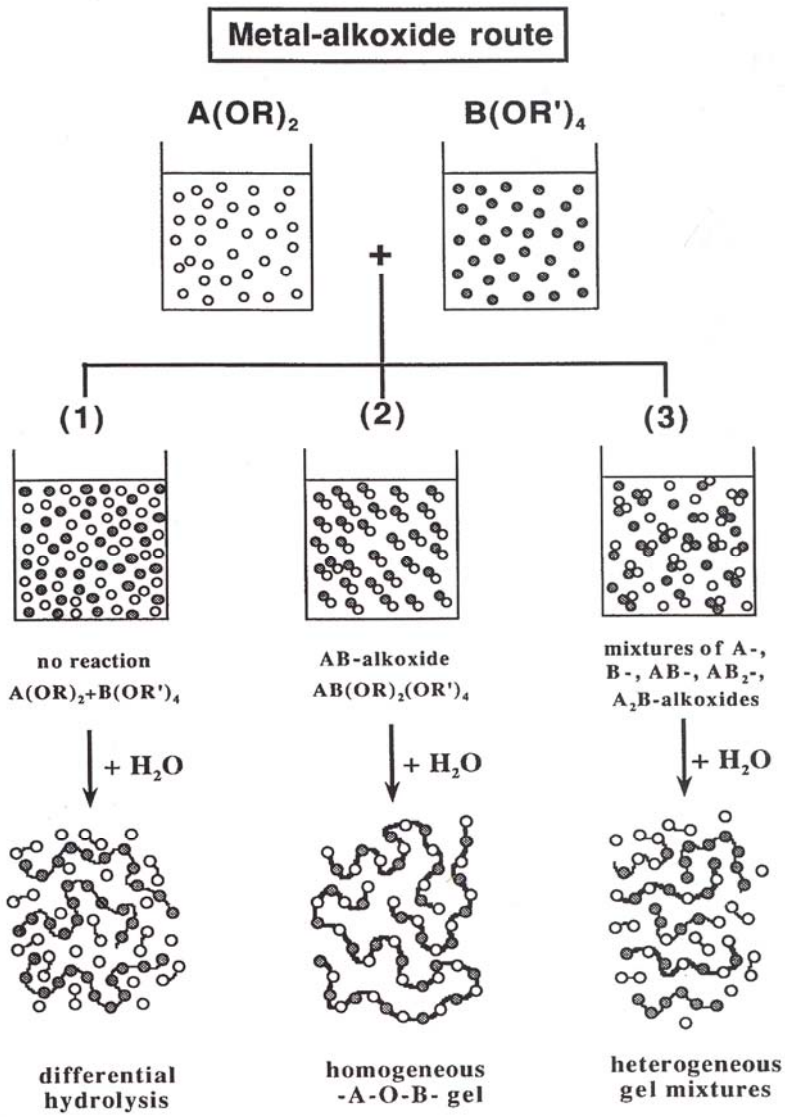

Figure 1.1-1. Effect of precursor characteristics on homogeneity of alkoxide-derived multicomponent gels: (1) A case where no reaction between $A(OR)_2$ and $B(OR')_4$ occurs, but the rate of hydrolysis and condensation is much larger in $B(OR')_4$ than in $A(OR)_2$ resulting in segregation of the B component. (2) A case where a heterometallic (double) alkoxide forms, resulting in a homogenous –A–O–B– gel. (3) A case where a variety of reactions occurs to form a mixture of molecular species with different stoichiometry, causing local heterogeneities in the resulting gel. (from Kakihana, 1996)

Factors affecting the sol-gel process

- Organic ligand

The hydrolysis rate decreases with increasing size of the alkyl groups since the positive partial charge of the metal decreases with the length of the alkyl chain. In the same way the positive partial charge of hydrogen atoms decreases giving rise to a more difficult proton transfer. In addition, the longer and the more branched organic ligands, the higher the sterical hindrance they induce, slowing down both hydrolysis and condensation. A comparison of the morphology of the powders synthesised from the

different precursors hydrolysed at the same conditions i.e. Zr ethoxide, Zr n-propoxide, Zr i-propoxide and Zr n-butoxide showed that the short linear alkyl groups produced fragments with no discernable texture and their gradual coarsening was observed with increasing the size of the alkyl group (Yoldas, 1986a).

- Molecular complexity

Hydrolysis and condensation are strongly dependent on oligomerization. The full coordination of the transition metal is not satisfied in the monomeric alkoxides. As a consequence, the metal increases its coordination number by using its vacant d-orbital to accept oxygen lone pairs from nucleophilic ligands. The degree of association depends on the metal atom. Within a given group, the molecular complexity increases with the atomic size of the metal (Zr>Ti). Molecular complexity depends on the nature of the alkoxy group and it decreases with increasing branching of the –OR group because of the steric hindrance.

The increase of coordination number of the metal atom can be realized either by bridging alkoxide groups and/or by the addition of solvent molecules to reach the stable coordination. By a XANES and EXAFS study of Ti alkoxides Babonneau *et al.* (Babonneau *et al.*, 1988) determined that $Ti(OEt)_4$ and $Ti(^nOBu)_4$ form trimers with alkoxide bridges to increase the Ti coordination number from 4 to 5. Studies of Zr n-butoxide in butanol (Peter *et al.*, 1994) show the formation of dimers with both alkoxide bridges and by the addition of solvent molecules to increase the coordination number of zirconium from 4 to 6.

As a consequence, the condensation of the hydrolysed species proceeds via alcoxolation and oxolation in the case of Ti n-butoxide and very probably initially by olation in the case of Zr n-butoxide, where the solvent molecule is present in the first coordination sphere.

- Catalyst

Acid or base catalysts can influence both hydrolysis and condensation rates and structure of the condensed product. Acids serve to protonate negatively charged alkoxide groups, enhancing the reaction kinetics by producing a better leaving group and eliminating the requirement for proton transfer within the transition state. The ease of protonation of different alkoxide ligands can influence the condensation pathway.

Beside their role as catalysts, acids and bases can also act as electrostatic barriers around particles leading to the interparticles repulsion and decreasing their agglomeration (Lange, 2001).

- Solvent

Metal alkoxides are often dissolved in organic solvents before hydrolysis is performed. These solvents, such as parent alcohol or other alcohols, are often far from being chemically inert with respect to the alkoxide.

The solvent can play two other functions:

- Solvation – by the addition of a protic solvent molecule the metal ion expands its coordination number. Such example is zirconium butoxide. Peter *et al.* (Peter *et al.*, 1994) proposed that the most probable structure is a dimer, which includes beside two alkoxy bridging groups also two solvent molecules, which increase the coordination number of zirconium to 6 (Figure 1.1-2).

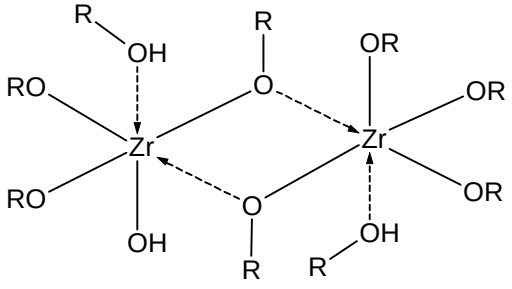

Figure 1.1-2. Proposed structure of a dimeric zirconium alkoxide and coordinated solvent molecules with linear alkyl chains (Peter *et al.*, 1994).

- Chemical modification – by an alcohol-exchange reaction, the alkoxide group is replaced with a less reactive group resulting in a decreased sensitivity of the modified alkoxide towards hydrolysis (Eq. 1.1-4).

$$M(OR)_x + x\ R'OH \longrightarrow M(OR')_x + ROH \qquad \text{Eq. 1.1-4}$$

Such solvent is 2-methoxyethanol. By molecular dynamics investigation (Kuhn *et al.*, 1964) it has been found that the molecule can exist in three conformations having a dihedral angle of 60°, two gauche conformations and one anti conformation (Figure 1.1-3).

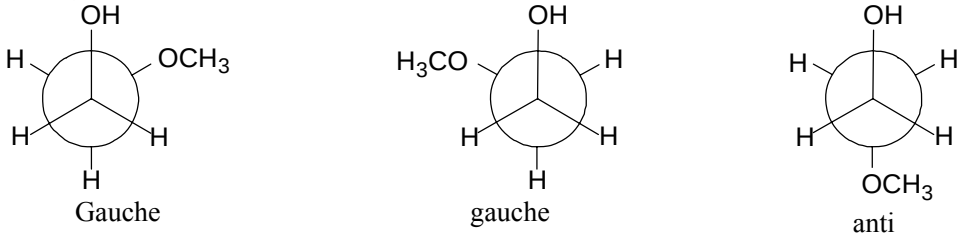

Figure 1.1-3. Conformations of 2-methoxyethanol; X=OCH_3 (Kuhn *et al.*, 1964).

2-Methoxyethanol is widely used as a solvent in ceramic thin films prepared by an alkoxide-based synthesis route, due to the decreased reactivity of the modified metal alkoxides towards hydrolysis (Schwartz, 1997).

- Concentration and temperature

The other external parameters such as concentration and temperature, even though of less importance, may also play a role in the reaction pathway. Several authors have shown that hydrolysis and condensation could be separated by a strong dilution (Livage *et al.*, 1988). In general, an increase of the temperature activates both hydrolysis and condensation reactions.

1.1.1.2 Nonhydrolytic route

In the alkoxide-based sol-gel route, the major problem is to control the rates of hydrolysis and condensation, which are generally too fast, resulting in a loss of microstructural control over the target oxide materials (Brinker *et al.*, 1990). An alternative strategy is provided by nonhydrolytic sol-gel processes, and their molecular chemistry is presented by Vioux (Vioux, 1997).

Nonhydrolytic hydroxylation reactions. An example of such reaction is the thermal decomposition of metal alkoxide (carboxylate) precursors in the temperature range 200-300°C, where the hydroxyl groups are produced via a cyclic elimination mechanism with liberation of alkenes (Shulman *et al.*, 1963). Such an example is aluminium alkoxide (Eq. 1.1-5). This kind of reaction is more relevant to MOCVD (metal-organic chemical vapour deposition), but it is also involved in the thermal degradation of the residual alkoxy groups during the calcination of nonhydrolytic gels into oxides.

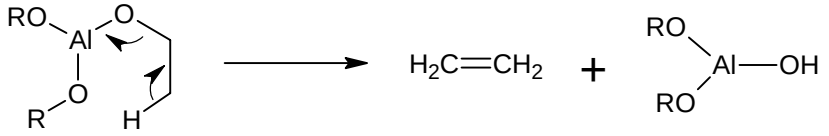

Eq. 1.1-5

Aprotic condensation reaction. In this case the formation of an oxo bridge is provided by the condensation reaction between two different functional groups bonded to two different metal centres, by eliminating a small molecule as follows:

1. Ester elimination. The condensation reaction between metal carboxylates and metal alkoxides (Eq. 1.1-6) is mostly used when metal alkoxides are expensive or unavailable (Budd *et al.*, 1985; Chandler *et al.*, 1993).

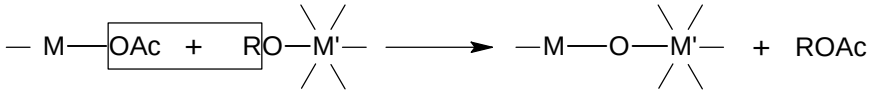

Eq. 1.1-6

2. Ether elimination. By thermolysis (Turova *et al.*, 2002), transition metal alkoxides can react with elimination of an ether molecule and formation of an "oxo" bridge between the metal atoms (Eq. 1.1-7). Such "oxo" bridges represent the building blocks of an oxide network, which is usually obtained only upon further heating.

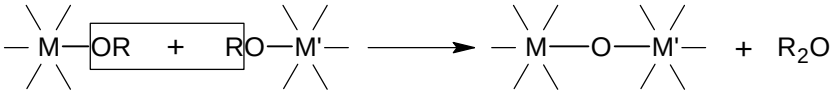

Eq. 1.1-7

Oxo-alkoxide complexes $Ti_7O_4(OEt)_{20}$ and $Nb_8O_{10}(OEt)_{20}$ were obtained as single crystals by spontaneous decomposition upon prolonged storage or heating of solution of $Ti(OEt)_4$ and $NbO(OEt)_3$ (Turova *et al.*, 2002), while $Ce_4O(OPr^i)_{14}$ was obtained by refluxing $Ce_2(OPr^i)_8(Pr^iOH)_2$ in toluene for 1.5 h (Sirio *et al.*, 1997).

A reaction between these species is expected with the formation of M-O-M' bridges. A perfect alternation of such bridge would assure homogeneity, while in reality the homogeneity is dictated by the relative rate of homocondensation (M-O-M and M'-O-M' bridges) towards heterocondensation (M-O-M' bridges) (Vioux *et al.*, 1997).

1.2 Alkoxide based sol-gel synthesis of $Pb(Zr,Ti)O_3$ powder – relevant literature

Lead zirconate titanate $Pb(Zr,Ti)O_3$ (PZT) is a binary solid solution of an antiferroelectric $PbZrO_3$ (PZ) and a ferroelectric $PbTiO_3$ (PT), which exist in orthorhombic and tetragonal phase at room temperature.

PZT ceramics with the morphotropic phase boundary composition, corresponding to Zr/Ti ratio of 53/47 have been widely used because of their excellent piezoelectric and ferroelectric properties (Jaffe *et al.*, 1971).

One of the methods to prepare PZT is the alkoxide-based sol-gel synthesis (Gurkovich *et al.*, 1984; Budd *et al.*, 1985), by which powders, fibres, thin films and monoliths with a controlled compositions and microstructures can be produced (Brinker *et al.*, 1990).

In this synthesis route the reagents are often lead acetate and zirconium and titanium alkoxides and their different reactivity needs to be considered. By the choice of precursors or by varying the hydrolysis conditions not only the powder morphology can be tailored but also the decomposition pathway and the homogeneity of the powder can be affected (Malic *et al.*, 1995, Wu *et al.*, 2000).

By a transmission electron microscopy study, Lakeman *et al.* (Lakeman *et al.*, 1995) demonstrated that when heated at 300 ^oC $Pb(Zr_{0.53}Ti_{0.47})O_3$ thin films were compositionally heterogeneous on the nanoscale, and that during heat treatment at 600 ^oC, compositionally uniform perovskite phase resulted through diffusion processes. Sengupta *et al.* (Sengupta *et al.,* 1995*)* found that Pb cations do not form bonds with Ti and Zr in $PbTiO_3$ (PT) and PZT amorphous powders heated at 375 ^oC and 425 ^oC, respectively; even in the $PbZrO_3$ (PZ) amorphous powder (500 ^oC) where Zr-O-Pb bonds do form, Zr-O-Zr bonds are still present. Feth *et al.* (Feth *et al.*, 2003) found that the local order of metal atoms in amorphous PT, PZ, and PZT was completely different from that in the perovskite structure, but resembled the local order of the individual metal oxides: local environment of lead, zirconium and titanium atoms in amorphous samples corresponded to structures of tetragonal PbO, monoclinic ZrO_2, and of tetragonal TiO_2, respectively. Clustering of Zr species in zirconium-rich PZT is supposed to affect the crystallization to the ferroelectric product, specifically the formation of transitory pyrochlore-type phase (Malic *et al.*, 1999). Also, a preferred Zr homo-condensation in the amorphous precursor powder (Malic *et al.*, 1999) or the 2-methoxyethanol based sol of PZT with a morphotropic phase boundary composition or PZT with a high Zr content of 75/25 was found (Malic *et al.*, 2005; Malic *et al.*, 2006). The authors proposed that during reflux and distillation polynuclear oxo-alkoxide complexes formed in the sol by ether elimination.
Polli *et al.* (Polli *et al.*, 1995) observed the segregation of lead upon rapid heating to 400 ^oC of the PZT (50/50) precursor prepared from lead acetate, zirconium butoxide, titanium propoxide in ethanol, and they avoided it only by a pyrolysis step at 300 ^oC / 1h.

The morphology of the $Pb(Zr_{0.5}Ti_{0.5})O_3$ powder depends on the precursors: gel fragments or soft agglomerates are obtained when propoxide or n-butoxide derived precursors are used, respectively (Kosec *et al.*, 1994). Different catalysts lead to different physical characteristics of $PbTiO_3$ produced using the 2-methoxyethanol route: acid-catalysed gels have a fibrous morphology with a homogenous distribution of constituent metals, while the base-catalysed gels have a highly condensed structure, with a coarse texture and an inhomogeneous cation distribution (Dey *et al.*, 1987).

1.3 Nitrate-modified sol-gel synthesis of $La_2Zr_2O_7$ powder – relevant literature

In the past decade there has been increased interest in preparing lanthanum zirconate because of its many possible applications. Its properties, including high thermal stability, good chemical resistance and low thermal conductivity, make it a candidate material for thermal barrier coatings in gas turbines and diesel

engines (Cao *et al.*, 2004). It has been investigated as a possible host for fluorescence centers (Kido *et al.*, 1991) and for radioactive waste (Bolech *et al.*, 1997), as a high-temperature catalyst (Nair *et al.*, 1999) and as a material that can provide a better understanding of the transport properties in solid-oxide fuel cells (SOFCs), since $La_2Zr_2O_7$ has been detected at the electrode/YSZ interfaces in $LaCoO_3$-, $LaFeO_3$- and $LaMnO_3$-based electrodes (Labrincha *et al.*, 1993; Kuscer *et al.*, 1995; Kuscer *et al.*, 2001).

Different methods, such as hydrothermal synthesis (Chen *et al.*, 1998), the hydrazine method (Matsumura *et al.*, 1997; Ota *et al.*, 1998) and sol-gel techniques (Chen *et al.*, 1998; Rao *et al.*, 2002), have been employed to prepare the LZ powder. We introduced the nitrate-modified alkoxide-based route as an attractive synthesis of LZ powders (Ion *et al.*, 2007b). The starting compounds are lanthanum nitrate, zirconium n-butoxide and 2-methoxyethanol as solvent.

2 Aims and Hypothesis

The advantage of the solution synthesis over the solid-state synthesis should be that the former ensures homogeneity on the molecular or nanometre level, and control of the powder morphology, thus allowing significantly lower processing temperatures. The use of the method is limited due to the insufficient data on reactions taking place in solution. A lot of research has been done in understanding the synthesis pathway and processing in order to obtain monodispersed ceramic powders.

In the case of single oxide ceramics produced by the alkoxide–based sol–gel route, several parameters have to be selected: the precursors, the molar ratio of hydrolysis, and the presence of catalyst.
In the case of multicomponent oxides ceramics the different reactivities of the precursors need also to be considered.

The first aim of the present work is to find the correlations between the transition metal, hydrolysis conditions of the heterometallic acetate-alkoxide-based sol and the homogeneity and the morphology of $PbZrO_3$ and $PbTiO_3$ powders

Metals with a low electronegativity have a large positive charge resulting in a high sensitivity towards nucleophilic attack and therefore in a high reactivity towards water. The electronegativity of transition metals (TM) is much lower than that of silicon, which explains the large reactivity of the TM alkoxides towards hydrolysis. Among the TM of interest for us, Zr has an electronegativity of 1.29, which is lower than 1.32 of Ti (Livage *et al.*, 1988, Livage *et al.*, 1998), leading to a higher reactivity of the former towards water (Livage *et al.*, 1988).

The electronegative alkoxo groups (-OR) make the metal atom highly prone to the nucleophilic attack of the water molecule.

By carefully controlling the R_w, which is defined as the number of moles of H_2O per moles of $M(OR)_n$, (where M = metal atom, OR = alkoxide group and R an alkyl or aryl group, n = oxidation state of the M) the condensation of the hydrolysed species can be controlled. Livage (Livage *et al.*, 1988) reported that when $R_w<1$, the condensation is mainly governed by alcolation and alcoxolation reactions. Under such conditions, gelation or precipitation cannot occur as long as the hydrolysis remains controlled with no local excess of water.

In this hydrolysis range polynuclear oxo-alkoxide complexes are prepared. $Ti_{12}O_{16}(OPr^i)_{16}$ was synthesised by hydrolysis of $Ti(OPr^i)_4$ with 1 equiv of water in i-PrOH solution at 100°C for 3 days (Day *et al.*, 1993). $Zr_{13}O_8(OCH_3)_{36}$ was synthesized by mixing dilute methanol solution of NaOH and the alkoxide of zirconium (Morosin, 1977). Bimetallic oligomeric structures are also possible: $Ba_4Ti_{13}O_{18}(OCH_2CH_2OCH_3)_{24}$ was synthesised by hydrolysis of barium titanium methoxyethoxide (Campion *et al.*, 1991).

For $1<R_w<n$, condensation can occur via oxolation and alcoxolation. However, at a high degree of hydrolysis, oxolation becomes highly competitive, since the -OR groups become more and more positive. Finally for $R_w>n$, it is highly probable that olation instead of oxolation is the predominant pathway for condensation. In this domain, cross-linked polymers, particulate gels and precipitates are obtained.

TiO_2 powders composed of gel fragments with a poorly crystallized anatase structure are obtained from the ethoxide-based sol aged at a low relative humidity and nonagglomerated powders with a rutile structure when the sol is exposed to a high relative humidity (Slunecko *et al.*, 1998).
The condensation pathway has also a great impact on the morphology of the final product. Henry (Henry 1998) found that corner-sharing between polyhedra seems to be the prerequisite for building a rather open network, whereas edge- or face sharing favour the formation of dense, non-porous solids. Oxolation and not olation should be the main pathway to obtain a microporous phase.

The catalysts are also used to control the hydrolysis and condensation reactions. This can be done with an acid, such as HCl or HNO_3, or a base, such as NH_3 or NaOH. Figure 1.3-1 presents a typical example of a partially hydrolyzed titanium oxo polymer and the charges distribution along it is presented in Table 1.3-1. The partial charge (refer to Appendix) of the –OR group increases in the sequence D>A>C>B while the partial charge of titanium becomes more positive: B>A~C>D.

Under acidic conditions, the more negative is the charge on the –OR groups, the easier the protonation. Therefore, acid-catalysed condensation is directed preferentially towards the ends of the chain rather than

the middle of the chains, resulting in more extended, less branched polymers.

Under alkaline conditions the higher the partial charge of the metal, the higher reactivity towards nucleophilic attack. Therefore base catalysed condensation (as well as hydrolysis) is directed towards the centre rather than the end of the chains leading to more compact, highly branched species.

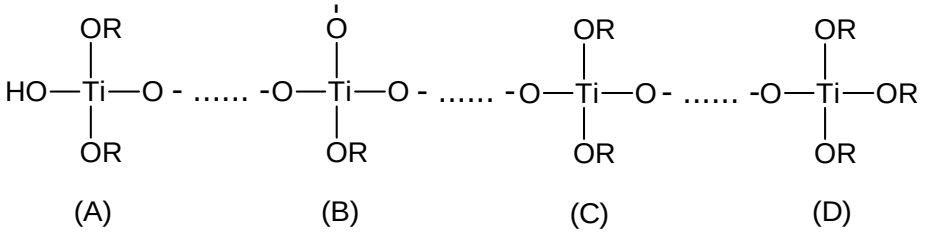

Figure 1.3-1. A typical partially hydrolysed polymer.

Table 1.3-1. Charge distribution in a titanium oxo polymer (from Livage *et al.*, 1988).

Site	δ(OR)	δ(Ti)
A	-0.01	+0.70
B	+0.22	+0.76
C	+0.04	+0.71
D	-0.08	+0.68

The second aim is the obtain knowledge about the structural evolution from the sol to the amorphous and crystalline $PbZrO_3$ and $La_2Zr_2O_7$ powders prepared by acetate-alkoxide and nitrate-alkoxide based sol-gel route.

There are only a few studies dedicated to the local environment of metal atoms in the early stage of the synthesis of $Pb(Zr,Ti)O_3$ powders and thin films and no studies on $La_2Zr_2O_7$ powders. However, structural changes are expected to take place in the transition from the liquid phase to the crystalline material.

In the case of alkoxide-based sol-gel synthesis of $La_2Zr_2O_7$ the role of nitrates has not been studied yet; therefore this topic has been also addressed in the thesis.

The pioneering work in investigation of lanthanum nitrate was performed in the period 1956-1960 by Wendlandt *et al.* (Wendlandt *et al.*, 1956; Stewart *et al.*, 1959). The only available datum of the lanthanum nitrate dissolution in 2-methoxyethanol is the salt solubility: 78g in 100g solution (Stewart *et al.*, 1959). Guha *et al.* (Guha *et al.*, 2003) studied the association state of the electrolytes in solution by conductometry and FTIR spectroscopy. They found that the nitrates, such as $NaNO_3$ and NH_4NO_3, remain strongly associated in 2-methoxyethanol forming contact ion pairs.

There are only a few studies of the oxidation/decomposition of the mixtures of nitrates and organic compounds: nitrate-citrate (Baythoun *et al.*, 1982; Schafer *et al.*, 1997) and nitrate-EDTA (ethylene-diaminetetraacetic acid) complexes (Wang *et al.*, 1992; Wang *et al.*, 1994). In both cases, upon heating the nitrate ions act as oxidizing agents for the organic groups of the precursors and enable their removal. Wang *et al.* (Wang *et al.*, 1992) found, for the case of $Pb(Zr_{0.52}Ti_{0.48})O_3$ powder synthesized from the nitrate-EDTA complex, that the crystallization of the perovskite phase is achieved at temperatures as low as 250 ^oC, because of the nitrate ions, which accelerate the precursor decomposition. Another advantage of the oxidation/decomposition in the system nitrates-organic compounds is that the fast reaction between reactants is accompanied by the evolution of gases. As a consequence, porous and friable powders can be produced by this synthesis route; these powders can then be sintered to highly dense ceramics.

3 Materials and Methods

3.1 Synthesis of $PbZrO_3$ and $PbTiO_3$ powders

3.1.1 Reagents

The reagents employed in the synthesis of $PbZrO_3$ (PZ) and $PbTiO_3$ (PT) powders were lead acetate hydrate $Pb(OCOCH_3)_2 \cdot 3H_2O$, zirconium (IV) n-butoxide n-butanol complex, $Zr[O(CH_2)_3CH_3]_4 \cdot CH_3(CH_2)_3OH$, Alfa Aesar, titanium (IV) n-butoxide, $Ti[O(CH_2)_3CH_3]_4$, Alfa Aesar, and 1-butanol anhydrous $CH_3(CH_2)_3OH$, Aldrich, as the solvent. Deionised water and ammonia solution 25%, GR, Merck were used for hydrolysis.

Lead acetate was dehydrated in vacuum at 70 ^oC for 16 h and at normal pressure at 140 ^oC for 10 h. The metal content of the reagents was determined gravimetrically.

3.1.2 Powder synthesis

The flow chart of the synthesis of PZ and PT powders is shown schematically in Figure 3.1-1.

Table 3.1-1 includes a list of the reagents, sol concentrations, hydrolysis conditions (R_w = moles of water/ moles of metal alkoxide) and the acronyms of the obtained precursor powders. The notation of the samples, used in this work, are composed of a core name, which represents the synthesised material and can be either PZ or PT. Additional letters or numbers may be added and their meaning are explained through the text. Ex.: PZ2 = core name (PZ) + additional (2).

3.1.3 Synthesis of the sol

All syntheses were performed in dry nitrogen atmosphere due to the extreme sensitivity of transition metal alkoxides towards water. The process involved dissolution of 10 millimoles of lead acetate in 10 millimoles of zirconium butoxide and 90 ml n-butanol (in the case of PZ) or 10 millimoles of titanium butoxide and 90 ml n-butanol (in the case of PT) at ~70 ^oC. The solutions were refluxed for 1h under constant stirring at 117^oC and distilled, to remove the volatile by-products. The sol concentration was 0.2 M for the majority of the syntheses. The hydrolysis products, which were used for Photon Correlation Spectroscopy (PCS) analysis, were prepared from the sols with 0.02 M concentration. The concentration of PZ sol, used in Extended X-ray Absorption Fine Structure Spectroscopy (EXAFS) analysis, was 0.5 M.

3.1.4 Hydrolysis of the sol

The PZ and PT sols were cooled to 0 ^oC and hydrolyzed in neutral and alkaline medium with different amounts of water/n-butanol. The sols were hydrolysed with R_w = 2, 5 and 15, where R_w is defined as moles of water/ moles of metal alkoxide. In the case of R_w = 2 and 5, the mixture water /n-butanol was 1:25 in volume and for R_w = 15 the mixture water/n-butanol was 1:7.5 in volume. In all cases, the pH at hydrolysis was around 6.

The hydrolysis in alkaline medium was performed using ammonia solution with the molar ratio $Pb:H_2O:NH_3$=1:15:5. The pH upon hydrolysis was about 11 for the sols with a 0.2 M concentration and about 9 for the sols with a 0.02 M concentration.

3.1.5 Drying and heating

The hydrolysed products, obtained from the sols with concentrations of 0.2 M and 0.02 M, were dried at 150 ^{o}C for 12 h and 90 ^{o}C for 48 h, respectively. The precursor powders were crushed in an agate mortar with pestle and heated to different temperatures between 400 ^{o}C and 700 ^{o}C for 1 h, using a heating rate of 10 ^{o}C / min in air.

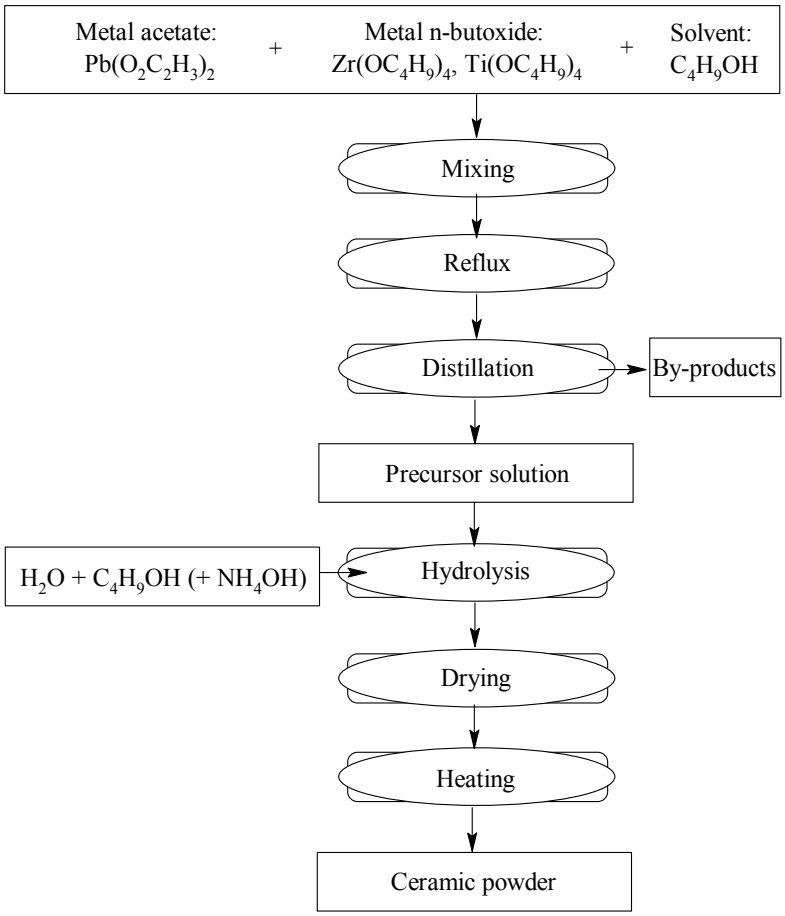

Figure 3.1-1. Flow chart of the synthesis of a ceramic powder

Table 3.1-1. List of the reagents, sol concentrations, hydrolysis conditions, and the acronyms of the obtained precursor powders.

	Chemicals (millimoles)			Concentration (M)	Hydrolysis condition - R_w		Precursor powder denotation
	$Pb(OAc)_2$	$Zr(nOBu)_4$	$Ti(nOBu)_4$		Neutral medium	Alkaline medium	
PZ	10	10	-	0.2	2	-	PZ2
	10	10	-	0.2	5	-	PZ5
	10	10	-	0.2	15	-	PZ15
	10	10	-	0.2	-	15	11PZ15
	10	10	-	0.02	-	15	PZ_d10
PT	10	-	10	0.2	2	-	PT2
	10	-	10	0.2	5	-	PT5
	10	-	10	0.2	15	-	PT15
	10	-	10	0.2	-	15	11PT15
	10	-	10	0.02	-	15	PT_d10

3.2 $La_2Zr_2O_7$ – synthesis of the powder and sintering

3.2.1 Reagents

The chemicals used for the synthesis of $La_2Zr_2O_7$ were lanthanum (III)-nitrate hydrate 99.9% $La(NO_3)_3 \cdot x H_2O$, Aldrich, zirconium (IV) n-butoxide n-butanol complex, $Zr[O(CH_2)_3CH_3]_4 \cdot CH_3(CH_2)_3OH$, Alfa Aesar, 2-methoxyethanol, ACS 99.3+%, $CH_3O(CH_2)_2OH$, Aldrich. The lanthanum content in $La(NO_3)_3 \cdot xH_2O$ was determined by inductive coupled plasma – atomic emission spectrometry (ICP-AES). The number of moles of water in $La(NO_3)_3 \cdot xH_2O$ was calculated as x=5.56.

3.2.2 Synthesis of the sol

9.0 millimoles of $La(NO_3)_3 \cdot 5.56\ H_2O$ were dissolved in 70 ml of $CH_3OC_2H_4OH$ and heated to the boiling point of $CH_3OC_2H_4OH$ at 124 ^oC. 30 ml were distilled off with the azeotrope mixture H_2O – $CH_3OC_2H_4OH$ (molar fraction H_2O: $CH_3OC_2H_4OH$ = 0.959 : 0.041 and distillation point 99.9^oC) (Gmehling *et al.*, 2008).

The dehydrated $La(NO_3)_3$ solution was then mixed with 9.0 millimoles of $Zr(OC_4H_9)_4$ in $CH_3OC_2H_4OH$ and refluxed for 3 h. The sol concentration was 0.1 M. For the EXAFS and thermal gravimetry and differential thermal analysis (TG/DTA), the sols with 1M concentration were used.

3.2.3 Drying and heating

The sol (0.1 M) was dried by heating at 150 ^oC for 12 h, the obtained powder was crushed in an agate mortar and heat treated at 700 ^oC, 800 ^oC, 900 ^oC and 1000 ^oC for 1 h and at 1100 ^oC for 6 h.

3.2.4 Milling, pressing and sintering

The powder, heated at 900 ^oC, was milled in acetone for 30 min in a zirconia ball mill (YSZ, Tosoh, ball diameter =10 mm). The powder was uniaxially pressed into pellets (Φ = 6mm) at 100 MPa and subsequently by cold isostatic pressing (CIP) at 500 MPa, and sintered at 1400 ^oC for 2 h in air.

3.3 Characterization methods

3.3.1 Nuclear Magnetic Resonance (NMR)

The quantitative analysis of the amounts of butyl acetate in the distillates was performed by ^1H nuclear magnetic resonance (NMR). The spectra were recorded using Varian EM 360L spectrometer at 60 MHz and 1,1-diphenylethylene as an internal standard.

3.3.2 Extended X-ray Absorption Fine Structure Spectroscopy (EXAFS)

Pb L_3-edge and some of the Zr K-edge spectra were measured at ROEMO II (X1) station in HASYLAB at DESY (Hamburg, Germany) while La L_3 – edge and some of the Zr K-edge were measured at XAFS (BL 11.1) beamline ELETTRA (Trieste Italy). All spectra were recorded in a standard transmission mode at room temperature. The intensity of the incident and transmitted monochromatic x-ray beam were measured by three consecutive ionization chambers. Gasses and their pressure used to fill the ionization cells are given in Table 3.3-1.

The Doris ring operates at 4.44GeV and a current of about 130 mA. A Si(311) double-crystal

monochromator was used with 2 eV resolution at 18 keV. Harmonics were effectively eliminated by detuning the monochromator crystal using a stabilization feedback control.

The ELETTRA storage ring operated in multibunch mode at electron energy of 2.4 GeV and a current of about 140 mA. A Si(111) double crystal monochromator was used with 1.5 eV resolution at the Zr K-edge (17998 eV) and 0.8 eV resolution at the La L_3-edge (5483 eV). The beam size was 1.7 mm x 6 mm.

Table 3.3-1. Content of the ionization cells (gasses and their pressure) at the appropriate EXAFS edge and storage ring.

Storage ring	EXAFS edge	Gas	Gas pressure in the ionization cells (mbar)		
			First	Second	Third
Doris	Pb-L_3	Ar	400	-	-
		Kr	-	1000	1000
	Zr-K	Ar	1000	-	-
		Kr	-	1000	1000
	La-L_3	He	1800	900	860
		N_2	200	1100	1000
Elettra		Ar	-	-	140
	Zr-K	N_2	1700	-	1600
		Ar	300	2000	-
		Kr	-	-	400

The powder samples were prepared in the form of homogeneous pellets, by mixing the powder sample with boron nitride powder (BN), 99.5 %, Alfa Aesar, to obtain self-supported pellets. 40 mg / cm^2 of sample and 100 mg / cm^2 BN were used for Zr K-edge and Pb-L_3 edge and 5 mg / cm^2 of sample and 30 mg / cm^2 BN for La L_3 edge. Liquid samples were prepared in inert atmosphere and sealed in thin vacuum-tight plastic bags to prevent hydrolysis in air. In all cases the samples with optimum absorption thickness of about 2 above the investigated absorption edge were prepared and inserted in the monochromatic beam between the first and the second ionization cells.

The absorption spectra were measured within the interval [-250 eV … 1000 eV] relative to the respective Zr K-edge or Pb L_3-edge. In the x-ray absorption near edge spectroscopy (XANES) region equidistant energy steps of 0.5 eV were used, while for the EXAFS region equidistant energy steps of 2 eV were adopted with the integration time of 2 s / step.

For La L_3-edge EXAFS scans a shorter interval was chosen [-250 eV … 450 eV] because of the subsequent L_2 edge (5891 eV). In the XANES region equidistant energy steps of 0.3 eV were used, while for the EXAFS region equidistant energy steps of 2 eV were adopted with the integration time of 2 s / step. With several consecutive runs of each spectrum the signal-to-noise ratio was improved.

Exact energy calibration was established with simultaneous absorption measurements on a 10 micron thick Zr or Pb metal foil or 5 micron thick Ti metal foil placed between the second and the third ionization chamber in all experiments. Absolute energy reproducibility of the measured spectra was ±0.1 eV.
The quantitative analysis of EXAFS spectra was performed with the IFEFFIT program packages (Ravel *et.al* 2005). Structural parameters were quantitatively resolved by comparing the measured signals with model signals, constructed ab initio with the FEFF6 program code (Rehr *et al.*, 1992) from the set of scattering paths of the photoelectron in a tentative spatial distribution of neighbour atoms. In the process, the atomic species of a neighbour was recognized by its specific scattering factor and phase shift.

Absorption spectra of La L_3 edge exhibit particularly strong effects of multielectron photoexcitations. In the region 100-180 eV above the edge, features due to coexcitation of $2p_{3/2}$ and 4d electrons interfere with the structural signal and reduce the resolving power of EXAFS analysis significantly. So, prior to analysis, the approximate atomic absorption obtained from the reference sample was subtracted from the normalized experimental spectra (Kodre *et al.*, 1994).

The least-square determination of structure parameters was performed in k-range = 4-12 $Å^{-1}$ for Zr K-edge, 4.3-13 $Å^{-1}$ for Pb L_3-edge and 2.5 – 9.9 for La L_3-edge. The amplitude reduction factor (S_o^2) was fixed to 0.9 for all analysed edges. The least-square fits of the spectra of PZ dried samples were performed at both edges simultaneously, so that the parameters of the path linking Pb and Zr atoms could be restrained to the same values in both spectra. The coordination numbers and corresponding Debye-Waller factors were strongly correlated. To avoid large error brackets arising in the correlation the Debye-Waller factors were kept fixed at a common average value.

3.3.3 Photon Correlation Spectroscopy (PCS)

The particle size distribution of the hydrolysis products and the zeta potential were determined using photon correlation spectroscopy (PCS, Zeta Pals Brookhaven Instrument Corporation).

3.3.4 Sedimentation curve

The sedimentation curves were recorded using Dispersion Analyser (LUMiSizer® of L.U.M. GmbH) by placing the hydrolysis product in a 2.2 mm cell and spun under 1000 rpm for 40 min.

3.3.5 Infrared Spectrometry (IR)

The IR spectra were recorded by a Perkin-Elmer FT-IR 1720X spectrometer in a transmission mode. All spectra were collected between 4000 - 400 cm^{-1} at 4 cm^{-1} resolution. Data collection and processing were performed with Spectrum v2.00, Version 2.00 (1998), Perkin-Elmer Ltd.1998. The solid samples were prepared in the form of pellets by mixing the sample with KBr, 99+ %, FT-IR grade, Sigma-Aldrich. The liquid samples were recorded by spreading a liquid drop on a KBr window.

3.3.6 Thermal Analysis (TG/DTA/EGA)

The thermal behaviour of the dried powders was investigated from room temperature to 640 ^{o}C using thermogravimetric analysis (TG) and differential thermal analysis (DTA) (Netzsch STA 409) coupled with a mass spectrometer (Thermostar GSD 300 T Balzers) for the evolved-gas analysis (EGA). The experiments were conducted in flowing air, using Pt crucibles, with a heating rate of 10 ^{o}C / min.

3.3.7 X-ray Diffraction (XRD)

The phase composition of the powders heated at different temperatures was investigated by X-ray diffraction (Bruker AXS D4 Endeavor diffractometer) using CuK_{α} radiation. The crystallite size of the samples was determined by X-ray line broadening analysis using the Voigt function (Langford, 1992). The profile refinements were analyzed using Peakoc software (Masson, 2000) and the instrumental line profile was evaluated using the standard reference material LaB_6 (NIST, SRM 660). In order to calculate the crystallite size, the approximation of spherical crystallites was used (Langford, 1992).

3.3.8 Scanning Electron Microscopy (SEM)

The morphology of the powders was analysed using scanning electron microscopes: a SEM JEOL JSM 5800 and a Zeiss SUPRA 35VP. The operating parameters of the microscopes are collected in Table 3.3-2

The powder samples were prepared as follow:

1. For investigation at lower magnifications (SEM JEOL JSM 5800) - a substrate such as a carbon conductive tape was used to spread the particles on and canned air was used to remove any loose material from the top of the tape. The as prepared powders were gold coated.
2. For investigation at higher magnifications (FESEM Zeiss Supra 35VP) - the powders were dispersed in acetone under ultrasound, and a few drops were spread on a substrate such as mica, highly oriented pyrolytic graphite or copper grid 200 Mesh.

Table 3.3-2. Summary of the working parameters for the powder morphology investigations.

	ACC (kV)	Aperture (μm)	WD (mm)	Magnification
JOEL JSM 5800	20	20	10	1 kx - 2.5 kx
FESEM Zeiss Supra 35VP	5	20	5	5 kx – 150 kx

ACC – accelerating voltage, WD – working distance

3.3.9 Specific Surface Area – BET

The specific surface area (SSA) of the powders was measured by Brunauer Emmett Teller (BET) method (Micrometrics Gemini). The particle size (d_{BET}), for selected samples, was calculated according to Eq. 3.3-1

$$d_{BET} = 6 / SSA \cdot D_x \qquad \text{Eq. 3.3-1}$$

where: SSA – specific surface area and D_x – theoretical density

For the precursor powders D_x was estimated as the tap density of 3 g / cm^3, while for the crystalline powders, the theoretical density was used: $D_{x\,(PZ)}$ = 8.055 g / cm^3 (JCPDS 87-0570), $D_{x\,(PT)}$ = 7.954 g / cm^3 (JCPDS 78-0298), $D_{x\,(LZ)}$ = 6.05 g / cm^3 (JCPDS 73-0444).

3.3.10 Particle size measurements

The median particle size (D_{50}) and particle size distribution were determined by laser granulometry (Cilas Alcatel) in isopropanol. The polydispersity index (P.I.) was calculated according to the Eq. 3.3-2 (He *et al.,* 2006; Landillon *et al.,* 2008).

$$\text{P.I.} = (D_{90}\text{-}D_{10}) / D_{50} \qquad \text{Eq. 3.3-2}$$

3.3.11 Density

The bulk density of the ceramic samples was determined geometrically and for selected samples by hexane pycnometry.

3.3.12 Sintering curves

A heating-stage microscope (Leitz Wetzlar), with a heating rate of 10 ^{o}C / min., was used to record the dimensions of the pellet, pressed with 100 MPa, upon heating to 1400 ^{o}C. From these data and the green density, the density of the pellet sintered at a selected temperature, was calculated according to the Eq. 3.3-3 (Kolar, 1993).

$$\frac{L_o - L}{L_o} = \left[1.00 - \left(\frac{\rho_{green}}{\rho} \right)^{1/3} \right] \cdot 100\% \qquad \text{Eq. 3.3-3}$$

Where L_o – the initial dimension of the pellet, L – the final dimension of the pellet, ρ_{green} – green density of the pellet and ρ – density of the sintered pellet.

4 Results and Discussions

4.1 $PbZrO_3$

This chapter describes the synthesis and characterization of the sol, the dried precursor powder and $PbZrO_3$ (PZ) powder. The sol (0.2 M) was prepared from lead acetate and zirconium n-butoxide in butanol, refluxed and distilled to remove the by products. The sol was then hydrolysed with different R_w in neutral and in alkaline medium.

At hydrolysis with $R_w = 2$ a translucent stiff gel developed slowly (~5min). In the case of $R_w = 5$ and 15 the hydrolysis proceeded slowly resulting in a semi-solid gel. In alkaline medium and at $R_w = 15$ a white suspension formed and slowly deposited a sediment in the case of 0.2 M sol, while for the 0.02 M sol, a semi-solid gel was observed. The hydrolysis products were dried at 150 ^oC and then heated at 500 ^oC / 1h and 700 ^oC / 1h.

We used EXAFS for studying the local environment of metallic species of PZ precursor sol, PZ dried powders prepared with different hydrolysis conditions and PZ heated powder at 400 ^oC in order to follow the evolution of the local environment of the metallic atoms along the synthesis path.

Using a partial charge model we calculated the stability of species at hydrolysis and condensation. The agglomeration state of the particles of the hydrolysed sol was investigated. The impact of the hydrolysis conditions on the decomposition pathway, the homogeneity and the morphology of the powders was assessed.

4.1.1 Synthesis of the sol

The sol was prepared from lead acetate and zirconium n-butoxide in butanol. Lead acetate does not dissolve in n-butanol but a clear sol is obtained by the reactive dissolution of lead acetate in zirconium butoxide in butanol with the elimination of butyl-acetate (Eq. 4.1-1) (Chandler *et al.*, 1993) and/or as an addition reaction (Eq. 4.1-2) (Kosec *et al.*, 1995; Malic *et al.*, 1997). The reactions are written for one acetate group and one alkoxide group.

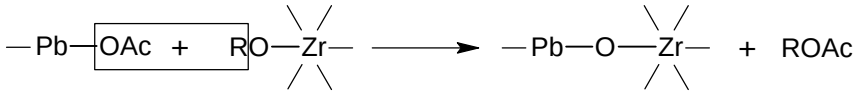

Eq. 4.1-1

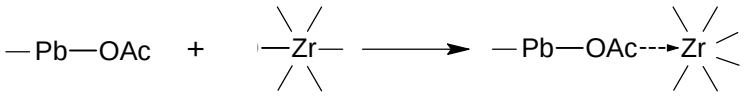

Eq. 4.1-2

where Ac=$OCCH_3$ and R=C_4H_9 in the present work.

Butyl-acetate forms an azeotrope mixture with n-butanol with the molar ratio 0.23: 0.77 and b.p. = 116.8^oC (Gmehling *et al.*, 2008). The amount of acetates removed by distillation as butyl-acetate was determined by NMR analysis. From initial 20 millimoles acetate about 25 % is removed, while the rest of 75 % remains in the sol, confirming that both reactions occurred.

4.1.2 Structural evolution from the sol to the $PbZrO_3$ precursor powders

Figure 4.1-1 presents Pb-L_3 edge EXAFS spectra of the sol (PZ_L), the dried powders prepared at different hydrolysis conditions (PZ2_D, PZ5_D, PZ15_D, 11PZ_D) and the powder 11PZ heated at 400 ^oC / 1h (11PZ_H). Fourier transforms of the spectra exhibit two prominent peaks, the fingerprints of the photoelectron backscattering on the nearest neighbours around Pb atom. Qualitative comparison indicates that the structure of the immediate neighbours at about 2 Å is retained, while significant changes are

observed in the second coordination shell at about 3.5 Å. The intensity of the second peak in the spectrum of PZ-L sample is reduced to about half the value in the spectra of the dried samples.

The local environment of Pb atoms can be reliably deduced in the quantitative EXAFS analysis, performed in the k interval from 4.3 Å to 13 Å. The complete list of the best fit structural parameters is given in Table 4.1-1. The Pb atom is coordinated to two O atoms: one at 2.22 Å, and one at 2.37 Å in all samples. In the second coordination shell, we found two Zr atoms at nonequal distances in PZ-L: one at 3.45 Å and one at 3.58 Å. In the spectra of PZ-D powders only one Zr neighbour is present, located at the distance of 3.58 Å. After heating at 400°C (11PZ-H sample) the Pb-O-Zr correlation is lost: there are no Zr neighbour atoms in the second coordination sphere of Pb.

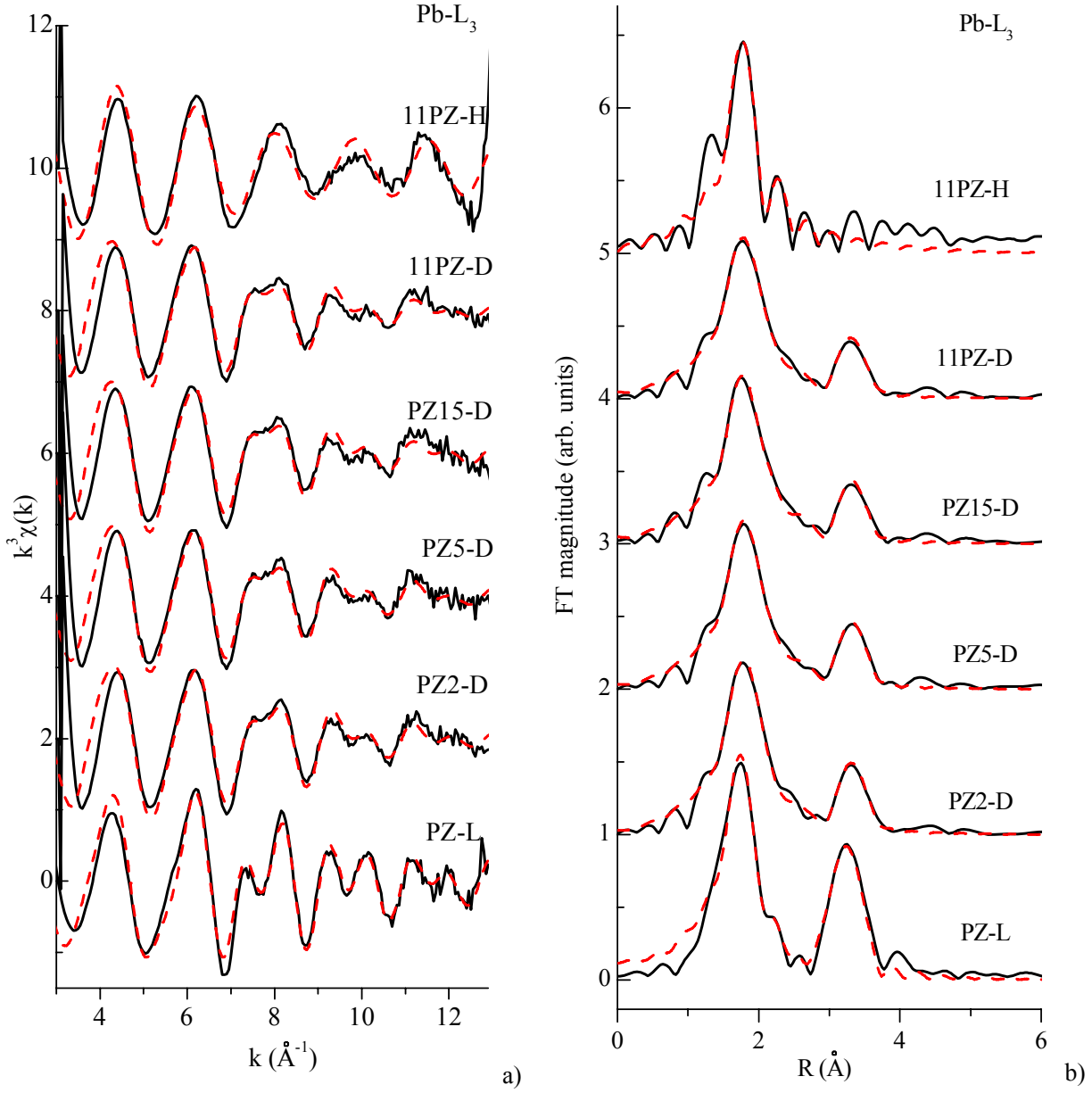

Figure 4.1-1. k^3 weighted Pb-L_3 data (a) and their k^3 weighted Fourier transforms (b) of PZ sol (PZ_L), PZ dried powders prepared at different hydrolysis conditions (PZ2_D, PZ5_D, PZ15_D, 11PZ_D) and 11PZ powder heated at 400 °C / 1h (11PZ_H). Solid line – experiment, dashed line – – – EXAFS model.

Table 4.1-1. Parameters of the nearest coordination shells around Pb atoms in PZ samples. Type of the neighbour atom, average number N, distance R and Debye Waller factor σ^2 are listed. Uncertainty of the last digit is given in parenthesis. For parameters that are kept fixed in the fit, the error brackets are omitted. The quality of the fit is indicated by R-factor (Ravel *et al.*, 2005).

Sample	Scattering atom	N	R(Å)	σ^2	R-factor
PZ_L	O	1.4(1)	2.21(1)		
	O	0.7(1)	2.37(2)	0.006	
	Zr	0.6(1)	3.45(2)		0.015
	Zr	1.2(1)	3.58(1)	0.006	
PZ2-D	O	1.0(1)	2.20(2)		
	O	0.8(1)	2.33(2)	0.005	0.005
	Zr	1.0(1)	3.58(2)	0.012	
PZ5-D	O	1.0(1)	2.21(1)		
	O	0.7(1)	2.35(2)	0.005	0.004
	Zr	1.0(1)	3.58(2)	0.012	
PZ15-D	O	1.0(1)	2.21(1)		
	O	0.8(1)	2.35(2)	0.005	0.005
	Zr	1.0(1)	3.59(2)	0.012	
11PZ-D	O	1.0(1)	2.21(2)		
	O	0.8(1)	2.34(3)	0.005	0.005
	Zr	1.0(2)	3.58(3)	0.014	
11PZ_H	O	1.2(1)	2.22(1)		
	O	0.6(2)	2.39(2)	0.004	0.032

Zr-K edge EXAFS spectra of all samples are presented in Figure 4.1-2. Fourier transforms of the EXAFS spectra of all samples exhibit two strong peaks. The quantitative EXAFS analysis is performed in the k interval from 4 to 12 $Å^{-1}$. The best fit parameters of the nearest coordination shells around Zr atoms are collected in Table 4.1-2. The analysis reveals that the first peak in all spectra is composed of O atoms distributed between 2.10 Å and 2.25 Å. At larger distances C, Zr and Pb neighbours are identified in all cases except for the11PZ-H sample, where Pb is not present. The Zr environment in the PZ_L is populated by about eight O, one C, six Zr and two Pb atoms. In the spectra of the dried powders the number of O neighbours is diminished as compared to the sol from about eight to about seven, number of Zr neighbours is diminished from six to five and number of lead neighbours from two to one. After heating at 400^{o}C/1h the structure of Zr local neighbourhood is mainly retained in the 11PZ-H sample with only one exception: there are no Pb neighbours, in agreement with Pb L_3 edge EXAFS results.

In the synthesis of PZ sol, lead acetate and zirconium butoxide come in contact through the mediation of the solvent, n-butanol. Pb-Zr correlations which we found in PZ_L (Table 4.1-1, Table 4.1-2) are explained through the reactions between lead acetate and zirconium n-butoxide (Eq. 4.1-1, Eq. 4.1-2).

Peter *et. al.* (Peter *et al.*, 1994) investigated zirconium n-butoxide diluted in the parent alcohol. Their analysis revealed that zirconium n-butoxide adopted a dimer configuration, where Zr is six-fold coordinated. During thermolysis (Turova *et al.*, 2002) alkoxides are known to react into oxoalkoxides by the ether elimination (Eq. 4.1-3). The reaction is written for one alkoxide group only.

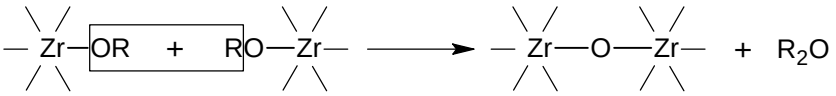

Eq. 4.1-3

where R=C_4H_9 in the present work.

Zr polynuclear oxo-alkoxide complexes have been proposed to form during reflux and distillation of the PZT precursor, containing lead acetate, Zr and Ti alkoxide (Malic *et al.*, 2006) and also other compounds such as $Zr_{13}O_8(OCH_3)_{36}$ (Morosin, 1977). There is evidence that other metal alkoxides such as Ti, Nb and Ce alkoxides can form polynuclear oxo-alkoxide complexes (Sirio *et al.*, 1997; Turova *et al.*, 2002). The ether to form in our case is butyl-ether, boiling point (b.p.) = 142 ^{o}C, which forms an azeotrope mixture with n-butanol at the molar ratio 0.13: 0.87 and b.p. =117.4^{o}C, which is 0.3 ^{o}C lower than the b.p. of n-butanol. The azeotrope mixture can be removed by distillation.

EXAFS analysis of PZ-L revealed a high coordination number of Zr: about eight O atoms and a relatively large number of Zr-Zr correlations, about six (Table 4.1-2). We propose that oxoalkoxides, similar to those in the cited papers, are formed also in our case.

Figure 4.1-3 presents a sketch of oligomers that can form during the sol synthesis. The homogeneous distribution of Pb-O-Zr and Zr-O-Zr links is represented in the case A, while the case B represents a heterogeneous distribution of Pb-O-Zr and Zr-O-Zr links, with a preferential distribution of Zr-O-Zr links inside the oligomers and Pb-O-Zr links at the ends of the oligomers.

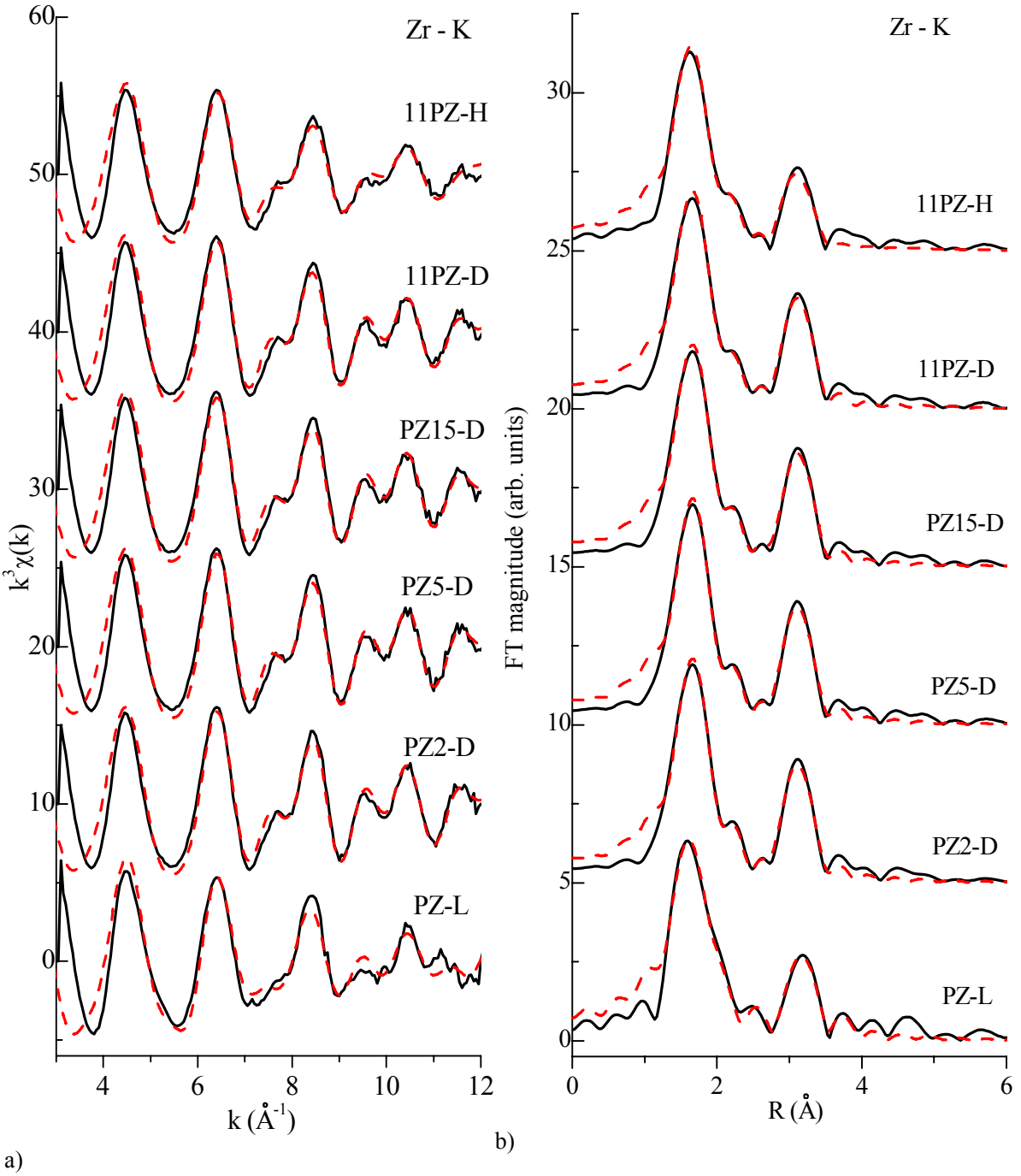

Figure 4.1-2. k^3 weighted Zr-K data (a) and their k^3 weighted Fourier transforms (b) of PZ-L sol, PZ-D dried powders prepared under different hydrolysis conditions and 11PZ-H powder heated at 400 °C / 1h. Solid line – experiment, dashed line - - - EXAFS model.

Table 4.1-2. Parameters of the nearest coordination shells around Zr atoms in PZ samples. Type of neighbour atom, average number N, distance R and Debye Waller factor σ^2 are listed. Uncertainty is given as the absolute value or, when in parenthesis, in units of the last digit. For parameters that are kept fixed in the fit, the error brackets are omitted. The quality of the fit is indicated by R-factor (Ravel *et al.*, 2005).

Sample	Scattering atom	N	R(Å)	σ^2	R-factor
PZ-L	O	4.3(5)	2.10(1)	0.003	0.014
	O	3.4(5)	2.25(1)		
	C	1.35±1.4	2.61(6)	0.007	
	Zr	6.4±1.1	3.49(1)	0.013	
	Pb –set	0.6(1)	3.45(2)	0.006	
	Pb –set	1.2(1)	3.58(1)		
PZ2-D	O	4.4(3)	2.12(1)	0.003	0.005
	O	2.5(2)	2.26(1)		
	C	1.4(8)	2.73(3)	0.008	
	Zr	4.9(3)	3.46(1)	0.009	
	Pb	1.0(1)	3.58(2)	0.012	
PZ5-D	O	4.3(3)	2.12(1)	0.003	0.004
	O	2.5(2)	2.25(1)		
	C	1.3(7)	2.73(3)	0.008	
	Zr	4.8(3)	3.45(1)	0.009	
	Pb	1.0(1)	3.58(2)	0.012	
PZ15-D	O	4.3(3)	2.11(1)	0.003	0.005
	O	2.7(2)	2.25(1)		
	C	1.3(8)	2.74(3)	0.008	
	Zr	4.6(3)	3.46(1)	0.009	
	Pb	0.9(1)	3.59(2)	0.012	
11PZ-D	O	4.3(3)	2.11(1)	0.003	0.005
	O	2.7(2)	2.25(3)		
	C	1.2(7)	2.73(4)	0.008	
	Zr	4.9(3)	3.46(1)	0.010	
	Pb	1.0(2)	3.58(3)	0.014	
11PZ-H	O	4.3(4)	2.11(1)	0.003	0.010
	O	2.5(4)	2.25(3)		
	C	1.0(9)	2.72(4)	0.007	
	Zr	4.9(8)	3.44(1)	0.013	

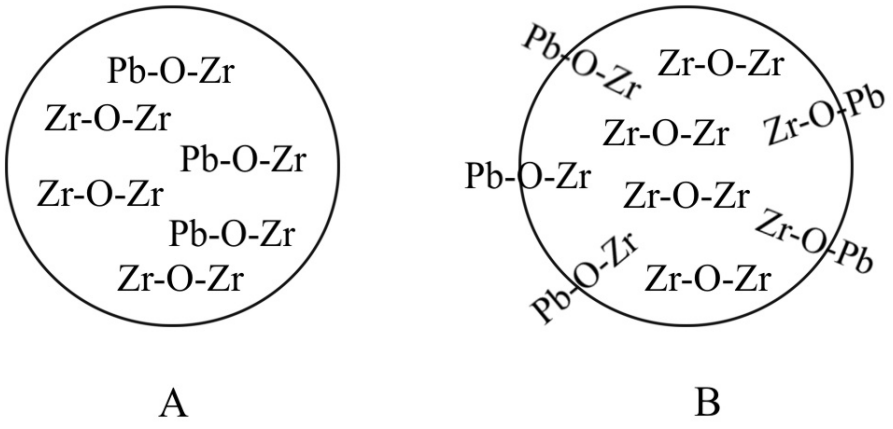

Figure 4.1-3. Sketch of possible distributions of the metal atoms during the sol synthesis. A) Homogenous distribution of the Pb-O-Zr and Zr-O-Zr links, B) Heterogeneous distribution of the Pb-O-Z and Zr-O-Zr links; Zr-O-Zr links inside the oligomer and Pb-O-Zr links at the ends of the oligomer. Note that only the M-O-M links are shown in the sketch.

The case A sustains a hypothesis that the Pb-O-Zr links are formed prior to the formation of Zr oxo-alkoxides, which will assure a uniform distribution of Pb atoms inside the oligomer, while the formation of the Zr oxo-alkoxides prior to the reaction between Pb and Zr species yielding Pb-O-Zr links would lead to the case B.

Since Pb is connected to two Zr atoms (Table 4.1-1) and Zr is connected to two Pb atoms (Table 4.1-2), and the stoichiometry Pb:Zr=1:1, we propose that the case A is the more probable.

The next step of the synthesis is hydrolysis, where alkoxide groups are partially exchanged with hydroxyl groups (Eq. 4.1-4). The resulting species are very reactive and immediately undergo a condensation reaction (Eq. 4.1-5) with the formation of M-O-M bridges (Brinker *et al.*, 1990). The reactions are written for Zr n-butoxide and for one alkoxide group only.

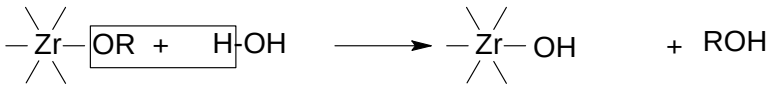

Eq. 4.1-4

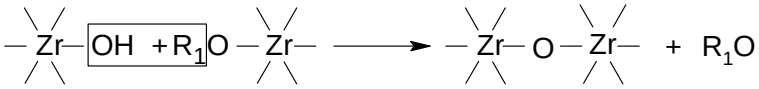

Eq. 4.1-5

where R=OC_4H_9; R_1= H, R.

The change of the Pb and Zr environment from the sol to the amorphous powder is summarized in Figure 4.1-4. In the sol, Pb established two links with Zr (Figure 4.1-4a) and Zr established two links with Pb (Figure 4.1-4b). The analysis of the dried powder reveals that only one Pb-O-Zr link persists (Table 4.1-1, Table 4.1-2), which means that the Pb atoms are still a component part of the oligomers similar to those in the case A (Figure 4.1-3). By heating the powder at 400°C, the Pb-O-Zr links are completely lost. The Zr coordination number decreases from eight to seven and Zr-O-Zr links diminish from six to five upon the transition from sol to the powder, but they remain almost stable upon heating at 400°C.

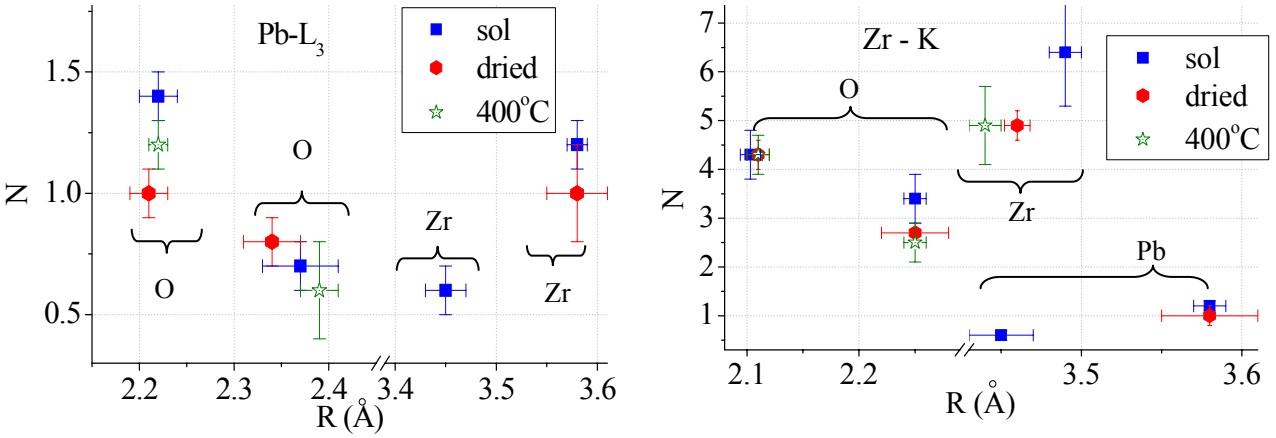

a) b)

Figure 4.1-4. Numbers of Pb and Zr neighbours (N) at the interatomic distance (R) obtained from the Pb-L_3 EXAFS results a) and the Zr-K EXAFS results b) in different stages of the evolution from the sol to the amorphous powder. Note the different y-scale in a) and b) graphs. The data correspond to the 11PZ15 samples (dried and 400 °C).

The Pb and Zr environment, in the dried powders, prepared under different hydrolysis conditions, is summarized in Figure 4.1-5. Under all hydrolysis conditions, only one Pb-O-Zr link is present in all PZ_D powders (Figure 4.1-5a) and the number of Zr-O-Zr is not changed (Figure 4.1-5b). There is no effect of R_w or pH on Pb and Zr environment observed within the EXAFS range.

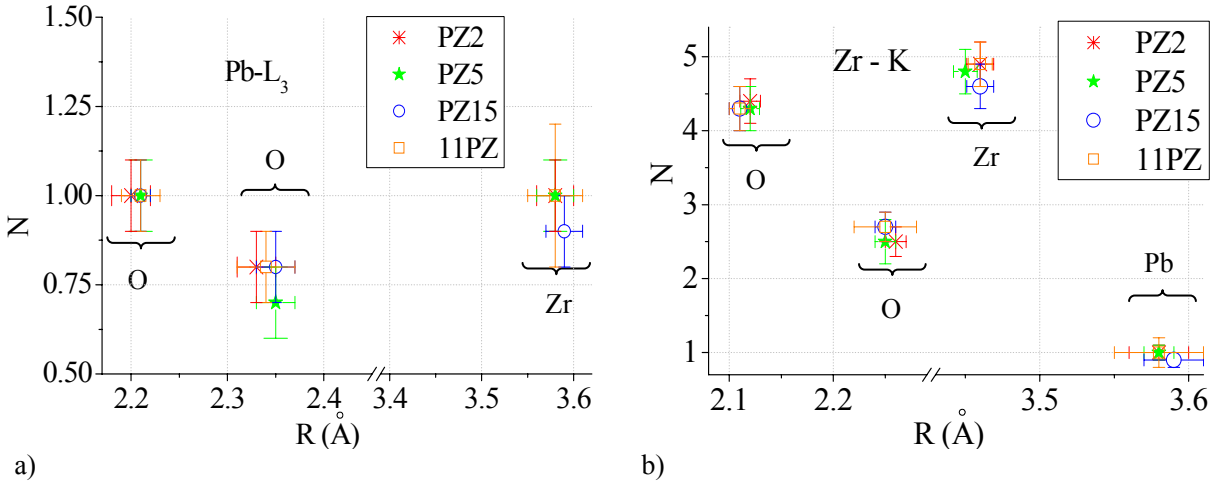

Figure 4.1-5. Numbers of Pb and Zr neighbours (N) at the interatomic distance (R) obtained from the Pb-L_3 EXAFS results a) and the Zr-K EXAFS results b) of powders prepared with different hydrolysis conditions. Note the different y-scale in a) and b) graphs.

4.1.3 Hydrolysis and condensation –stability of the species

By the reaction of zirconium n-butoxide with a water molecule, one butoxide group is replaced with a hydroxyl group (Eq. 4.1-6). The equation is based on the three step mechanism, proposed in the literature (Livage *et al.*, 1988).

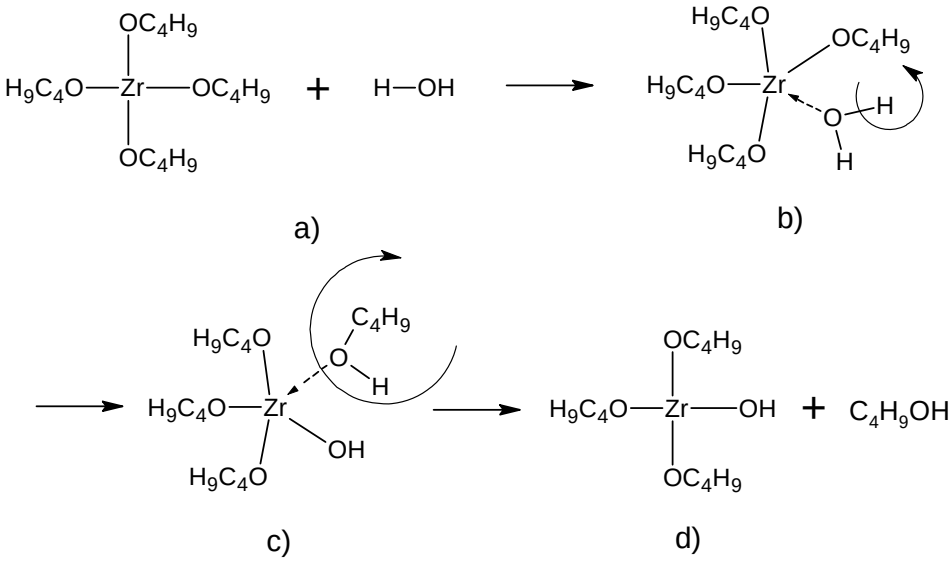

Eq. 4.1-6

By using the partial charge model we calculated the charges of constituent parts of intermediate and final products of hydrolysis (Eq. 8.1-2)

The electronegativities of the atoms used in the calculations are presented in Table 4.1-3 (Livage *et al.*, 1988). The partial charges of the constituent species during hydrolysis are presented in Table 4.1-4.

The species a)-d) (Table 4.1-4) include the hydrolysed product and the partial charges of the constituent parts during the three steps of the hydrolysis. The first step is a nucleophilic addition of the water molecule to the positively charged zirconium atom ($\delta = 0.6322$). At this step we can notice an increase in the partial charge of the metal from $\delta=0.6322$ to $\delta = 0.6392$ while the butoxide group becomes less negative, i.e. δ changes from $\delta = - 0.1580$ to $\delta = - 0.0846$. In the next step, due to the positive charge of the metal atom, the most probable leaving group is the group with a positive charge, which is C_4H_9OH with $\delta = 0.0053$. Since in the case d), the partial charge on the metal ($\delta=0.6393$) is higher then the initial partial charge ($\delta = 0.6322$), this results in an increase of the species' reactivity.

Depending on the hydrolysis degree, the hydrolysis product can be expressed by the formula $M(OR)_{4-x}(OH)_x$, where M = metal atom, OR = alkoxide group and $x \leq 4$.

For the case of x = 2, which in our experimental conditions is equivalent to $R_w = 2$, this theoretically corresponds to a 50 % exchange of (OR) groups with (OH) groups, while for x = 4, the exchange is 100 %. The products e) and f) (Table 4.1-4) present the zirconium species with 50 % and 100 % exchanged alkoxide groups and their corresponding partial charges. As hydrolysis advances, an increase in the partial charge of the metal is observed, $\delta = 0.6517$ for the product with a 50 % exchanged groups and even higher $\delta = 0.7798$ for the case where the (OR) groups were completely exchanged by (OH) groups. For the same product there is a decrease in the partial charge of the (OH) groups, but they still remain negatively charged.

Table 4.1-3. Electronegativities of selected atoms (Livage, 1998).

	Zr	O	C	H
Electronegativity	1.29	3.50	2.50	2.10

Table 4.1-4. Partial charges of constituent parts of zirconium n-butoxide during hydrolysis.

	Species	δ(M)	δ(O)	$\delta(OC_4H_9)$	$\delta(C_4H_9OH)$	δ(HOH)	δ(OH)
a)	$Zr(OC_4H_9)_4$	0.6322	-0.4847	-0.1580			
b)	$Zr(OC_4H_9)_4(HOH)$	0.6392	-0.4805	-0.0846		-0.3005	
c)	$Zr(OC_4H_9)_3(OH)(C_4H_9OH)$	0.6392	-0.4805	-0.0846	0.0053		-0.3905
d)	$Zr(OC_4H_9)_3(OH)$	0.6393	-0.4804	-0.0830			-0.3903
e)	$Zr(OC_4H_9)_2(OH)_2$	0.6517	-0.4729	0.04724			-0.3731
f)	$Zr(OH)_4$	0.7798	-0.3951				-0.1949

Once the hydrolysis starts, there is an increase in the partial charge of the metal atoms; therefore they become highly prone to the nucleophilic attack of the negatively charged hydroxyl group. Next, the reactive species undergo a condensation reaction (Eq. 4.1-7). The reaction is written for the specific case x = 1 i.e. $Zr(OC_4H_9)_3(OH)$. In the steps a) and b) the zirconium species are coming closer with the formation of an intermediate state where the coordination number of the zirconium increases by one.

The c) and d) products and the partial charges of their constituent parts involved during condensation are presented in Table 4.1-5. Similarly as in the case of hydrolysis, the C_4H_9OH has a positive partial charge and consequently the highest probability to be a leaving group. As the leaving group is an alcohol molecule, the condensation pathway is alcoxolation. The partial charge of the metal atom slightly increases from $\delta = 0.6392$ to $\delta = 0.6393$. The same calculation shows that the partial charge of the OH group slightly decreases from c) to d) but it still remains nucleophilic enough to initiate further condensation.

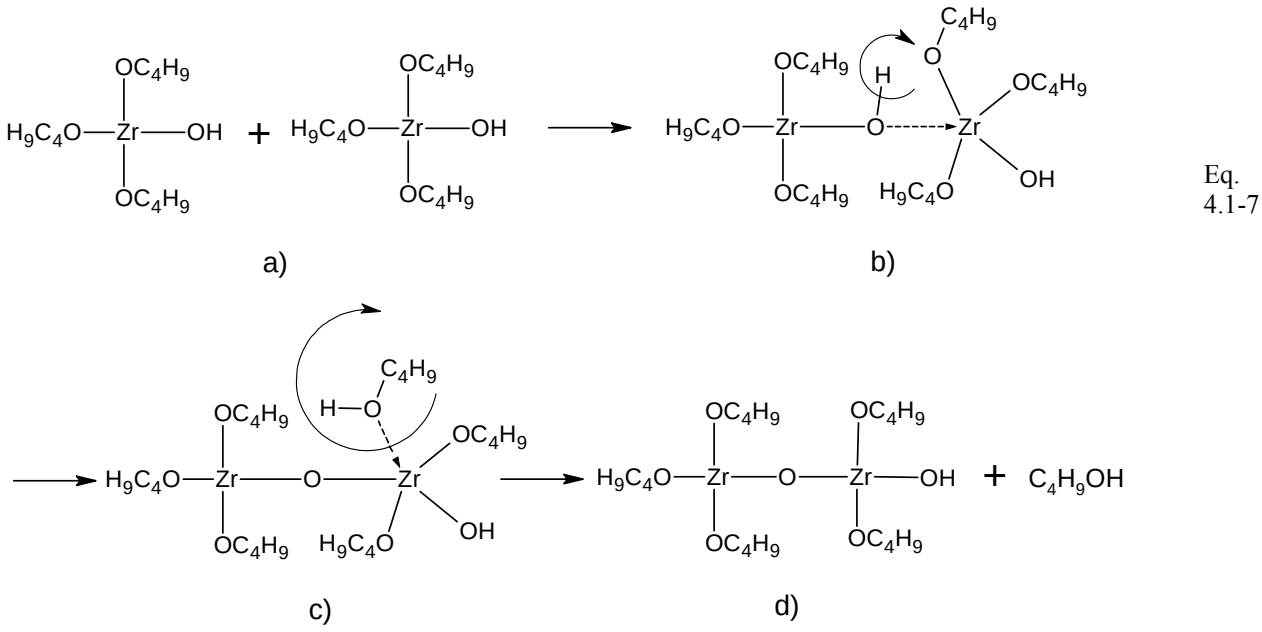

Eq. 4.1-7

Table 4.1-5. Partial charges of constituent parts of zirconium n-butoxide during condensation.

	Species	δ(M)	δ(O)	δ(OC_4H_9)	δ(C_4H_9OH)	δ(OH)
c)	$Zr_2(OC_4H_9)_5(O)(OH)(C_4H_9OH)$	0.6393	-0.4804	-0.0830	0.0071	-0.3903
d)	$Zr_2(OC_4H_9)_5(O)(OH)$	0.6394	-0.4803	-0.0816		-0.3901

Next we evaluate the stability of the intermediate products along the condensation pathway. We consider that alcoxolation is the condensation pathway for species with 50% exchanged groups ($Zr(OR)_2(OH)_2$)) or oxolation for the species with 100% of exchanged groups ($Zr(OH)_4$). By the equimolar reaction between an alkoxide group (Eq. 4.1-8) or a hydroxyl group (Eq. 4.1-9) and a hydroxyl group an oxo-bridge is formed. As the condensation proceeds, a partially or fully condensed compound can be obtained. Examples of ($Zr(OR)_2(OH)_2$)) species with a 50% and 100% extent of condensation are given by Eq. 4.1-10 and Eq. 4.1-11, respectively. Similarly they are written for ($Zr(OH)_4$) in Eq. 4.1-12 and Eq. 4.1-13.

$\equiv(OR) + \equiv(OH) \rightarrow \equiv O\equiv + ROH$ -alcoxolation Eq. 4.1-8

$\equiv(OH) + \equiv(OH) \rightarrow \equiv O\equiv + H_2O$ -oxolation Eq. 4.1-9

$Zr(OR)_2(OH)_2) \rightarrow ZrO(OR)(OH) + ROH$ -50% extent of condensation Eq. 4.1-10

$ZrO(OR)(OH) \rightarrow ZrO_2 + ROH$ -100% extent of condensation Eq. 4.1-11

$(Zr(OH)_4) \rightarrow ZrO(OH)_2 + H_2O$ -50% extent of condensation Eq. 4.1-12

$ZrO(OH)_2 \rightarrow ZrO_2 + H_2O$ -100% extent of condensation Eq. 4.1-13

To follow the partial charge during the condensation of zirconium in PZ precursor, a molecular formula is needed for calculation. By the EXAFS analysis of the PZ sol (starting from lead acetate and zirconium n-butoxide) it has been established that there are links between Pb and Zr through oxo-bridges and that Zr species tend to form polynuclear oxo-alkoxide complexes (Malic *et al.*, 1999; Ion *et al.*, 2007). To write a molecular formula for the PZ precursor, we chose the only polynuclear oxo-alkoxide complex described in the literature: $Zr_{13}O_8(OR)_{36}$ (Morosin, 1977), and our quantitative NMR results, which reveal that about 25% of acetate groups were removed as butyl-acetate. The PZ species can be described by the formula $Pb_{13}Zr_{13}O_{14.5}(OC_4H_9)_{29.5}(O_2C_2H_3)_{19.5}$.

The partial charges were calculated for products hydrolysed with $R_w = 2$ and $R_w = 4$. Partial charges of zirconium n-butoxide, partially hydrolysed $(Zr)(OC_4H_9)_2(OH)_2$ and fully hydrolysed $(Zr)(OH)_4$ were calculated for comparison. Figure 4.1-6 presents the partial charge during the condensation of zirconium n-butoxide product and PZ n-butoxide-based precursor product hydrolysed with $R_w = 2$ and $R_w = 4$.
The partial charges of constituents of products hydrolysed with $R_w = 4$ represent the upper value that the constituents can reach.

The partial charge of Zr in $(Zr)(OC_4H_9)_2(OH)_2$ increases during the condensation, leading to even more reactive species. The partial charge of OH groups decreases, but still remains negatively charged, so we assume that the condensation stops only due to steric hindrance.

The partial charge on Zr atom in the PZ precursor with a 50 % exchanged groups is 8 % higher that in the $Zr(OR)_2(OH)_2$, which leads to the conclusion that the reactivity of the Zr species in the case of PZ precursor is higher towards hydrolysis and condensation than in the $Zr(OR)_2(OH)_2$ species. The partial charges of the OH groups are negative in all cases, meaning that they are nucleophilic enough to initiate further condensation.

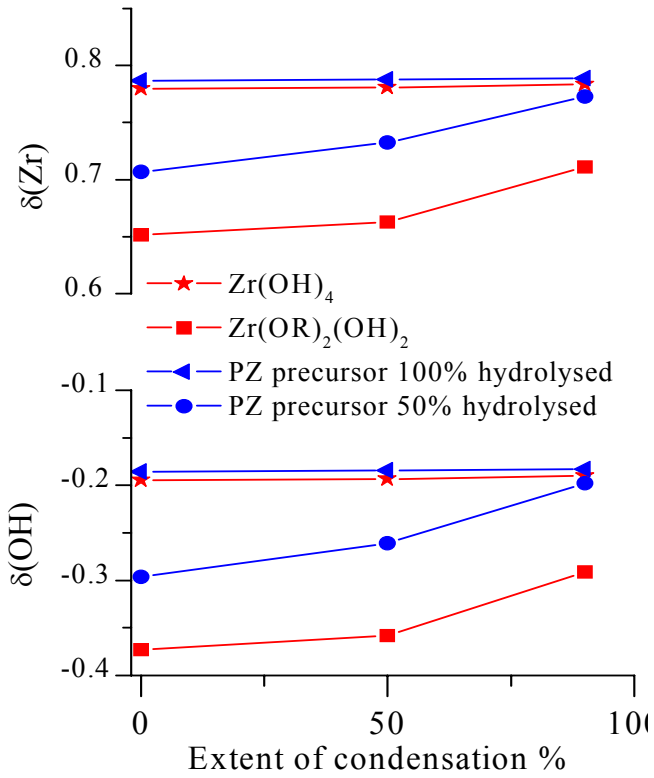

Figure 4.1-6 Partial charges of Zr and OH groups of zirconium n-butoxide species and of PZ n-butoxide-based precursor during the condensation reaction.

4.1.4 Characterization of the hydrolysed sol

For particle size determination by Photon Correlation Spectroscopy (PCS) the PZ sol of 0.02M concentration (PZ_d10) was hydrolysed with a molar ratio of Pb : H_2O : NH_3 = 1 : 15 : 5.

The mean diameter obtained from the particle size distribution measured by PCS and the zeta potential of PZ_d10 hydrolysed products, are presented in Table 4.1-6. The mean diameter for the PZ_d10 is about 400 nm. The zeta potential is -1.76 eV, which is very close to zero. Such value can favour particles agglomeration. In order to learn about the agglomerates measured by PCS, the hydrolysis product was diluted for ten times (PZ_d100). The particle size, measured in the diluted hydrolysis product is around 120 nm for PZ_d100. We therefore conclude that the PZ_d10 hydrolysed product is composed of about 120 nm particle sized which represent the building units of the about 400 nm particles determined by PCS (Table 4.1-6).

Table 4.1-6.Mean diameter and zeta potential of PZ samples.

Sample	PCS – Mean diameter (nm)	Zeta potential (mV)
PZ_d10	441.3	-1.76
PZ_d100	116.6	-*

* - Zeta potential was not determined.

The sedimentation curve was traced by recording the evolution of the transmission profile at each 10 s under 1000 rpm for PZ_d10 hydrolysis products. The evolution of the interface liquid/solid *vs.* time is plotted in Figure 4.1-7. The separation of the solid mass starts from the top of the cell and the destabilization of the system is fast. The solid phase compacts to 77.18 % of the initial volume. The sedimentation curve could be transformed into particle size distributions by knowing the hydrodynamic density and refractive index of the powder. Unfortunately neither parameter is known for the investigated sample.

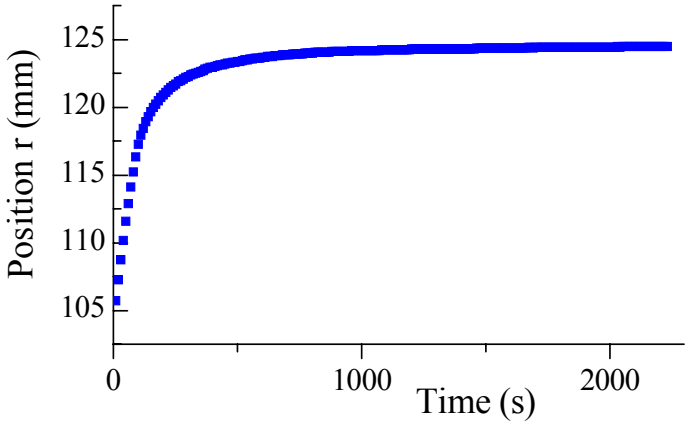

Figure 4.1-7. Evolution of the interface liquid/ solid *vs.* time during centrifuging under 1000 rpm of PZ_d10 hydrolysis product.

4.1.5 Morphology and thermal decomposition of $PbZrO_3$ precursor powders

Table 4.1-7 presents the specific surface area (SSA) and the calculated d_{BET} of the PZ product hydrolysed in neutral medium with R_w = 2, 5 and 15 and in alkaline medium with R_w = 15, and dried at 150 °C, and from the PZ_d10, hydrolyzed in alkaline medium with R_w = 15 and dried at 90 °C. The SSA increases with the increase in the R_w from 0.53 m^2 / g in the PZ2 dried powder to 118.13 m^2 / g in the PZ15 dried powder, which corresponds to diameters of 3760 nm and 16 nm, respectively. There is a strong decrease in the diameter of the particles, for more then two hundred times when changing the R_w from 2 to 15. The d_{BET} slightly decreases with the increase of pH from 16 nm, when hydrolysed in neutral medium, to 11 nm, when hydrolysed in alkaline medium. The d_{BET} increases with the decrease of the concentration: from 11 nm when prepared from the 0.2 M sol to 425.5 nm in the case of the 0.02 M sol. The ten times dilution of the sol leads to an almost forty time increase in the d_{BET}. The d_{BET} of PZ precursor powder prepared from the 0.02 M sol is in agreement with the mean diameter of the particles of the hydrolysed sol (PZ_d10) equal to 441.13 nm, determined by PCS (Table 4.1-6).

Table 4.1-7. SSA and d_{BET} of PZ precursor powders prepared in neutral medium at R_w = 2, 5 and 15 and in alkaline medium at R_w = 15 and dried at 150 °C and from the 0.02 M (PZ_d10) in alkaline medium with R_w = 15 and dried at 90 °C.

	PZ2	PZ5	PZ15	11PZ15	PZ_d10 (0.02 M)
SSA (m^2 / g)	0.53	32.45	118.41	178.13	4.70
d_{BET} (nm)	3760	61	16	11	425.5

Figure 4.1-8. presents the cumulative particle size distribution of the dried PZ precursor powders prepared at different hydrolysis conditions and in Table 4.1-8 the particle diameter distributions and their polydispersity indices ((D_{90}-D_{10}) / D_{50}) are summarised. The median size of the particles falls between 5 μm and 10 μm, with a random distribution regardless of the hydrolysis conditions. The polydispersity index (Eq. 3.3-2) increases with the increase of R_w from 3.06 in PZ2 to 4.33 in PZ15 and with the increase of the pH to 6.43.

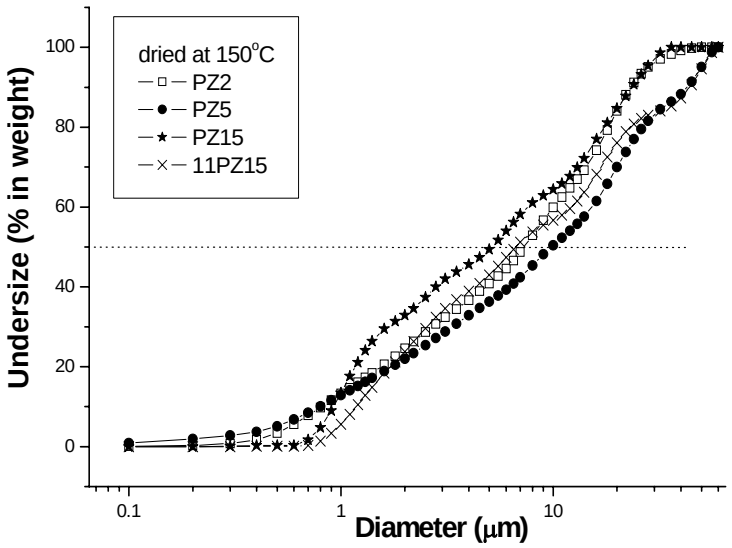

Figure 4.1-8. Cumulative particle size distributions of PZ powders, hydrolysed at different conditions, after drying at 150 °C, determined by laser particle size analyzer.

Table 4.1-8. Particle diameter distributions and calculated polydispersity indices $(D_{90}\text{-}D_{10})/D_{50}$ of PT2, PT5, PT15 and 11PT15 powders, dried at 150 °C.

	PZ2	PZ5	PZ15	11PZ15
D_{10} (μm)	0.81	0.79	0.92	1.18
D_{50} (μm)	7.30	9.80	5.12	6.66
D_{90} (μm)	23.22	42.66	23.51	44.01
$(D_{90}\text{-}D_{10})/D_{50}$	3.06	4.27	4.33	6.64

Table 4.1-9 presents the summarised D_{50} and d_{BET} of the dried PZ powders prepared with different hydrolysis conditions, and their ratio expressed as the agglomeration factor F_{ag}. The F_{ag} increases with the increase of R_w and pH, from $F_{ag} = 1.94$ at $R_w = 2$ to $F_{ag} = 320$ at $R_w = 15$ and to $F_{ag} = 605$ when powders were prepared in alkaline medium. This means that by increasing R_w and the pH the particle size decreases but at the same time the particles form agglomerates, the smaller their particle sizes the stronger their agglomeration.

Table 4.1-9 Summary of the D_{50} and d_{BET} of the dried PZ powders prepared with different hydrolysis conditions, used to calculate F_{ag}.

	PZ2	PZ5	PZ15	11PZ15
D_{50} (μm)	7.30	9.80	5.12	6.66
d_{BET} (nm)	3760	61	16	11
F_{ag}	1.94	160	320	605

Figure 4.1-9 presents the SEM images of a few drops of PZ_d10 hydrolysis product, spread on a substrate allowing the solvent to evaporate to get a dried sample. At a low magnification the gel fragments are observed. Their surface is smooth, with mainly linear cracks. At a higher magnification, we can observe that the PZ_d10 fragments are composed of tiny fibres connected in a dense network. A direct agreement with the values from the PCS measurements where the mean diameter was 441 nm (Table 4.1-6), is not confirmed, but the SEM images confirm that the large fragments are composed of small units.

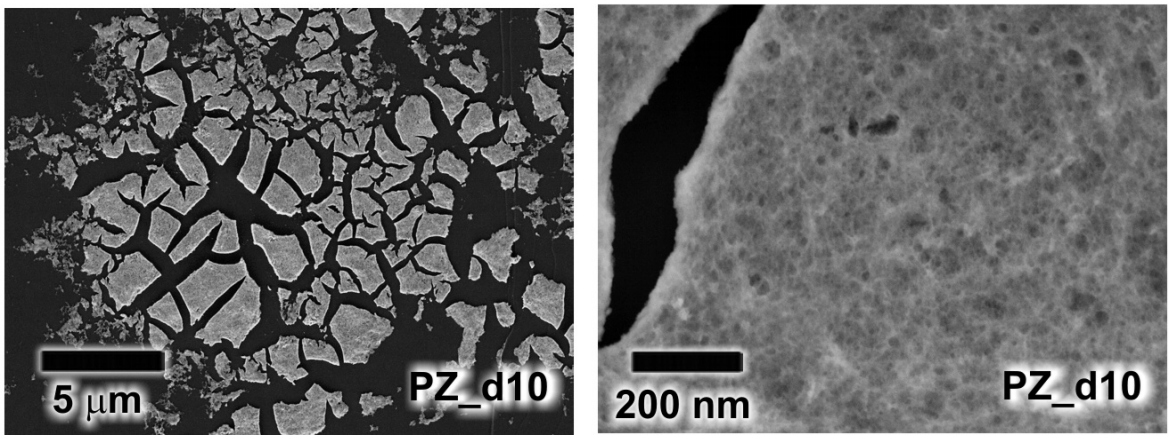

Figure 4.1-9. SEM images of a few drops of the dried PZ_d10 hydrolysis product.

The SEM micrographs of the PZ precursor powders, dried at 150 ^{o}C, are presented in Figure 4.1-10. At a lower magnification, the PZ powders comprise of coarse fragments which are noticeably larger in the case of PZ2 and PZ5, and mixtures of fragments and smaller particles in the case of PZ15 and 11PZ15. A direct correlation between the median size of the fragments determined by laser granulometry and the size of the fragments from SEM cannot be established (Table 4.1-8). At a higher magnification, we can see that the fragments are densely packed in the case of the powders prepared with the low R_w (PZ2, PZ5), while small particles with a low amount of porosity can be observed on the surface of PZ15 and 11PZ15 fragments. The result is in agreement with the increase of SSA with the increase of R_w and pH. The SSA of the PZ2 sample was about two hundreds times lower than that of the PZ15 and even more for 11PT15, 0.53 m^2 / g *vs.* 118 m^2 / g or 178 m^2 / g, respectively (Table 4.1-7).

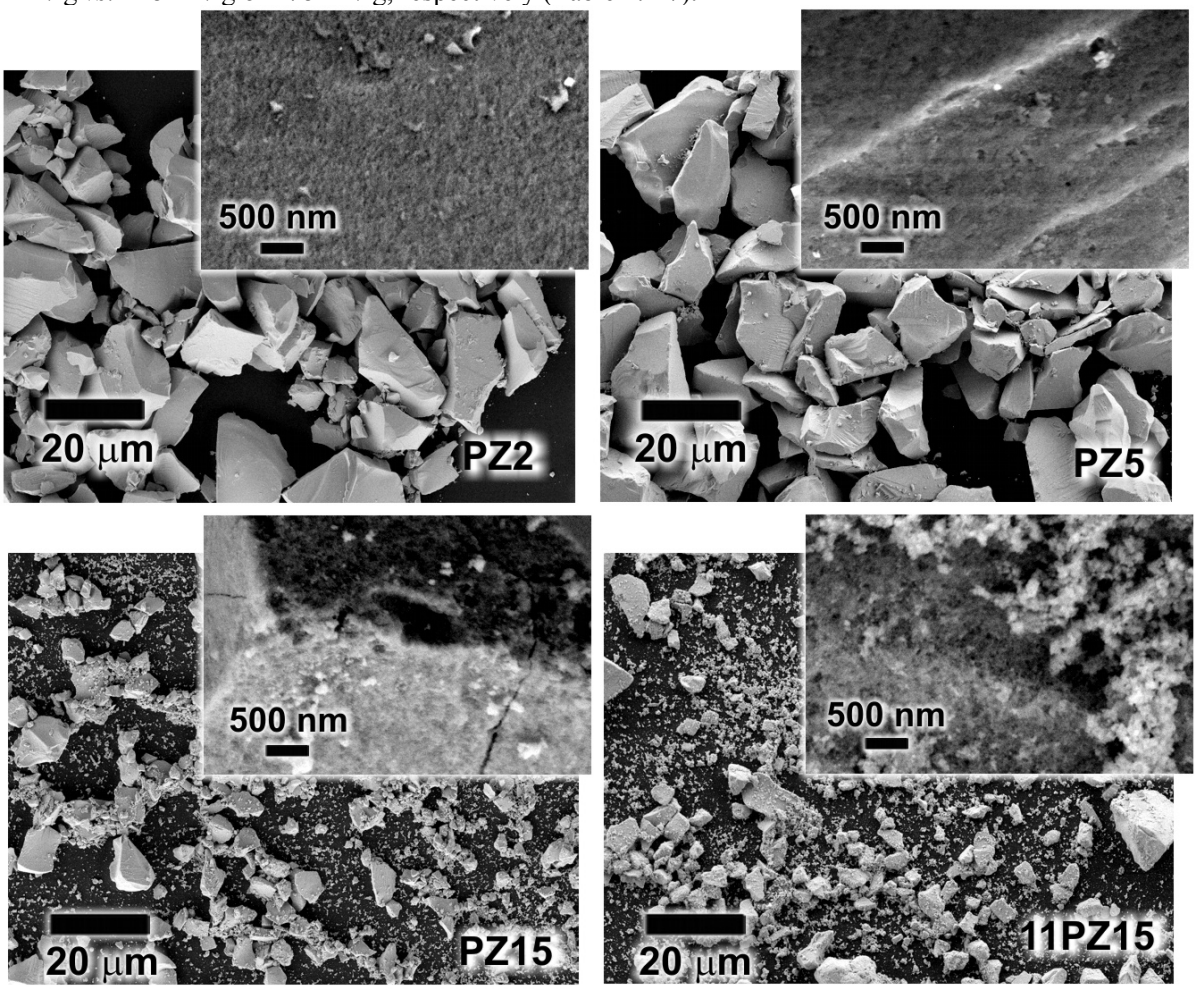

Figure 4.1-10. Morphology of the PZ2, PZ5, PZ15 and 11PZ15 powders dried at 150 ^{o}C. Insets show the morphology of powders observed at a higher magnification.

The thermal decompositions of the dried hydrolysis products PZ2, PZ5, PZ15 and 11PZ15 were investigated using the TG / DTA / EGA (Figure 4.1-11). The total mass losses of all samples were about 16 %. The PZ2 and PZ5 decomposed in three steps, while the PZ15 and the 11PZ15 decomposed in only two steps. The mass losses and gases evolved in different temperature ranges are summarized in Figure 4.1-12. In the first step, in the temperature range 25 - 220 ^{o}C, all samples lose between 5 % and 6 % of their mass. There is no thermal event in their DTA curves, while the main evolved gas in this temperature range is water and we attribute the mass loss between 25 ^{o}C and 220 ^{o}C to the removal of water and/or possibly residual solvent (Figure 4.1-12). Between 220 ^{o}C - 400 ^{o}C, there is 8 % to 10 % mass loss. The mass loss increases with the increase of R_w used at hydrolysis: 8.41 % in case of PZ2, 9.77 % in PZ5 and 10.71 % in PZ15. A slight decrease was observed in the case of sample prepared at high pH: 10.31 % mass loss in 11PZ15. The DTA curves present an exothermic peak in the same temperature range with maximum between 285 ^{o}C and 306.5 ^{o}C. The intensity of the DTA peak is strongly correlated with the mass loss in this temperature range; the higher the mass loss, the higher the intensity of the DTA peak. The EGA analysis revealed the evolution of H_2O, acetone and CO_2 (Figure 4.1-12). We attribute the mass loss in this temperature range to the decomposition of both alkoxide and acetate groups in agreement to the earlier reports (Patil *et al.*, 1968). In the temperature range 400 ^{o}C- 640 ^{o}C only the PZ2 and PZ5 lose 2.78 % and 0.58% mass, respectively. The mass losses are accompanied by exothermic peaks, a pronounced one in PZ2 and a very weak peak in PZ5. The CO_2 evolves from the PZ2 sample and in traces from the PZ5, as a consequence of decomposition of carbonaceous residues (Figure 4.1-12).

To gain further insight into the processes occurring during the organic groups' decomposition, the samples were quenched at 460 ^{o}C. This temperature is marked by a dotted line in Figure 4.1-11.
We noticed that the quenched powders have different colours: the PZ2 powder is black, the PZ5 is dark yellow, while the PZ15 and 11PZ15 powders are light yellow (Figure 4.1-13).
The XRD patterns of the PZ samples quenched at 460 ^{o}C are presented in Figure 4.1-14. The XRD patterns reveal reflections of lead in the amorphous matrix in PZ2, only traces in PZ5, while the PZ15 and 11PZ15 are amorphous, without any traces of lead.

The PZ dried powders and powders heated at 400^{o}C were examined by FTIR between 2500 cm^{-1} and 400 cm^{-1} (Figure 4.1-15). The spectrum of Pb acetate is presented for comparison. The bands between 1400 cm^{-1} and 1520 cm^{-1} are attributed to the symmetric and asymmetric vibrations of the acetate groups (Nakamoto, 1997). In the dried powders the two absorption bands of acetate groups are the most prominent. By heating the powders, the acetate bands disappear and weak bands between 1250 cm^{-1} and 1450 cm^{-1}, which can be assigned to the carbonate groups, are noticed (Gatehouse *et al.*, 1958). There are no significant differences related to the hydrolysis conditions, but small differences in the shape of the bands of the samples prepared with low R_w (2, 5) and R_w = 15 can be noticed.

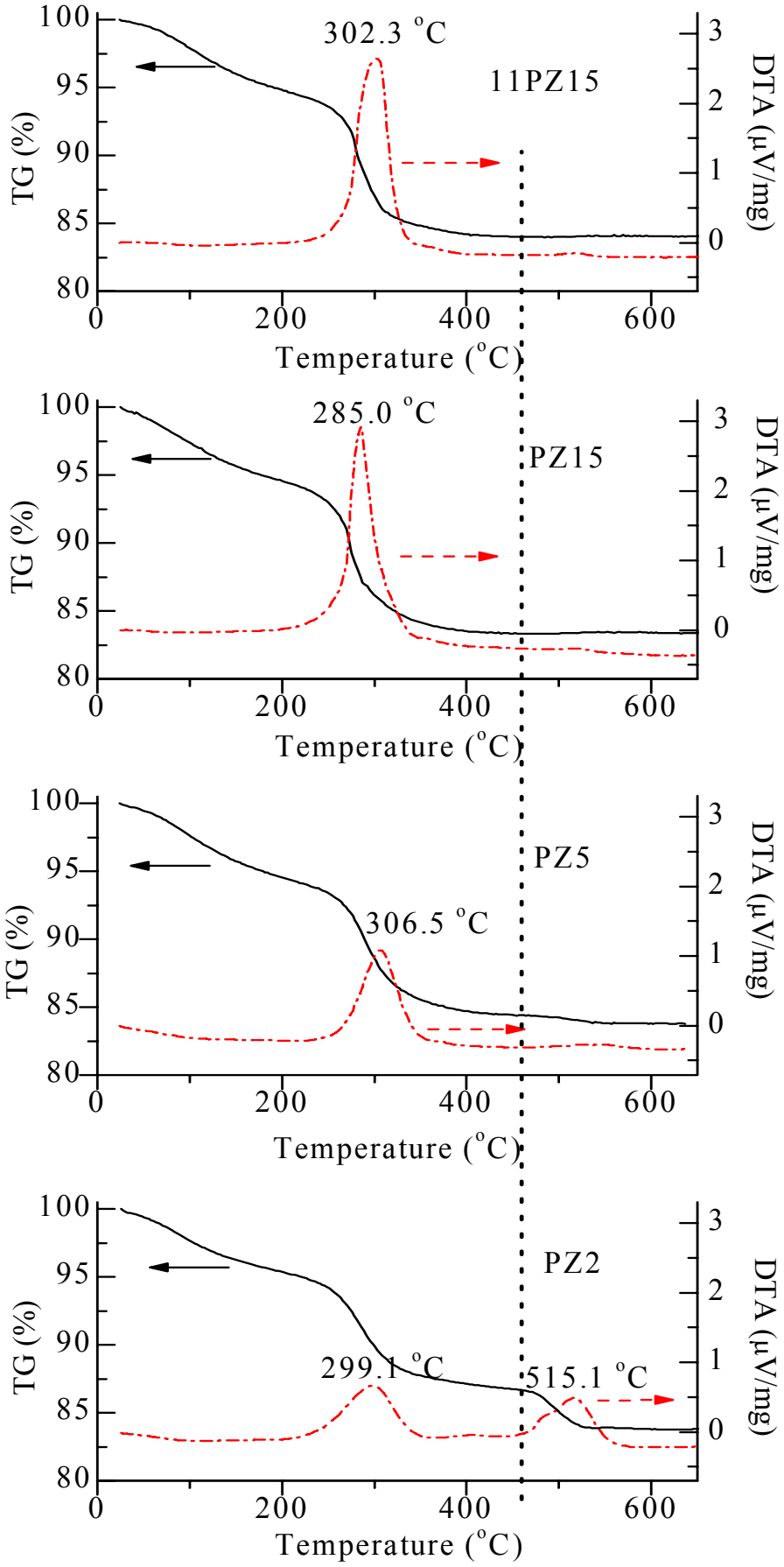

Figure 4.1-11. TG-DTA curves of PZ dried powders, prepared with different hydrolysis conditions. The dotted line marks the temperature of 460 °C.

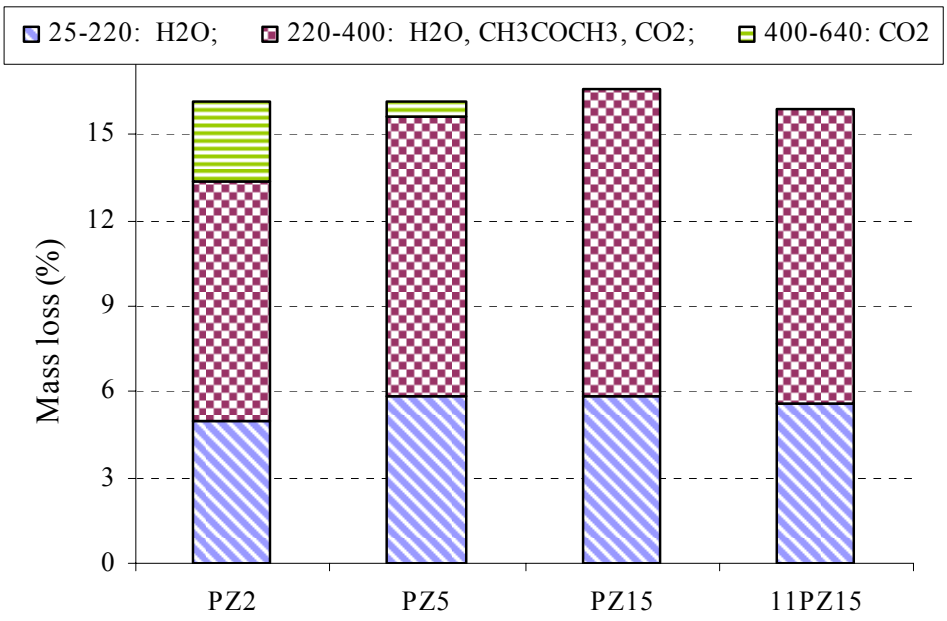

Figure 4.1-12. Mass losses and evolved gas of the PZ precursors determined by TG/EGA in different temperature ranges.

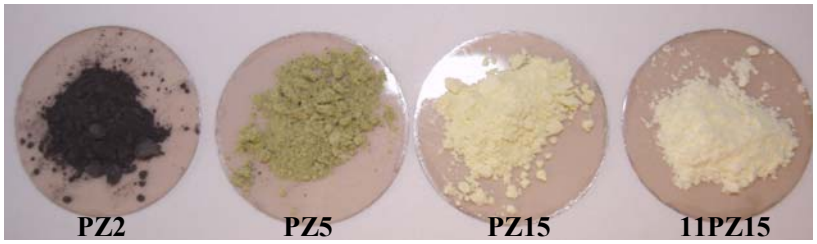

Figure 4.1-13. Colour of the PZ powders after quenching at 460 °C.

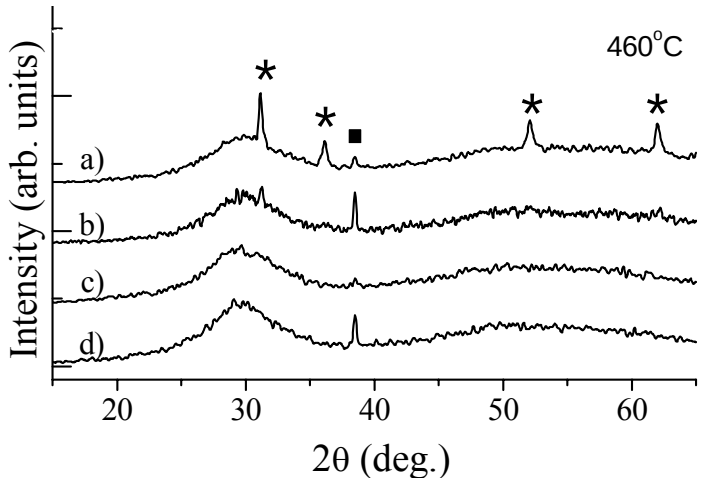

Figure 4.1-14. XRD patterns of a) PZ2, b) PZ5, c) PZ15, d) 11PZ15 powders quenched at 460 °C; ■–sample holder, *- lead (JCPDS 65-2873).

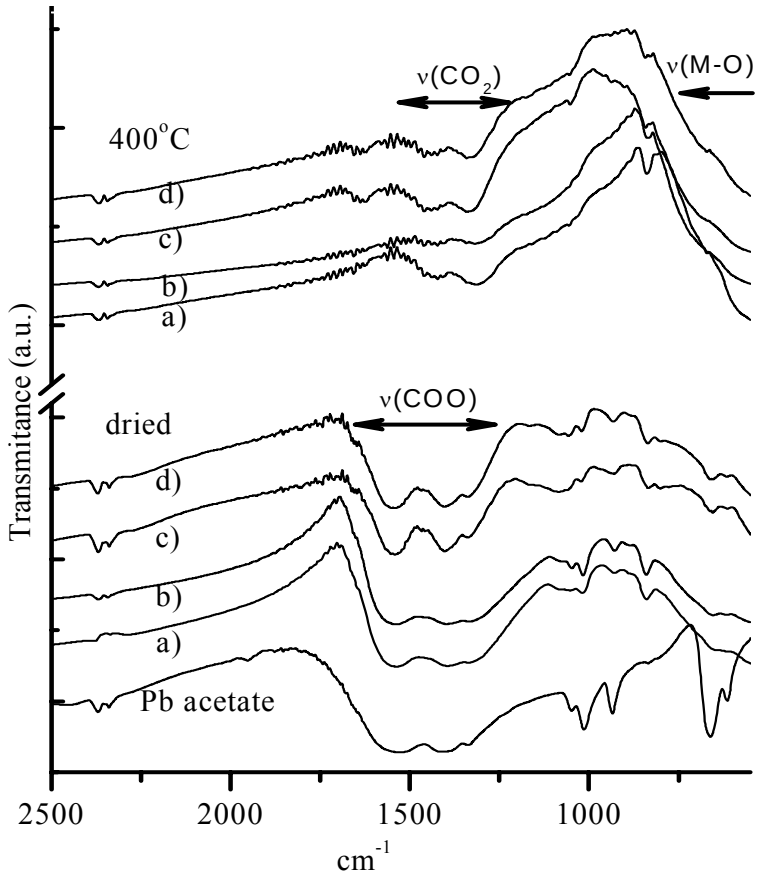

Figure 4.1-15. The IR spectra of Pb acetate and a) PZ2, b) PZ5, c) PZ15, d) 11PZ15 dried powders, and heated at 400 °C and at 700 °C for 1h.

It has been reported for transition-metal (TM) alkoxides that monolithic gels form at low R_w and at low pH, while particulate gels or precipitates form at high R_w and at high pH (Livage *et al.*, 1988). In our case we relate the different microstructures of the powders to the different pathways of hydrolysis and condensation induced by changes in R_w and pH.

We assume that, like in the case of TM alkoxides, the translucent gel formed during the hydrolysis of PZ precursor with $R_w = 2$ and 5, is composed of polymer chains, similar to those formed in the PZ_d10 (Figure 4.1-9), which during drying yield dense gel fragments (Figure 4.1-10) with low SSA (Table 4.1-7). Increasing the amount of water of hydrolysis at $R_w = 15$ the semi-solid gel, composed of cross-linked polymers, yields a product with fine particles - d_{BET} is 16 nm, but they are strongly agglomerated. When hydrolysed in alkaline medium, the obtained gel fragments contain pores, the d_{BET} is 11nm, but the particles are also agglomerated (Table 4.1-9). The concentration of the sol seems to have a strong effect on determining the particle nucleation and growth and on the type of condensation products: polymer chains or cross-linked polymers. The median size of agglomerates is not sensitive to these changes; however the polydispersity index and especially the factor of agglomeration increase with the increase of R_w and pH, the latter increases from 2 for PZ2 to 320 and 605 for PZ15 and 11PZ15, respectively.

All powders have similar mass losses in the interval 25-220 °C (Figure 4.1-12), while obviously the powders with the low SSA (Table 4.1-7) and comprising of dense gel fragments (Figure 4.1-10) decompose differently, as compared to the porous powders with the high SSA (Table 4.1-7). The low mass losses of PZ2 and PZ5 powders are strongly correlated with the existence of a third step of the decomposition (Figure 4.1-12). A similar, two-step decomposition of the organic groups has been reported by Malic *et al.* (Malic *et al.*, 1997) for the propoxide-derived PZ precursor ($R_w = 10$). The presence of acetate groups in the dried powders and their complete decomposition in the powder heated at 400°C/1h was confirmed by the IR analysis (Figure 4.1-15).

Next we noticed that the powders quenched at 460°C have different colours and the XRD analysis of these powders reveals that lead is segregated from the amorphous matrix in PZ2, giving a black colour to the powder. Traces of lead are found in PZ5 and consequently the colour is dark yellow, while the samples prepared at $R_w = 15$, amorphous on the level of XRD, are light yellow.

We propose that when heating the PZ2 precursor, its dense microstructure hinders the access of air to

the interior of the gel fragments. As a consequence the organic groups only partially oxidize and thermally decompose to carbonaceous residues. These are oxidized to produce CO_2 only upon further heating in the second step of the organic decomposition (Figure 4.1-12). The locally formed reducing atmosphere causes a partial reduction of Pb^{2+} to lead (Figure 4.1-14). Malic *et al.* (Malic *et al.*, 1992) Polli *et al.* (Polli, *et al.*, 1995) and Coffman *et al.* (Coffman *et. al.*, 1996) also report the presence of lead in the process of thermal decomposition of PZT precursors and Cakare *et al.* (Cakare *et al.*, 2000) in case of PZ precursor and they also relate this to the reducing environment created by organics burn-out which provides a low oxygen partial pressure during heating. The cracks and pores of the fragments of the PZ precursors hydrolysed at R_w=15 facilitate the access of air and the oxidation of organic groups in one step, as confirmed by the thermal analysis (Figure 4.1-12). We conclude that in the porous microstructure the partial pressure of oxygen is high enough to avoid partial reduction of Pb^{2+} as in the case of PZ2 and PZ5 (Figure 4.1-14).

4.1.6 Crystallization and morphology of the $PbZrO_3$ powders

XRD patterns of the PZ samples heated at different temperatures are presented in Figure 4.1-16. All the PZ powders heated at 500 °C crystallize in the pyrochlore-type phase and at 700 °C in the perovskite phase with some traces of pyrochlore, irrespective of the hydrolysis conditions.

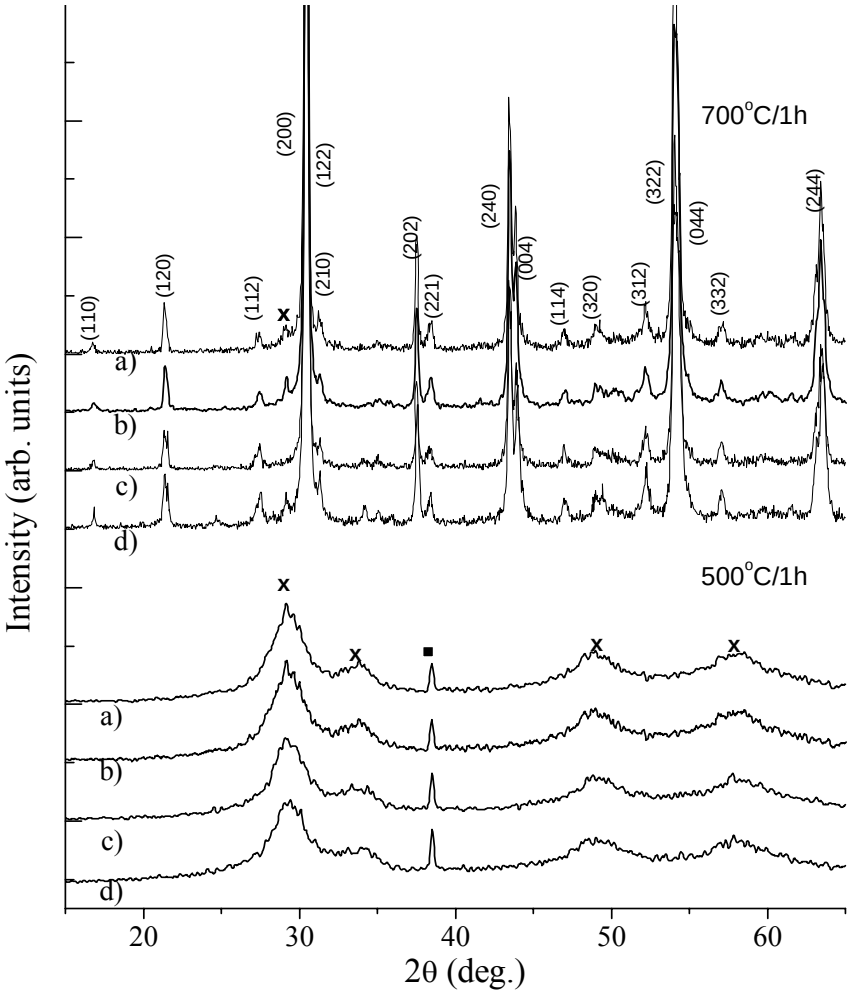

Figure 4.1-16. XRD patterns of a) PZ2, b) PZ5, c) PZ15, d) 11PZ15 powders heated at 500 °C / 1h and 700 °C / 1h. The main reflections of the perovskite (JCPDS 87-0570) phase are marked; ■–sample holder, x–pyrochlore type phase.

The X-ray pattern of PZ_d10 powder heated at 700°C/1h shows the reflections of pure perovskite phase. PZ_d10 crystallizes in perovskite phase with orthorhombic syngony without any secondary phases (Figure 4.1-17).

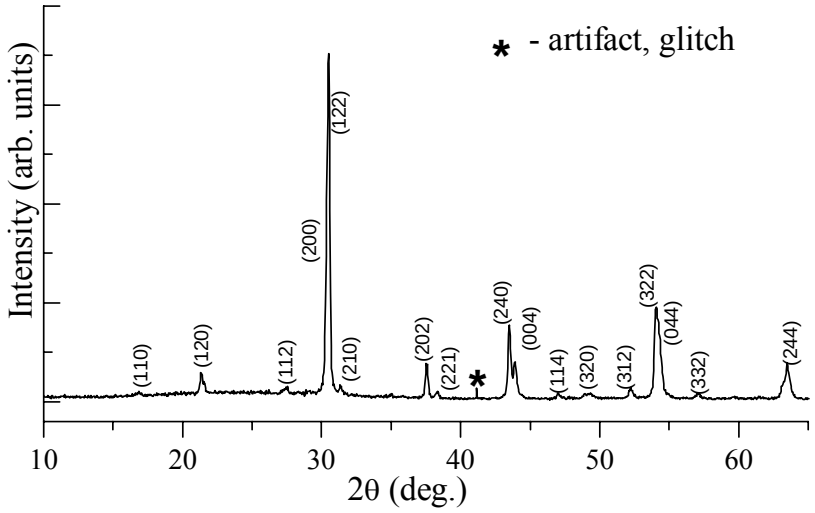

Figure 4.1-17. X-ray pattern of PZ_d10 after heating at 700 °C/1h. The main reflections of the perovskite phase (JCPDS 87-0570) are marked.

By heating to 500°C/1h the powders crystallize in the pyrochlore-type phase regardless of the hydrolysis conditions (Figure 4.1-16). This metastable phase has been usually observed in the sol-gel synthesis of PZ or Zr-rich PZT (Polli *et al.*, 2000). It transforms to the perovskite phase at higher temperatures, at about 700 °C. However, traces of pyrochlore phase still remain. The powder prepared from strongly diluted sol crystallizes in pure perovskite phase. We propose that a better mixing of the sol with water and therefore a more homogenous nucleation and growth of the particles take place.

Table 4.1-10 presents the SSA and the calculated d_{BET} of the PZ powders heated at 700 °C/1h, prepared in neutral medium at R_w = 2, 5 and 15 and in alkaline medium at R_w = 15 and from the 0.02 M (PZ_d10) in alkaline medium with R_w = 15. The SSA increases with the increase of the R_w from 0.01 m^2/g in the PZ2 powder to 8.46 m^2/g in the PZ15 dried powder, which correspond to d_{BET} of 6710 nm and 88 nm, respectively. The same relation was observed in the dried powders, just that their diameters were 3760 nm and 16 nm, respectively (Table 4.1-7). There is a slight decrease in the d_{BET} with the increase of pH from 88 nm, when hydrolysed in neutral medium, to 58 nm, when hydrolysed in alkaline medium. We observe the increase of d_{BET} of PZ 15 and 11PZ15 powders upon heating in relation to the value obtained for the dried powders: 16 nm and 11 nm (Table 4.1-7), and we attribute it to the interparticles sintering. There is an almost 5 times increase in the d_{BET} of the powder prepared from the 0.02 M sol and dried at 90 °C, compared to the powder prepared from the 0.2 M sol, namely from 58nm to 290 nm.

Table 4.1-10. SSA and d_{BET} of PZ powders, prepared in neutral medium at R_w = 2, 5 and 15 and in alkaline medium at R_w = 15 and from the 0.02 M (PZ_d10) in alkaline medium with R_w = 15, after heating at 700 °C / 1h.

	PZ2	PZ5	PZ15	11PZ15	PZ d10 (0.02M)
SSA (m^2 /g)	0.01	0.27	8.46	12.83	2.6
d_{BET} (nm)	6710	2679	88	58	288.4

The d_{50} (7.28 μm) of 11PZ15 was used to evaluate the agglomeration of the particles by calculating the agglomeration factor $F_{ag}= d_{50}/d_{BET}$ =125.

The SEM micrographs of PZ powders heated at 700 °C are collected in Figure 4.1-18. At a lower magnification the PZ powders comprise of coarse fragments. At a higher magnification, the fragments are the most densely packed in the case of the PZ2. A low amount of porosity can be observed on the surface of PZ5 fragments, while the PZ15 powders are highly porous. At a higher magnification the 11PZ15 powder consists of agglomerates of fine particles. The SEM micrographs agree well with the SSA. By increasing the R_w an increase in porosity is observed, while a dramatic change is noticed by the pH increase: gel fragments at neutral pH and agglomerated particles in alkaline medium. In the latter case the SEM images agree very well with the d_{BET} = 58 nm (Table 4.1-10).

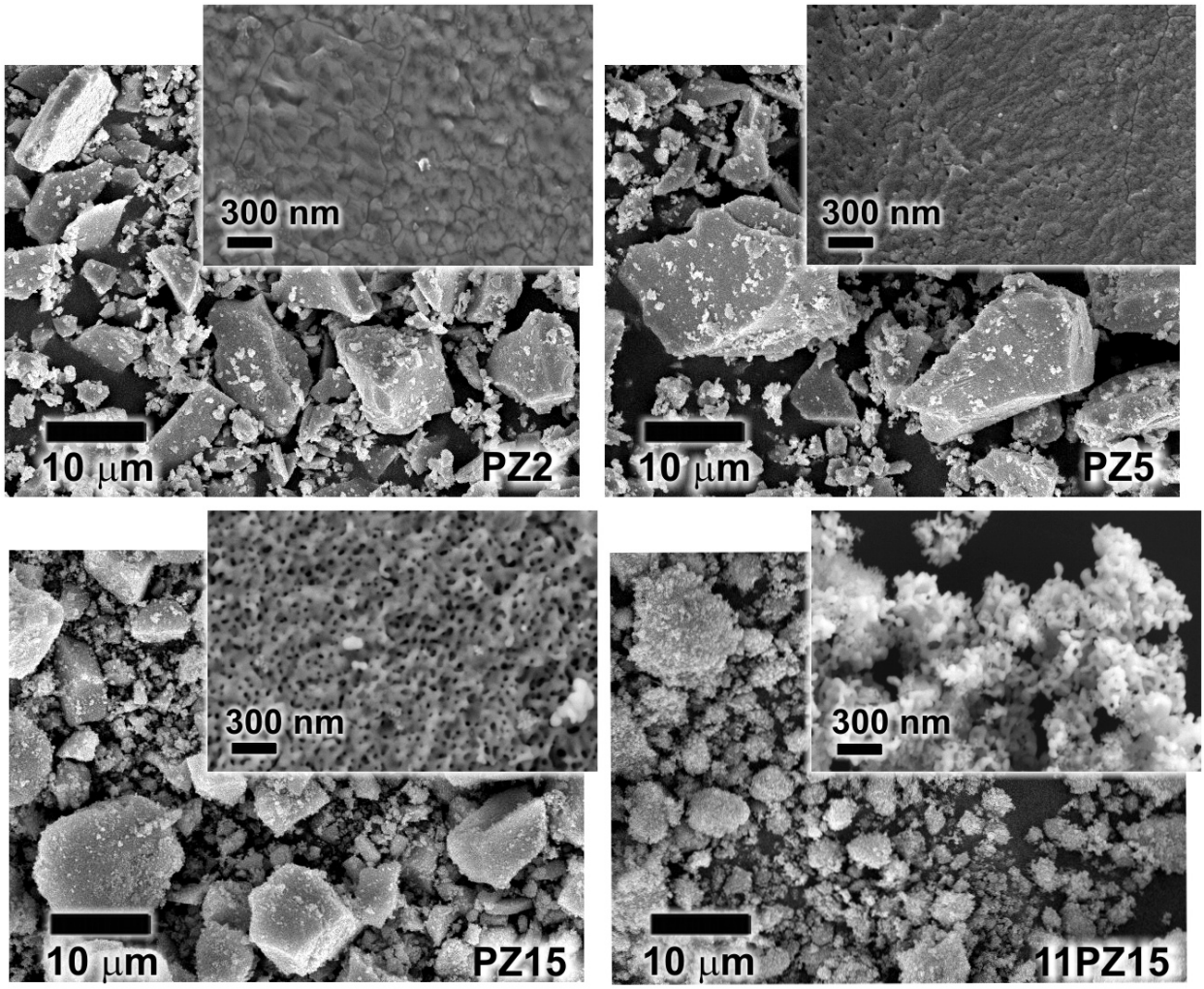

Figure 4.1-18. SEM micrographs of PZ powders heated at 700 ^{o}C / 1h. Insets show the morphology of powders observed at higher magnification.

Figure 4.1-19 presents the morphology of the PZ_d10 powder, heated at 700 ^{o}C / 1h. The powder is composed of densely packed fragments.

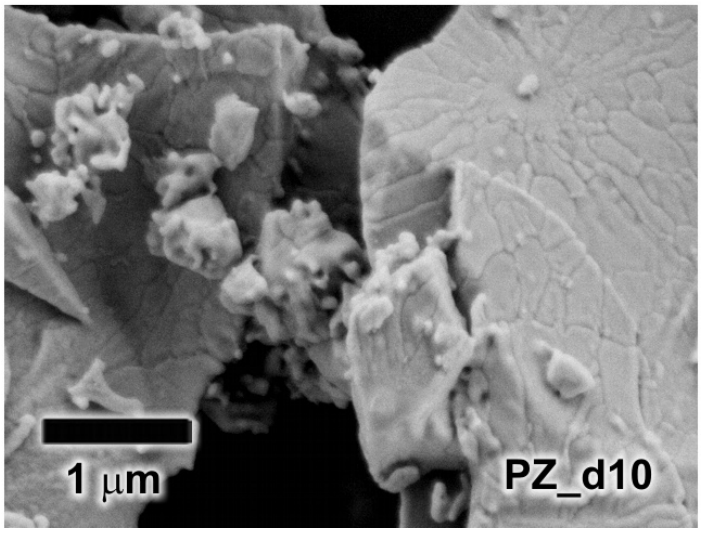

Figure 4.1-19. SEM micrograph of PZ_d10 powder heated at 700 ^{o}C / 1h.

4.1.7 Summary

The summary of the most important results is presented in Table 4.1-11.

In the PZ sol, the lead environment is dominated by two Pb-O-Zr links, while the initial Zr n-butoxide dimers transform during thermolysis to Zr oxo-alkoxides, where the Zr environment is populated by six Zr-O-Zr links. A reaction takes place between lead and zirconium species leading to a complex, most probably with a homogenous distribution of the Pb-O-Zr and Zr-O-Zr links.

By using the partial charge model we established that the Pb-Zr species, formed during synthesis, are more reactive towards hydrolysis and condensation then the simple zirconium n-butoxide.

In the next step the sol is hydrolysed. The PZ_d10 hydrolysed product is composed of about 120 nm particles which represent the building units of the about 400 nm agglomerates.

After hydrolysis of the sol with different amounts of water, in neutral and alkaline medium, one of the two Pb-O-Zr links is lost while Zr -Zr correlations are retained over the whole range of the R_w values. However, the SSA and the morphology of the dried hydrolysis products strongly depend of the hydrolysis conditions, pH and sol concentration and drying conditions. Dense gel fragments with a low SSA are obtained at low R_w or at low sol concentration (0.02 M) while increasing the R_w, and using a more concentrated sol (0.2 M), the powders present high SSA and are composed of cracked and porous fragments. Upon heating, the organic groups are removed in two steps for the precursors prepared at $R_w = 2$ and 5, and in one step at $R_w = 15$. In the precursors, prepared at $R_w = 2$ and 5, the organic groups decompose with intermediate carbonaceous residues forming a locally reducing atmosphere, and as a consequence metallic lead segregates. A porous structure of the precursors prepared at $R_w = 15$ facilitates the oxidation of organic groups and in this case the homogeneity is retained at the XRD level. The results agree also with the case with a uniform distribution of the Pb-O-Zr and Zr-O-Zr links, otherwise a heterogeneous distribution would lead to phase segregation of all powders.

In the 11PZ_H powder (heated at 400 ^oC / 1h) the Pb-Zr correlation is completely lost, while the Zr-Zr correlations remain almost unchanged. In contrast to the prevailing belief, atomic homogeneity is not entirely lost in the process of hydrolysis and condensation but in a further step by heating. To regain the homogeneity during crystallization into the desired perovskite phase of the end product, both Pb and Zr environments have to suffer major changes. Since the pyrochlore phase predominantly develops in the PZ or Zr-rich PZT precursors, and the Zr-Zr correlations are stable at temperature higher than 400 ^oC / 1h, it is rational to suppose that Zr-Zr links are the reason for the persistence of the transitory pyrochlore-type phase upon thermal treatment (Malic *et al.*, 1999). After heating at 700 ^oC the powders crystallize in the perovskite phase with traces of pyrochlore at all hydrolysis conditions. When prepared from a diluted sol the powder crystallizes in pure perovskite phase. We propose that by better mixing of the sol with water a more homogenous nucleation and growth of the particles take place.

The morphology of the dried powder is correlated to the heated powder morphology, the dense gel fragments prepared at low R_w or the porous fragments prepared at high R_w are preserved. Densification or particle growth takes place in all the powders, being reflected in the decrease of the SSA from the dried to the heated powders. Agglomerated particles of about 60 nm are obtained only when the hydrolysis is performed at $R_w = 15$ in alkaline medium and from a 0.2 M sol.

Table 4.1-11 Summary of the most important results obtained in the synthesis of PZ powders.

C (M)	pH	R_w	EXAFS			PCS – median size (nm)	TG/DTA	XRD			d_{BET} (nm)		Morphology	
			Sol	dried	Heated			460 °C	500 °C	700 °C	dried	700 °C	dried	700 °C
0.2	Neutral	2			-	-	3 steps	Pb+Am	Py	PE+ Py tr.	3760	6710	Dense fragments	Dense fragments
		5	2x Pb-O-Zr	1x Pb-O-Zr	-	-	3 steps	Pb+Am	Py	PE+ Py tr.	61	2679	Dense fragments	Dense + some pores
		15	+	+	-	-	2 steps	Am	Py	PE+ Py tr.	16	88	Dense + some cracks	Porous fragments
	Alkaline	15	6x Zr-O-Zr	5x Zr-O-Zr	2x Pb-O 5x Zr-O-Zr	-	2 steps	Am	Py	PE+ Py tr.	11	58	Dense + cracks + particles	Agglomerated particles
0.02	Alkaline	15	-	-	-	441	-	-	-	Pure PE	425	288	Dense network of tiny fibres	Dense fragments
	dilution10x					116	-	-	-	-	-	-	-	-

Am – amorphous phase,
Py tr. – traces of pyrochlore phase,
PE – perovskite phase.

4.2 $PbTiO_3$

This chapter describes the characterization of the dried precursor and $PbTiO_3$ (PT) powder. The sol was prepared from lead acetate and titanium n-butoxide in butanol and hydrolysed in neutral medium with different R_w. For selected experiments a ten times diluted (0.02M) sol was used.

The hydrolysis of the sol occurred quickly, resulting in a white suspension, not withstanding the conditions of hydrolysis. The hydrolysis products were dried at 150 ^oC, when prepared from the sol of 0.2 M concentration, and at 90 ^oC / 48h, when prepared from the sol of 0.02 M concentration and heated at 500 ^oC / 1h and 700 ^oC / 1h.

Evaluation of the stability of species at hydrolysis and condensation was made using a partial charge model. The agglomeration state of the particles of the hydrolysed sol was investigated. The impact of the hydrolysis conditions on the morphology, decomposition pathway, and the homogeneity of the powders were assessed.

4.2.1 Synthesis of the sol

The sol was prepared from lead acetate and titanium n-butoxide in butanol. The lead acetate does not dissolve in n-butanol but a clear sol is obtained by reactive dissolution of lead acetate in titanium butoxide in butanol with butyl-acetate elimination (Eq. 4.1-1) (Chandler *et al.*, 1993). The reaction is written for one acetate group and one alkoxide group.

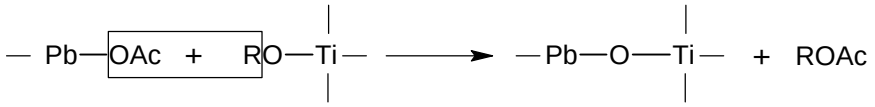

Eq. 4.2-1

where Ac = $OCCH_3$ and R = C_4H_9 in the present work.

The butyl-acetate forms an azeotrope mixture with n-butanol with the molar ratio 0.23 : 0.77 and b.p. = 116.8 ^oC (Gmehling *et al.*, 2008). The amount of acetates removed by distillation as butyl-acetate was determined by NMR analysis. From 20 millimoles acetate about 50% is removed, while the rest of 50 % remains in the sol, confirming that the reactive dissolution occurred.

4.2.2 Hydrolysis and condensation –stability of species

We calculate the partial charges of titanium butoxide undergoing hydrolysis and condensation by the same approach as in the case of PZ (Chapter 4.1.3). By the reaction with a water molecule, one butoxide group of titanium butoxide is replaced with a hydroxyl group (Eq. 4.1-6) (Livage *et al.*, 1988).

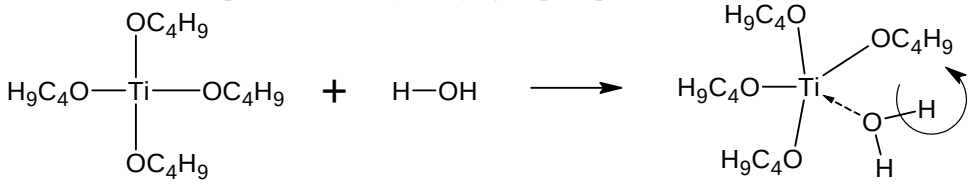

Eq. 4.2-2

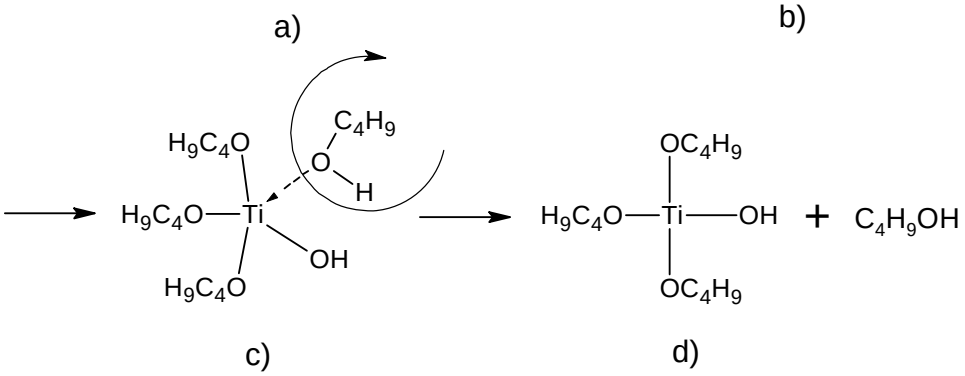

Electronegativity of Ti is 1.32 which is slightly higher than the value of Zr (Table 4.1-3). The partial charges of the titanium species involved in the hydrolysis reaction (Eq.4.2-2) are presented in Table 4.2-1. The species a)-d) (Table 4.2-1) present the titanium species and their charges during the three steps of hydrolysis (Eq. 4.2-2). The nucleophilic addition of the water molecule to the positively charged titanium atom ($\delta = 0.6064$) produces an increase in the partial charge of the metal from $\delta = 0.6064$ to $\delta = 0.6132$ and a decrease of the partial charge of the butoxide group from $\delta = -0.1516$ to $\delta = -0.0785$. The positively charged C_4H_9OH ($\delta = 0.0119$) is the leaving group. Since in the d) species the partial charge on the metal ($\delta = 0.6136$) is higher then the initial partial charge ($\delta = 0.6064$), this leads to an increase of the species' reactivity.

The hydrolysis product can be expressed by the formula $M(OR)_{4-x}(OH)_x$, where M=metal atom and OR=alkoxide group.

For the case where $x = 2$, equivalent to $R_w = 2$ in our experimental conditions, there is a 50 % exchange of the (OR) groups with (OH) groups, while for $x = 4$, the exchange is 100 %.
The species $Ti(OC_4H_9)_2(OH)_2$ and $Ti(OH)_4$ (e) and f) in Table 4.2-1 correspond to titanium species with 50 % and 100 % exchanged groups and their partial charges. An increase in the partial charge of the metal is observed, $\delta = 0.6261$ for the species with 50 % exchanged groups and even higher $\delta = 0.7559$, for the species where the groups were 100% exchanged, in comparison to the $\delta = 0.6064$ for $Ti(OC_4H_9)_4$. For the same species there is a decrease in the partial charge of the OH groups, but they still remain negatively charged.

Table 4.2-1. Partial charges of titanium species during hydrolysis.

	Species	δ(M)	δ(O)	$\delta(OC_4H_9)$	$\delta(C_4H_9OH)$	δ(HOH)	δ(OH)
a)	$Ti(OC_4H_9)_4$	0.6064	-0.4843	-0.1516			
b)	$Ti(OC_4H_9)_4(HOH)$	0.6132	-0.4801	-0.0785		-0.2992	
c)	$Ti(OC_4H_9)_3(HO)(C_4H_9OH)$	0.6132	-0.4801	-0.0785	0.0119		-0.3897
d)	$Ti(OC_4H_9)_3(HO)$	0.6136	-0.4799	-0.0747			-0.3892
e)	$Ti(OC_4H_9)_2(OH)_2$	0.6261	-0.4722	0.05854			-0.3716
f)	$Ti(OH)_4$	0.7559	-0.3925				-0.1889

The metal atom is highly prone to the nucleophilic attack of the (OH) groups due to its positive charge. In the next step the hydrolysed products undergo a condensation reaction (Eq. 4.2-3). The reaction is written for the specific case of one alkoxide group exchanged with an OH group ($x = 1$). In the steps a) and b) the titanium species forms an intermediate state where the coordination number of titanium increases by one.

The c) and d) species and their partial charges during condensation are presented in Table 4.2-2. The group C_4H_9OH has a positive charge, which means that it has the highest probability to be a leaving group so we conclude that the alcoxolation is the condensation pathway (Eq. 1.1-2). The partial charge of the metal atom slightly increases from $\delta = 0.6136$ to $\delta = 0.6139$ leading to intermediate products which are even more reactive. At the same time the partial charge of the OH group slightly decreases from c) to d) but as it is still negative, we expect that it further initiates condensation.

Next we evaluate the stability of the species along the condensation pathway. We consider that alcoxolation is the condensation pathway for species $Ti(OR)_2(OH)_2$) with 50 % of exchanged groups or oxolation for the species $Ti(OH)_4$ with 100 % of exchanged groups. As the condensation proceeds, a partially or fully condensed compound can be obtained in both cases as described by Eq. 4.2-4 to Eq. 4.2-7.

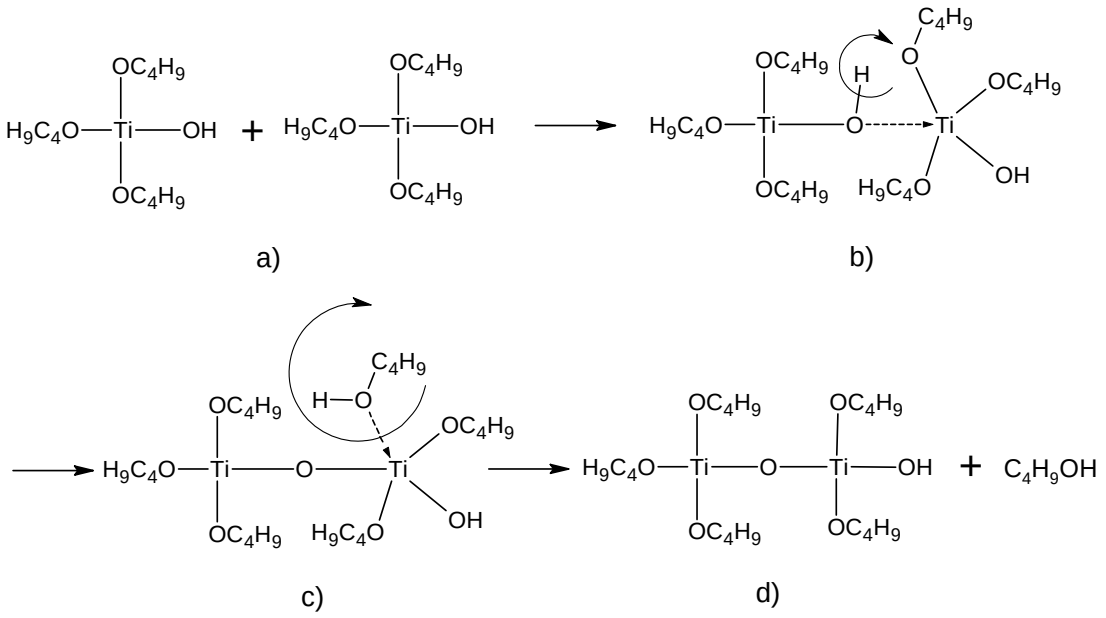

Eq. 4.2-3

Table 4.2-2. Partial charges of titanium species during condensation.

	Specie	δ(M)	δ(O)	δ(OC_4H_9)	δ(C_4H_9OH)	δ(OH)
c)	$Ti_2(OC_4H_9)_5(O)(OH)(C_4H_9OH)$	0.6136	-0.4799	-0.0747	0.0159	-0.3892
d)	$Ti_2(OC_4H_9)_5(O)(OH)$	0.6139	-0.4797	-0.0718		-0.3888

$Ti(OR)_2(OH)_2) \rightarrow TiO(OR)(OH) + ROH$ -50% extent of condensation Eq. 4.2-4

$TiO(OR)(OH) \rightarrow TiO_2 + ROH$ -100% extent of condensation Eq. 4.2-5

$Ti(OH)_4 \rightarrow TiO(OH)_2 + H_2O$ -50% extent of condensation Eq. 4.2-6

$TiO(OH)_2 \rightarrow TiO_2 + H_2O$ -100% extent of condensation Eq. 4.2-7

To follow the partial charge during the condensation of the PT precursor, a molecular formula is needed for calculation. It has been established by EXAFS analysis that titanium butoxide forms trimers (Babonneau *et al.*, 1988) and this oligomeric structure is retained even after the hydrolysis of the PT precursor (Malic *et al.*, 1997). Based on the literature data and our quantitative NMR results, which show that about 50% of acetates groups were removed as butyl-acetate, we propose the following formula of the PT precursor: $Pb_3Ti_3O_3(OC_4H_9)_{12}(O_2C_2H_3)_3$.

Figure 4.2-1presents the partial charges of Ti atoms and OH groups as the function of the extent of condensation for titanium n-butoxide hydrolysed with $R_w = 2$ $Ti(OC_4H_9)_2(OH)_2$ and for fully hydrolysed product $Ti(OH)_4$, and for the PT n-butoxide-based precursor species hydrolysed at the same conditions. The partial charge of titanium atoms increases during the condensation, which means that the intermediate products are more reactive species. The partial charge of OH groups decreases, but still remains negatively charged and prone to further condensation, so we assume that the condensation stops only due to the steric hindrance.

The partial charge on Ti atoms in the PT precursor is 5.5 % higher than in the $Ti(OR)_2(OH)_2$, meaning that the reactivity of the PT precursor is higher than of the $Ti(OR)_2(OH)_2$ species. The partial charges of the OH groups are negative in all cases, and they can initiate further condensation.

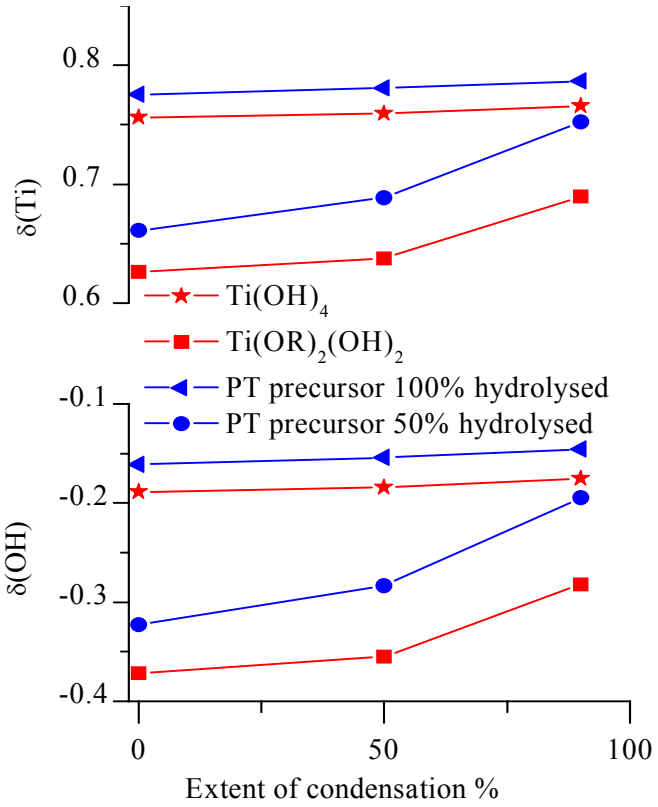

Figure 4.2-1 Partial charges of Ti atoms and OH groups in titanium n-butoxide and PT n-butoxide-based precursor, both partially and fully hydrolysed, during the condensation reaction.

4.2.3 Characterization of the hydrolysed product

We hydrolysed the PT sol with 0.02 M concentration (PT_d10) with a molar ratio of $Pb(OAc)_2$: H_2O: NH_3 = 1:15:5.

Table 4.2-3 presents the mean diameter obtained from the particle size distribution measured by photon correlation spectroscopy (PCS) and the zeta potential of PT hydrolysed product. The mean diameter for the PT_d10 sample is about 500 nm. The zeta potential is 4.20 mV. To get insight into the agglomeration state of the particles, the hydrolysed sol was diluted ten times (PT_d100). The particle size in the diluted sample was 87 nm and we assume that these are the building units of the about 500 nm agglomerates (Table 4.2-3). The surface charge of the particles approaches zero (Table 4.2-3) and it is reasonable to conclude that they agglomerate.

Table 4.2-3. Mean diameter determined by PCS and zeta potential of PZ and PT samples.

Sample	PCS – Mean diameter (nm)	Zeta potential (mV)
PT_d10	524.7	4.20
PT_d100	87.0	- *

* - Zeta potential was not determined.

The sedimentation curve was traced during centrifuging by recording the evolution of the interface liquid/solid at each 10 s under 1000 rpm for PT_d10 hydrolysis product (Figure 4.2-2). The separation of the solid mass started from the top of the cell and the destabilization of the system was fast. The solid phase compacted to 72.21% of the initial volume.

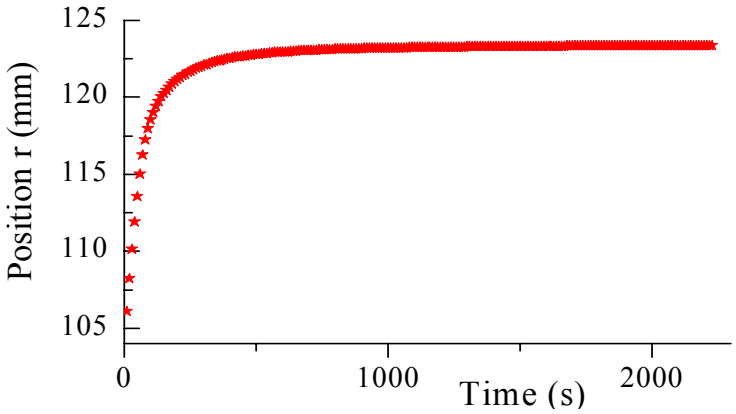

Figure 4.2-2. Evolution of the interface liquid/ solid *vs.* time during centrifuging under 1000 rpm of PT_d10 hydrolysis product.

4.2.4 Morphology and thermal decomposition of $PbTiO_3$ precursor powder

Table 4.2-4 presents the specific surface area (SSA) and the calculated particle size d_{BET} of the PT precursor powders, prepared from the 0.02 M sol and 0.2 M sol i.e. PT_d10 and 11PT15, respectively. In both cases the hydrolysis was performed in alkaline medium with a molar ratio $Pb(OAc)_2$:H_2O:NH_3=1:15:5 and the samples were dried at 90°C and 150°C, respectively. The d_{BET} decreases with the increase of the concentration: from 21 nm in the case of 0.02 M sol (PT_d10) to 8 nm when prepared from the 0.2 M sol (11PT15). The d_{BET} of the PT precursor powder prepared from the 0.02 M sol is about four times smaller than the mean diameter of the particles of the hydrolysed sol (PT_d100) determined by PCS (Table 4.2-3), suggesting that the particles determined by PCS are agglomerates of even smaller particles.

Table 4.2-4. SSA and d_{BET} of PT precursor powders prepared by hydrolysis of the 0.02 M (PT_d10) and 0.2 M sol (11PT15) in alkaline medium with a molar ratio $Pb(OAc)_2 : H_2O : NH_3 = 1 : 15 : 5$ and dried at 90 °C and 150°C, respectively.

	PT_d10 (0.02M)	11PT15 (0.2M)
SSA (m^2/g)	93.4	247.0
d_{BET} (nm)	21.4	8.0

The cumulative particle size distributions determined by laser granulometry of the dried PT precursor powders prepared at different hydrolysis conditions are collected in Figure 4.2-3. In Table 4.2-5 the distribution of the particle diameters and the polydispersity indices are summarised. The median size of the particles falls in the same range, about 1.5 μm, regardless of the hydrolysis conditions, however the polydispersity index is about 10 at R_w = 2 and 15 and narrower at R_w = 5. The powder 11PT15 has the narrowest particle size distribution.

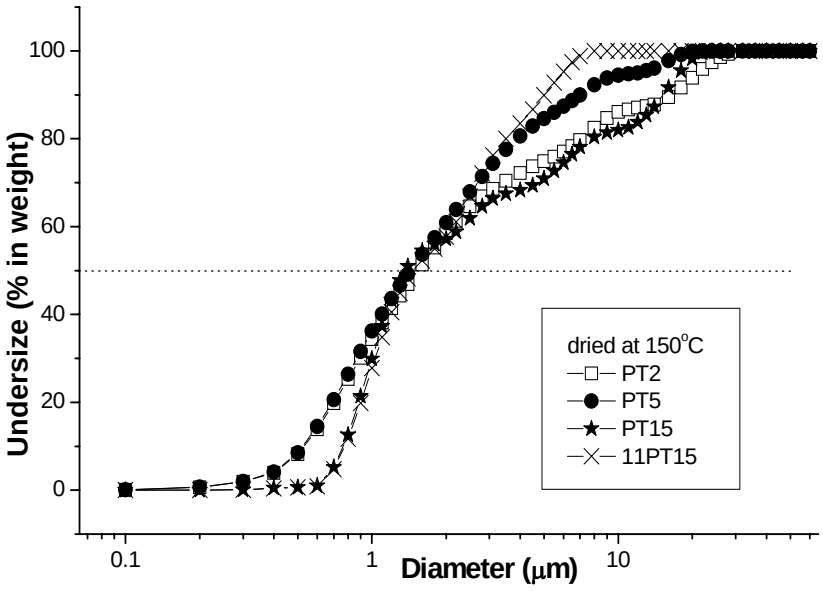

Figure 4.2-3. Cumulative particle size distributions of PT2, PT5, PT15 and 11PT15 powders, dried at 150°C, determined by laser particle size analyzer.

Table 4.2-5. Particle diameter distributions and the calculated polydispersity index (D_{90}-D_{10}) / D_{50} of PT2, PT5, PT15 and 11PT15 powders, dried at 150 °C.

	PT2	PT5	PT15	11PT15
D_{10} (μm)	0.53	0.52	0.76	0.77
D_{50} (μm)	1.54	1.43	1.37	1.49
D_{90} (μm)	16.45	6.98	15.19	5.02
(D_{90}-D_{10})/D_{50}	10.33	4.51	10.53	2.85

Figure 4.2-4 presents the SEM images of a few drops of PT_d10 hydrolysis product, spread on a substrate with allowing the solvent to evaporate. The low magnification image presents the distribution of the fragments after the solvent evaporation. The surface is rough, with irregular cracks. At a higher magnification, the PT_d10 fragments form a very porous network of particles of a few tens of nm in size, in agreement with the d_{BET}= 20 nm (Table 4.2-4). A similar microstructure of the gel fragments of lead titanate dried gel, prepared from lead acetate and titanium isopropoxide in 2-methoxyethanol and hydrolysed in alkaline medium, was observed by Dey *et al.* (Dey *et al.*, 1987). They proposed that the cross-linked condensation of the species lead to a coarse microstructure.

The SEM images of the dried PT2, PT5, PT15 and 11PT15 powders prepared from the 0.2 M sol are presented in Figure 4.2-5. The PT powders are comprised of agglomerates of particles. A slight decrease in the size of the particles with increasing the R_w and pH is noticed. The 11PT15 powder has an agglomeration factor, which is the ratio of D_{50}/d_{BET}, F_{ag} =186. A good agreement between the SEM images and the narrow particle size distribution measured by laser granulometry (Table 4.2-5) is evident especially for the 11PT15 powder.

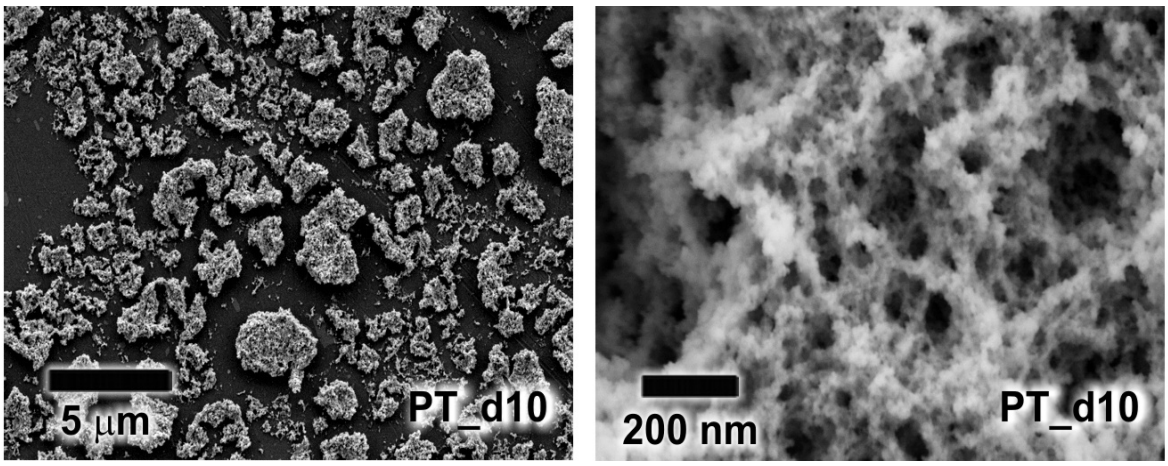

Figure 4.2-4. SEM images of a few drops of PT_d10 hydrolysis product, spread on a substrate, after evaporation of the solvent.

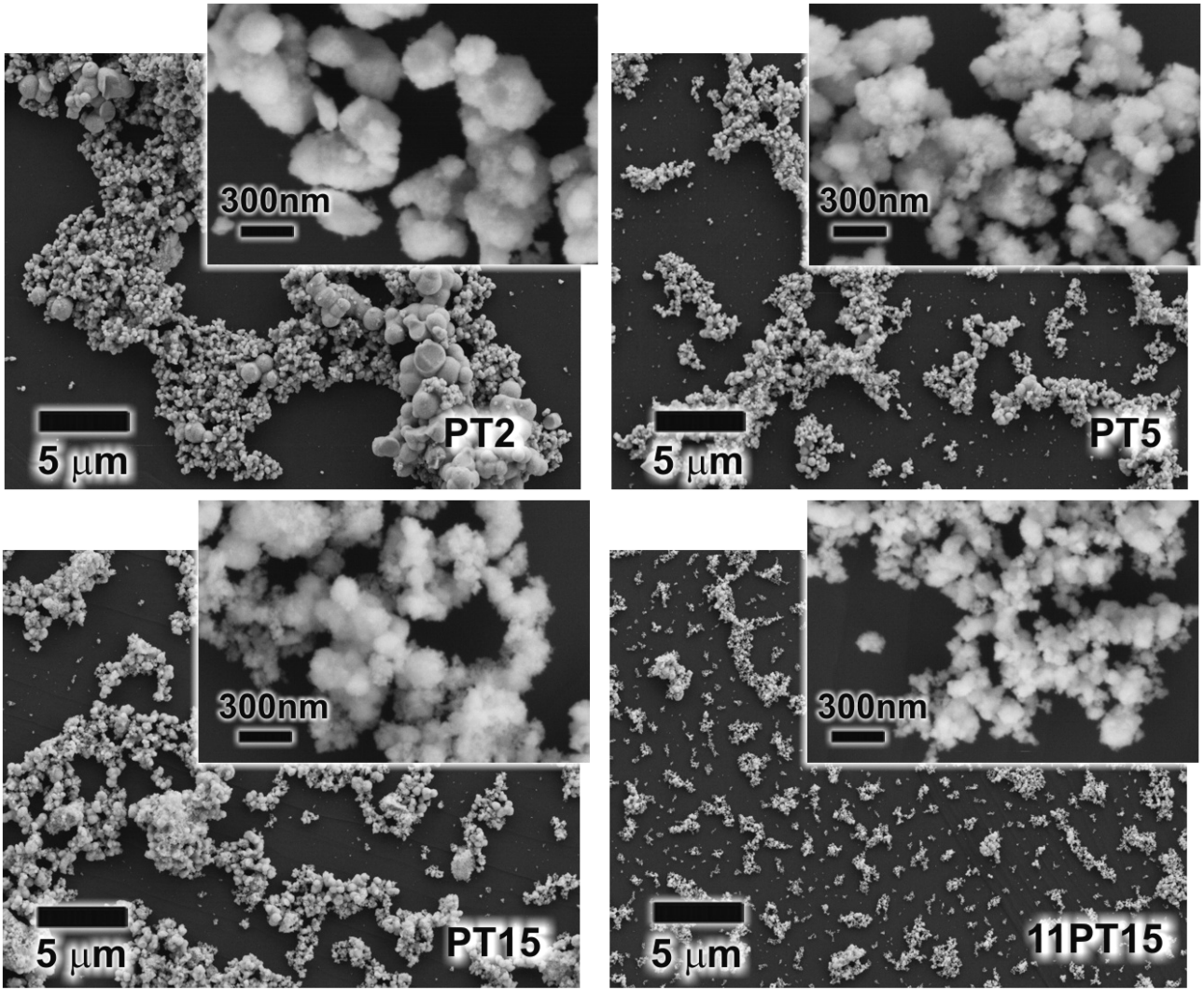

Figure 4.2-5. SEM micrographs of PT dried powders, prepared at different hydrolysis conditions. Insets show the morphology of the powders observed at a higher magnification.

Cross-linked polymers, particulate gels or precipitates are expected to form when R_w>1 is used for hydrolysis (Livage *et al.*, 1988), while with increasing the pH even more strongly cross-linked polymers are expected to form. The powders have similar median sizes of about 1.5 μm, they slightly differ in particle size and particle size distribution (Figure 4.2-3, Table 4.2-6), so we can conclude that there is a

small impact of the hydrolysis conditions on the powder morphology.

The dried powders PT2, PT5, PT15 and 11PT15, were investigated by TG/DTA/EGA (Figure 4.2-6). The mass losses and gases evolved in different temperature ranges are summarized in Figure 2.2–7. The PT2, PT5, PT15 and the 11PT15 decompose in only two steps upon heating to 650 ^{o}C; the total mass losses are about 12 – 13 %. In the first step, between 25 ^{o}C and 220 ^{o}C (mass loss about 3-4 %) water and possibly some solvent accompanied by traces of by-products are evolved. No pronounced endothermic peak is present in the DTA curves. The mass loss occurring between 220 ^{o}C and 400 ^{o}C is accompanied by the main exothermic peak at about 290 ^{o}C for all PT samples. An additional week exothermic peak is noticed at 218.6 ^{o}C in PT 2. The evolved gases, H_2O, CO_2 and acetone confirm the decomposition of the acetate (Patil *et al.*, 1968) and oxidation of the alkoxide groups (Bradley *et al.*, 1978). The exothermic peak at 520^{o}C in the DTA curves, present in all PT samples, which has no mass loss associated, is due to the sample crystallization as explained later.

The PT powders decompose upon heating in a similar way regardless of the hydrolysis conditions (Figure 4.2-6, Figure 4.2-7).

In order to obtain qualitative chemical information, FTIR spectra of PT dried powders and powders quenched at 460^{o}C were recorded between 2500 cm^{-1} and 550 cm^{-1} (Figure 4.2-8). In the dried powders two absorption bands between 1400 cm^{-1} and 1520 cm^{-1} were identified as symmetric and asymmetric vibrations of the acetate groups (Nakamoto, 1997). The acetate bands completely disappear by quenching the samples to 460 ^{o}C and only very weak bands between 1250 cm^{-1} and 1450 cm^{-1}, which can be assigned to the carbonate groups, are observed (Gatehouse *et al.*, 1958). The bands at 600 cm^{-1}, specific for the M-O stretches (Coffman *et. al.*, 1996) are also observed. There are no significant differences related to the hydrolysis conditions.

The IR analysis of the PT dried and quenched powders confirm that the remaining organic groups decompose below 460^{o}C as determined also by the TG/DTA/EGA analysis.

Figure 4.2–9 presents the XRD patterns of PT_d10 powder heated at 700 ^{o}C / 1h. The powder crystallizes in pure perovskite phase with tetragonal syngony.

Figure 4.2-10 presents the XRD spectra of PT2, PT5, PT15 and 11PT15 powders heated at 500 ^{o}C and 700 ^{o}C. The powders heated at 500 ^{o}C crystallize in perovskite phase with traces of pyrochlore type phase. By increasing the temperature, there is an increase in the intensity of peaks of the perovskite phase and a weak decrease in the intensity of pyrochlore peaks. There is no difference in the XRD patterns regardless the hydrolysis conditions. However, a big difference is observed in the phase purity when the powders were prepared from the sol with a low concentration (0.02 M). There are many literature reports (Merkle *et al.*, 1998; Polli *et al.*, 2000) that secondary phase appears during crystallization and special care must be taken to avoid it (Polli *et al.*, 1995). We associate the complete disappearing of the residual pyrochlore phase to the improved homogenization in the latter case. The low concentration of the reactants (0.02 M) allows a better mixing of the sol with the water/butanol mixture resulting in a more homogenous nucleation and growth of the particles.

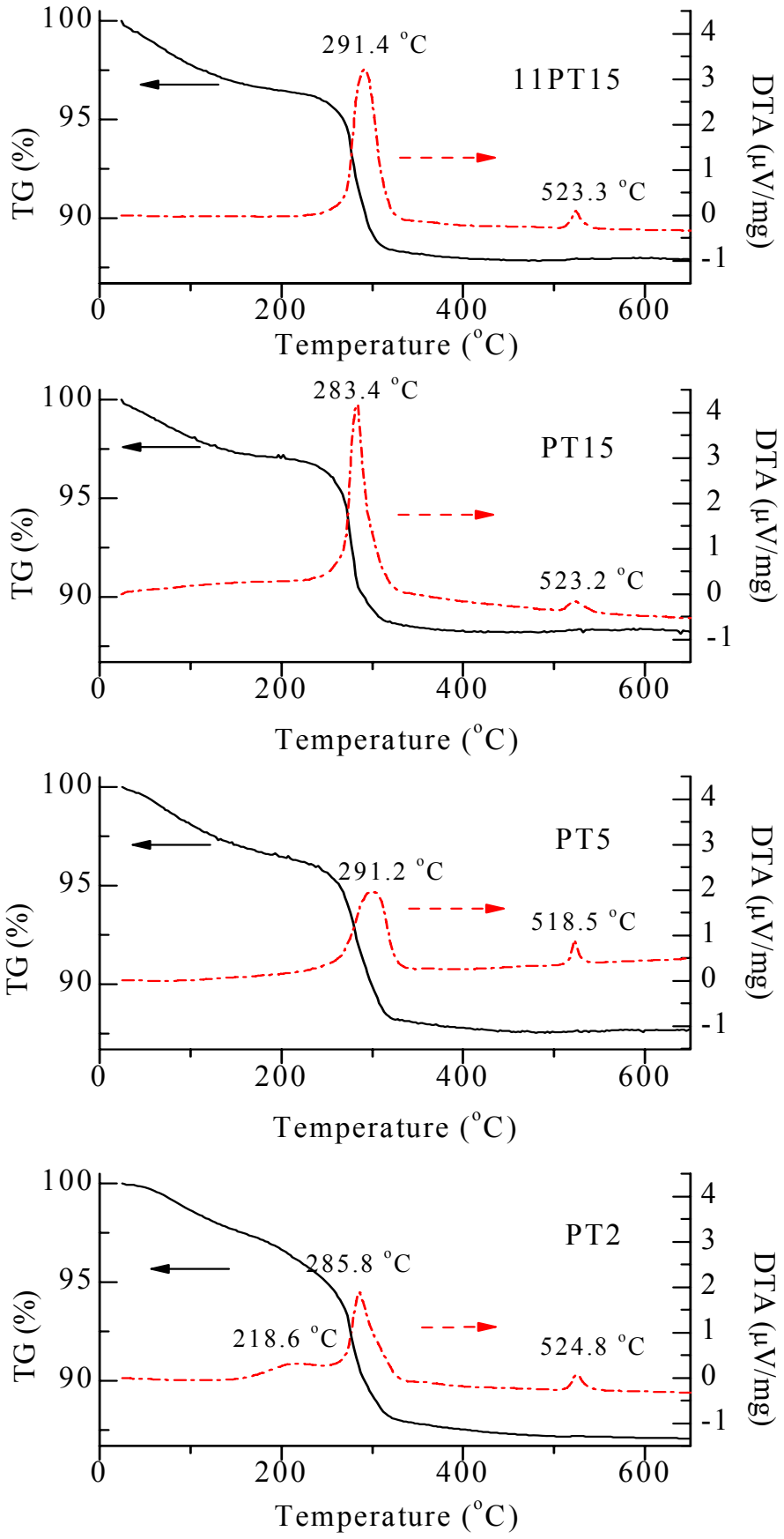

Figure 4.2-6. TG-DTA curves of PT dried powders, prepared with different hydrolysis conditions.

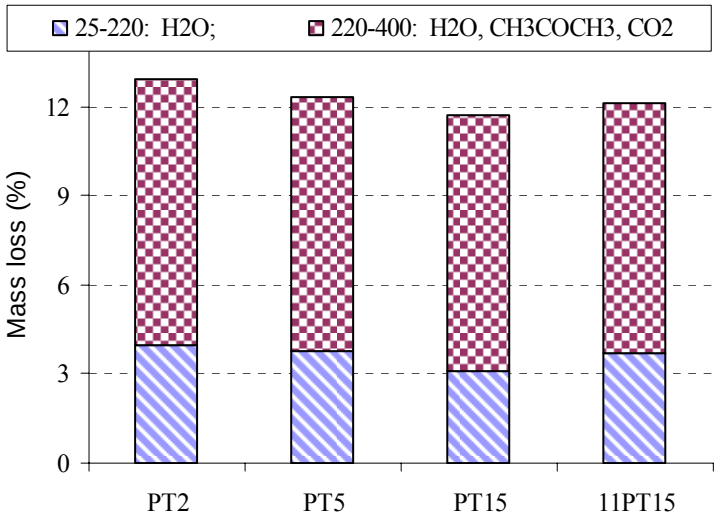

Figure 4.2-7. Mass losses and evolved gases of PT precursors determined by TG/EGA in different temperature ranges.

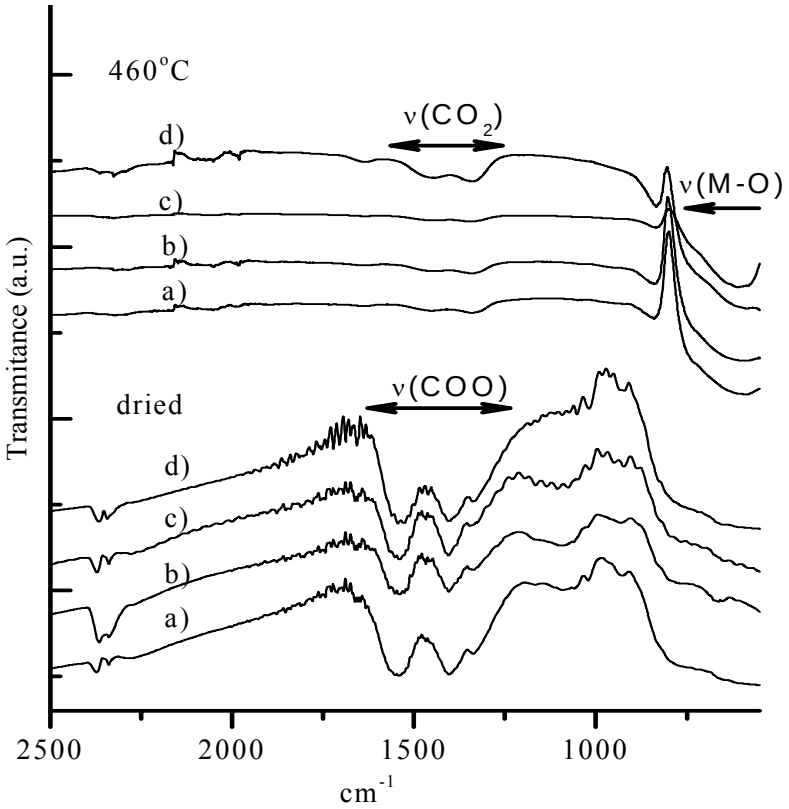

Figure 4.2-8. IR spectra of a) PT2, b) PT5, c) PT15, d) 11PT15 powders dried at 150 °C, and quenched at 460 °C.

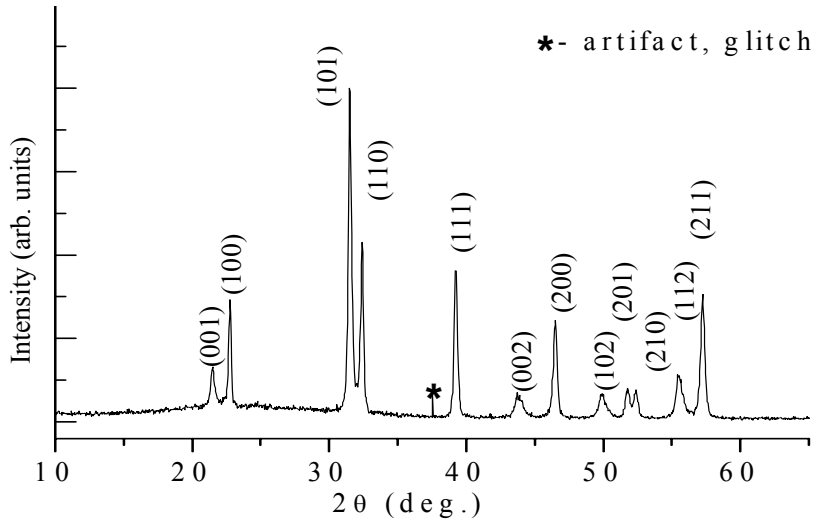

Figure 4.2-9. XRD pattern of PT_d10 heated at 700 °C / 1h. The main reflections of the perovskite phase are marked (JCPDS 78-0298).

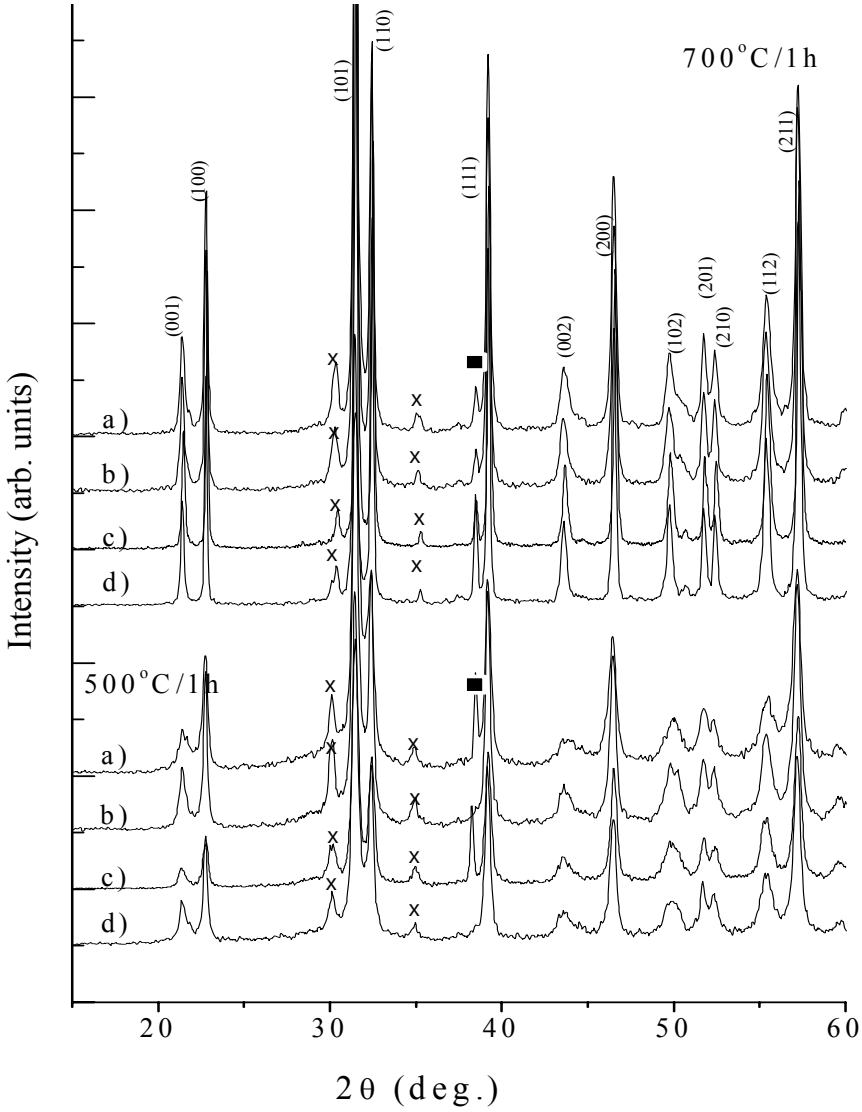

Figure 4.2-10. XRD patterns of a) PT2, b) PT5, c) PT15, d) 11PT15 powders after different heat treatments. The main reflections of the perovskite phase (JCPDS 78-0298) are marked; ■–sample holder, x–pyrochlore type phase.

Table 4.2-6 presents the SSA and the calculated d_{BET} of the PT powders heated at 700 °C/ 1h prepared from the 0.2 M and the 0.02 M sols. In both cases the hydrolysis was performed in alkaline medium with a molar ratio $Pb(OAc)_2 : H_2O : NH_3 = 1 : 15 : 5$ and dried at 150 °C and 90 °C, respectively. There is a decrease in the d_{BET} from 186 nm for the powder prepared from the 0.02 M sol, to 144 nm for that prepared from the 0.2 M sol. A similar trend, smaller particles resulting from the sol with a higher concentration, was observed also for the dried powders (Table 4.2-4).

Table 4.2-6. SSA and d_{BET} of PT powders, prepared from the 0.02 M (PT_d10) and the 0.2 M sol (11PT15) hydrolysed with a molar ratio $Pb(OAc)_2 : H_2O : NH_3 = 1 : 15 : 5$, dried at 150 °C and 90 °C, respectively and heated at 700 °C / 1h.

	PT_d10 (0.02 M)	11PT15 (0.2 M)
SSA (m^2/g)	4.03	5.24
d_{BET} (nm)	186.1	143.7

Table 4.2-7 presents the specific surface area (SSA), the calculated diameter of the particles (d_{BET}), particle diameter distributions measured by laser granulometry, the calculated agglomeration factor (F_{ag}) and polydispersity index ($(D_{90}$-$D_{10})$ / D_{50} of the PT powders heated at 500 °C / 1h and 700°C/1h, prepared with R_w=15 in neutral and alkaline medium.

Upon heating at 500 °C and 700 °C the SSA of the PT15 decreases from 16 m^2 / g to 5.5 m^2 / g, this corresponds to an increase of dBET from 46 nm to 136 nm. The median size determined by laser granulometry is in both cases about 1μm, which is further reflected in the strong decrease of agglomeration factor from 22 to 7 for the powders heated at 500 °C and 700 °C, respectively. We explain the almost triple increase of d_{BET} by intensive growth of the particles, most probably by surface diffusion. However, the almost unchanged values of D_{50} imply that interparticles sintering could take place within agglomerates and not between them. We observe a very similar behaviour for the PT powders, hydrolysed in alkaline medium, only with slightly higher d_{BET} and polydispersity indices.

Table 4.2-7. SSA, the calculated d_{BET}, particle diameter distributions measured by laser granulometry and the calculated agglomeration factor (F_{ag}) and polydispersity index ($(D_{90}$-$D_{10})$ / D_{50}) of PT15 and 11PT15 powders heated at 500 °C / 1h and 700 °C / 1h.

	Temp. (°C)	SSA (m^2/g)	d_{BET} (nm)	D_{10} (μm)	D_{50} (μm)	D_{90} (μm)	F_{ag}	$(D_{90}$-$D_{10})$ /D_{50}
PT15	500	16.09	46.2	0.71	1.03	3.02	22.2	2.24
	700	5.51	135.9	0.68	1.00	1.94	7.3	1.26
11PT15	500	13.47	55.9	0.73	1.29	4.93	23.0	3.25
	700	5.24	143.7	0.68	1.04	2.87	7.2	2.1

SEM image of PT_d10 powder, heat treated at 700 °C / 1h, is presented in Figure 4.2-11. The PT_d10 powder is composed of particles sized between 50 nm and 300 nm. Due to the high temperature of the heat treatment, the interparticle sintering occurred, agreeing well with increased d_{BET} = 186 nm (Table 4.2-7).

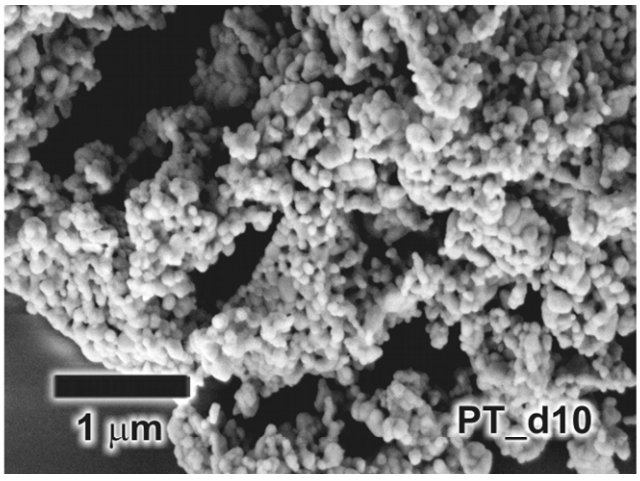

Figure 4.2-11. SEM micrograph of PT_d10 powder heated at 700 °C / 1h.

Figure 4.2-12 presents SEM micrographs of PT powders, heated at 500 °C / 1h. All PT powders comprise of similar agglomerates of less than 10 μm. The SEM pictures at a higher magnification reveal that the agglomerates are composed of very fine particles at about 50 nm, agreeing with the d_{BET} values determined for the powders hydrolysed with R_w = 15 namely, 46 nm and 56 nm for PT15 and 11PT15, respectively. There are no major differences in the powder morphology related to the hydrolysis conditions.

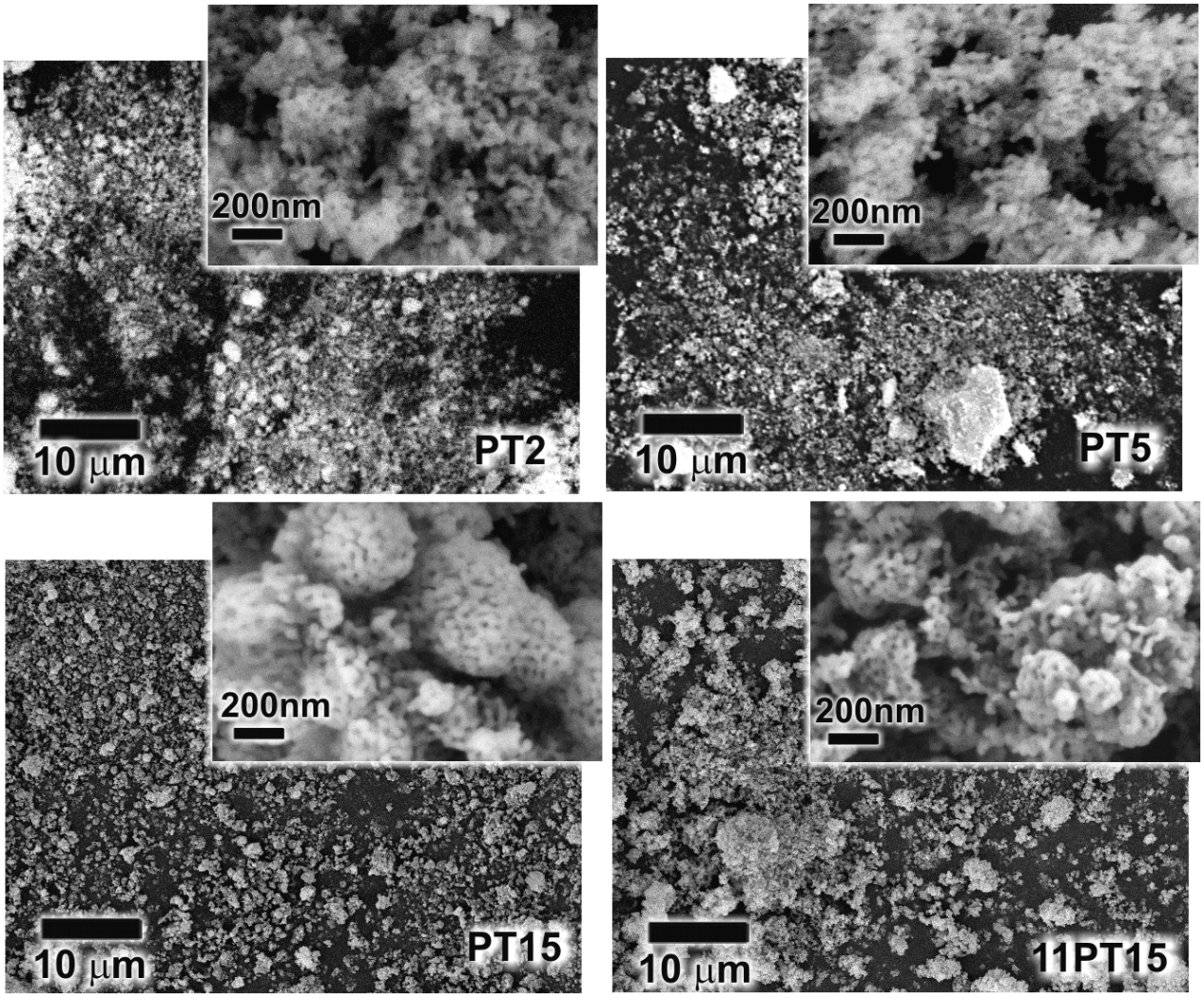

Figure 4.2-12 SEM micrographs of PT powders heated at 500 °C / 1h. Insets show the morphology of powders observed at a higher magnification.

4.2.5 Summary

The most important results on the PT synthesis are summarised in Table 4.2-8.

The calculation based on the partial charge model shows, that there is an increase in the partial charge of Ti atoms in the PT precursor as compared to Ti n-butoxide, therefore an increase in the PT precursor reactivity toward hydrolysis and condensation. The partial charges of the OH groups are negative in all cases; hence they can initiate further condensation.

The hydrolysed product (PT_d10) is composed of about 90 nm sized particles, which represent the building units of the about 500 nm particles (Table 4.2-3), as determined by PCS. The surface charge of the particles approaches zero (Table 4.2-3) and it is reasonable to conclude that they agglomerate.

The surface of the hydrolysed product is rough, with irregular cracks and the higher magnification image reveals that fragments are composed of a very porous network of a few tens of nm particles, in agreement with the d_{BET} = 20 nm (Table 4.2-4). The dried powders prepared at different hydrolysis conditions have very a similar median size of about 1.5 μm and only slightly different particle size distributions (Table 4.2-5). We can conclude that there is a small impact of hydrolysis conditions on the powder morphology.

Upon heating of dried PT hydrolysis products, the organic groups are removed in a single step. The IR analysis confirms the complete decomposition of the acetates groups in the powders quenched at 460 ^{o}C. After heating at 500 ^{o}C / 1h, the powders crystallize in perovskite phase with traces of pyrochlore phase when prepared from the sol with a 0.2 M concentration. Lowering the sol concentration to 0.02 M allows a better mixing of the sol with the water/butanol mixture, allowing a more homogeneous nucleation and growth of the particles, which results in crystallization of pure perovskite phase.

The crystalline powders are composed of agglomerates of very fine particles with a diameter of about 50 nm and 140 nm when heated at 500 ^{o}C / 1h and 700 ^{o}C / 1h, respectively. There are no major changes in the powder morphology from the precursor powder to crystalline powders beside those related to crystallization and particles growth. The morphology is mainly retained, regardless the hydrolysis conditions.

Table 4.2-8 Summary of the most important results obtained in the synthesis of PT powders.

C (M)	pH	R_w	PCS – median size (nm)	TG/DTA	XRD		d_{BET} (nm)			Morphology	
					500 °C	700 °C	Dried	500 °C	700 °C	dried	700 °C
0.2	neutral	2	-	2 steps	PE+ Py tr	PE+ Py tr	-	-	-	Agglomerated particles	Agglomerated particles
		5	-				-	-	-	Agglomerated particles	Agglomerated particles
		15	-				-	46.2	135.9	Agglomerated particles	Agglomerated particles
	alkaline	15	-				8	55.9	143	Agglomerated particles	Agglomerated particles
0.02	alkaline	15	524			Pure PE	21	-	186	Porous network of small particles	Agglomerated particles
	dilution	10x	87				-	-	-	-	-

Py tr. – traces of pyrochlore phase.

4.3 $La_2Zr_2O_7$

This chapter presents an insight into the synthesis of lanthanum zirconate powders, prepared by the nitrate-alkoxide sol-gel route. Lanthanum nitrate sol (LN_sol) was first prepared by dehydration of lanthanum nitrate in 2-methoxyethanol. The sol was then mixed with zirconium butoxide and by refluxing, the lanthanum zirconate sol (LZ_sol) yielded. In the next step the sol was dried leading to a friable amorphous powder and heated to yield a crystalline powder.

The first part describes the structural evolution from the sol to the amorphous powder. The characterization of the precursors and the sol was performed in order to understand if any reaction between lanthanum nitrate and zirconium n-butoxide occurred during the synthesis. The second part of this chapter includes the powder characterization and in the last part the sinterability of the powder is studied.

4.3.1 Structural evolution from the sol to the amorphous powder

Figure 4.3-1 presents the thermogravimetric (TG) and differential thermal analysis (DTA) curves of the $La(NO_3)_3 \cdot 5.56H_2O$, and LN_sol. The thermal behaviour of $La(NO_3)_3 \cdot 5.56H_2O$ follows the typical decomposition pathway of this compound between RT and 800°C (Wendlandt *et al.*, 1956). The total mass loss is 62.11 %, which is 0.7 % higher than the theoretical mass loss. The peak at 83 °C in the DTA curve which has no associated mass loss is due to melting. The endothermic DTA peaks between 170 °C and 250 °C associated with a mass loss of 22.56 % correspond to dehydration in several steps. The next major mass loss, 27.20 % associated with a broad endothermic peak at 440 °C is due to the conversion to lanthanum oxynitrate (Eq. 4.3-1). Between 500 °C and 650 °C the sample loses 12.23 % and the two endothermic events at 577 °C and 641 °C are typical for the decomposition of lanthanum oxynitrate, via lanthanum carbonate (Eq. 4.3-2) to lanthanum oxide (Eq. 4.3-3), as confirmed by earlier literature (Klingemberg *et al.*, 1996).

$$La(NO_3)_3 \longrightarrow LaONO_3 + 2\,NO_2 + 1/2\,O_2 \qquad \text{Eq. 4.3-1}$$

$$2\,LaONO_3 \longrightarrow La_2O_2CO_3 + NO + NO_2 + O_2 \qquad \text{Eq. 4.3-2}$$

$$La_2O_2CO_3 \longrightarrow La_2O_3 + CO_2 \qquad \text{Eq. 4.3-3}$$

The LN_sol (1M) follows a different decomposition pathway from the salt. The total mass loss between RT and 800 °C is 84.12 %. The mass loss of 65.14 % between RT and 170°C, accompanied by two endothermic DTA peaks at 105 °C and 142 °C is due to the evaporation of solvent and water. Between 170 °C and 350 °C another weight loss of 11.27% accompanied by two strong exothermic DTA peaks at 231 °C and 255 °C occurs. We associate this with a violent decomposition of the nitrate groups in the presence of organic groups of the solvent. Above 350 °C the sample decomposes gradually without major thermal events.

The TG curve of the LZ_sol (1M) presents a total mass loss of 70.90 %. The major mass loss, 39.50 %, between R.T. and 150 °C, which is associated with a strong endothermic peak at 109.9 °C in the DTA curve, is due to the evaporation of the solvent. Between 150 °C and 200 °C, another mass loss of 11.22 % occurs, which is accompanied by a sharp exothermic DTA peak at 169.9 °C. We associate this peak with the reaction between the nitrates and the organic groups present in the sample. Between 200 °C and 800 °C the sample gradually loses 20.20 %, associated with the exothermic peaks at 237.8 °C, 340.4 °C and 648.0 °C, which we connect with the decomposition of the remaining functional groups or oxidation of carbon residues.

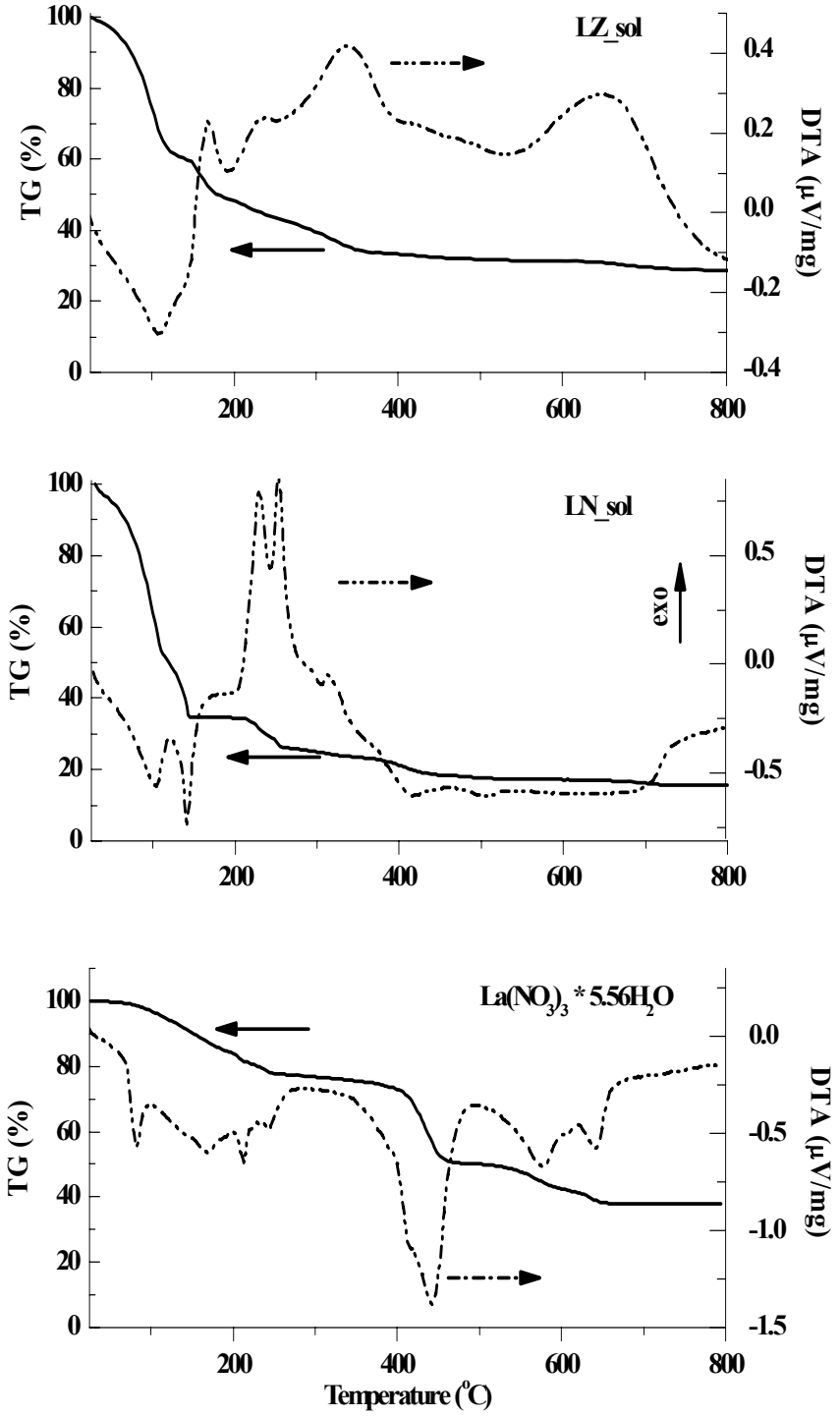

Figure 4.3-1. TG and DTA curves of the $La(NO_3)_3 \cdot 5.56\ H_2O$, LN_sol and LZ_sol.

Infrared spectroscopy was performed to understand the chemical environment of the anions at each stage of the synthesis. Figure 4.3-3 presents the spectra of 2-methoxyethanol, $La(NO_3)_3 \cdot xH_2O$, LN_sol, LZ_sol, and LZ_dried.

The spectrum of the solvent 2-methoxyethanol presents all the characteristic O-H, C-H and C-O bands in agreement with the literature (Guha *et al.*, 2003; NIST, 2005). In the spectrum of $La(NO_3)_3 \cdot xH_2O$, two different regions can be distinguished: 3600-3100 cm^{-1} corresponding to the O-H stretching vibrations and 1650-700 cm^{-1} corresponding to the nitrate vibrations (Gatehouse *et al.*, 1957). Additionally it contains also the band at 1636 cm^{-1} assigned to the bending mode of the lattice-coordinated water. The spectrum of LN_sol contains characteristic bands of both $La(NO_3)_3 \cdot xH_2O$, and the 2-methoxyethanol. The spectrum of LZ_sol is almost identical to the spectrum of LN_sol. The spectrum of the dried powder exhibits the characteristic band of O-H absorption between 3600-3000 cm^{-1}, a broad band at 1700-1200 cm^{-1} and a

sharp band at 850 cm^{-1} attributed to carbonate species (Nakamoto *et al.*, 1997). Due to the breadth of the band between 1700 and 1200 cm^{-1}, these vibrations can be assigned to bulk CO_3^{2-}, as well as to unidentate and bidentate CO_3^{2-} (Klingemberg *et. al.,* 1996). Very low intensity peaks at 812 cm^{-1} and 739cm^{-1} could be assigned to the residual nitrate species.

Thermal decomposition of LN_sol obviously proceeds differently from that of the pure salt (Figure 4.3-1).

The exothermic decomposition between 170 ^oC and 350 ^oC suggest the presence of the organic groups together with the nitrate groups. A possible explanation is that the 2-methoxyethanol molecules coordinate to the lanthanum ions, and at higher temperature nitrate ions act as oxidizing agents and enable the organic groups' removal. The presence of two exothermic peaks suggests also different types of bonding e.g. monodentate or bidentate (Kuhn *et al.*, 1964).

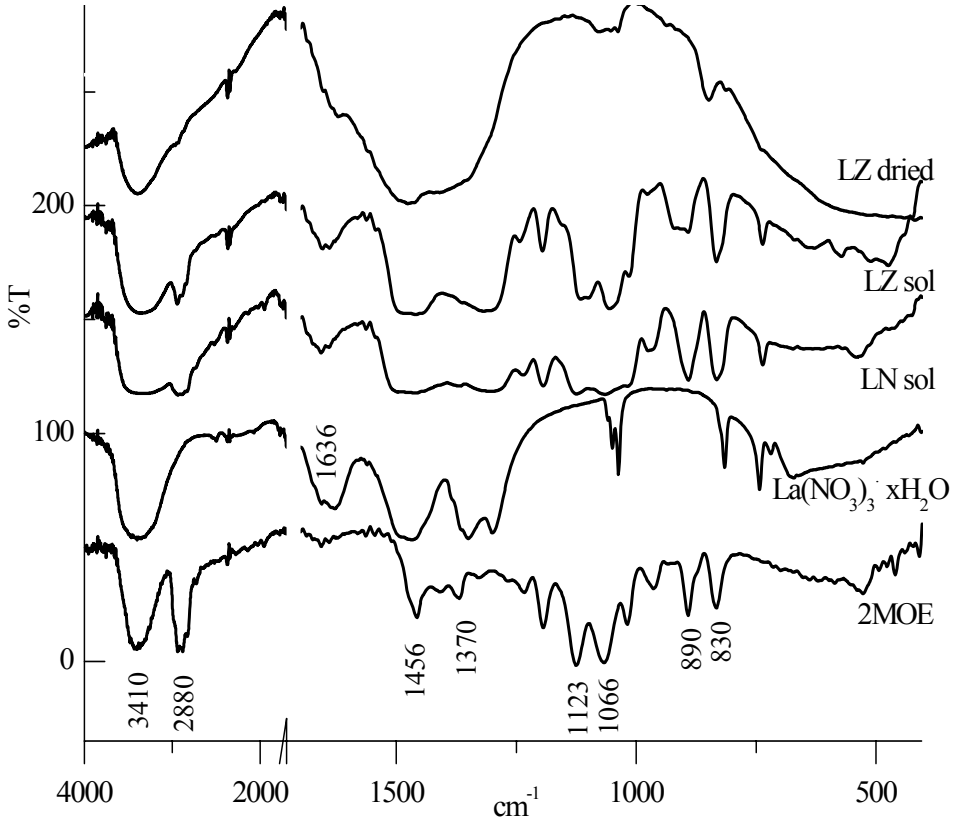

Figure 4.3-2. IR spectra of 2-methoxyethanol, $La(NO_3)_3 \cdot 5.56\ H_2O$, LN_sol, LZ_sol, LZ_dried and crystalline LZ.

Figure 4.3-3 presents EXAFS spectra of La_L_3 edge in the k and R-space. Prominent peaks in the Fourier transforms of the EXAFS spectra are the fingerprints of the photoelectron backscattering on the near neighbours around La atom. The R-space spectra are composed of one peak at about 2 Å, with a decreasing intensity from the sols to LZ_dried and LZ_500, and a second peak situated at 3.4 Å, with an even stronger decrease of intensity to noise level at LZ_500.

The local environment of La atoms can be reliably deduced in the quantitative EXAFS analysis, performed in the k interval from 2.5 to 9.9 $Å^{-1}$. The complete list of the best-fit structural parameters is collected in Table 4.3-1.The local environment of La atoms in LN_sol comprises 10 O at 2.57 Å, 2 N at 3.11 Å, 1 N at 3.45 Å, 6 O at 3.95 Å, and 7 O at 4.41 Å. Small differences are found in the local environment of LZ_sol: 9 O at 2.57 Å, 2 N at 3.11 Å, 1 N at 3.51 Å, 7 O at 3.95 Å and 6 O at 4.40 Å.

The large number of oxygen atoms at 3.95 Å and 4.40 Å could be attributed also to the presence of some carbon atoms since the procedure cannot distinguish between light elements with small difference in their atomic number, such as oxygen and carbon.

A qualitative analysis of the R-space of LZ_dried shows that the intensity of the peak at about 3.8 Å is decreased, close to the noise level, in comparison to the corresponding peak of LN_sol and LZ_sol. The spectrum of LZ_dried could not be described by the model developed for the LN_sol and LZ_sol. A heavy element was required in the model to describe the peak at 3.8 Å. We tried the fit with either La or Zr and

the results were acceptable for both. Due to the short k-range used in analysis the fit cannot distinguish between them since the maximum amplitude of their scattering contribution is beyond the investigated range.

The results of the model containing La as a heavy element are presented and the motivation for the choice is given in the discussion section. The analysis reveals that the first peak is composed of ~ 7 O distributed at 2.45 Å and 2.59 Å, followed by ~ 2 light atoms such as N or C at 3.21 Å and 3.49 Å. Next there is one La atom at 4.17 Å and ~ 4 O at 4.49 Å.

Since in the spectrum of LZ_500 the second peak is completely vanished only the first peak is modelled and the result of the fit shows that the local environment of La is described by 5 O at 2.48 Å.
Figure 4.3-4 presents EXAFS spectra of Zr-K edge in k-space and R- space. The spectra in the R - space are composed of two similar peaks for all samples.

The quantitative EXAFS analysis is performed in the k interval from 4 to 11.4 Å and the best fit parameters of the nearest coordination shells around Zr atoms are collected in Table 4.3-2. The local environment of Zr atoms in the LZ_sol is described by ~ 7 O atoms at 2.12 Å, two C at 2.73 Å and ~ 6 Zr atoms at 3.42 Å. The local environment of Zr in the LZ_dried is similar: ~ 7 O at 2.12 Å, 2 C atoms at 2.71 Å and ~ 6 Zr at 3.40 Å. The analysis of the LZ_500 reveals that the Zr neighbourhood is composed of ~ 6 O at 2.09 Å, ~ 2 C at 2.71 Å and ~ 6 Zr at 3.37 Å. which is slightly shorter than Zr-Zr distance in the LZ_sol and LZ-dried. No Zr-La correlation was found in any of the investigated samples.

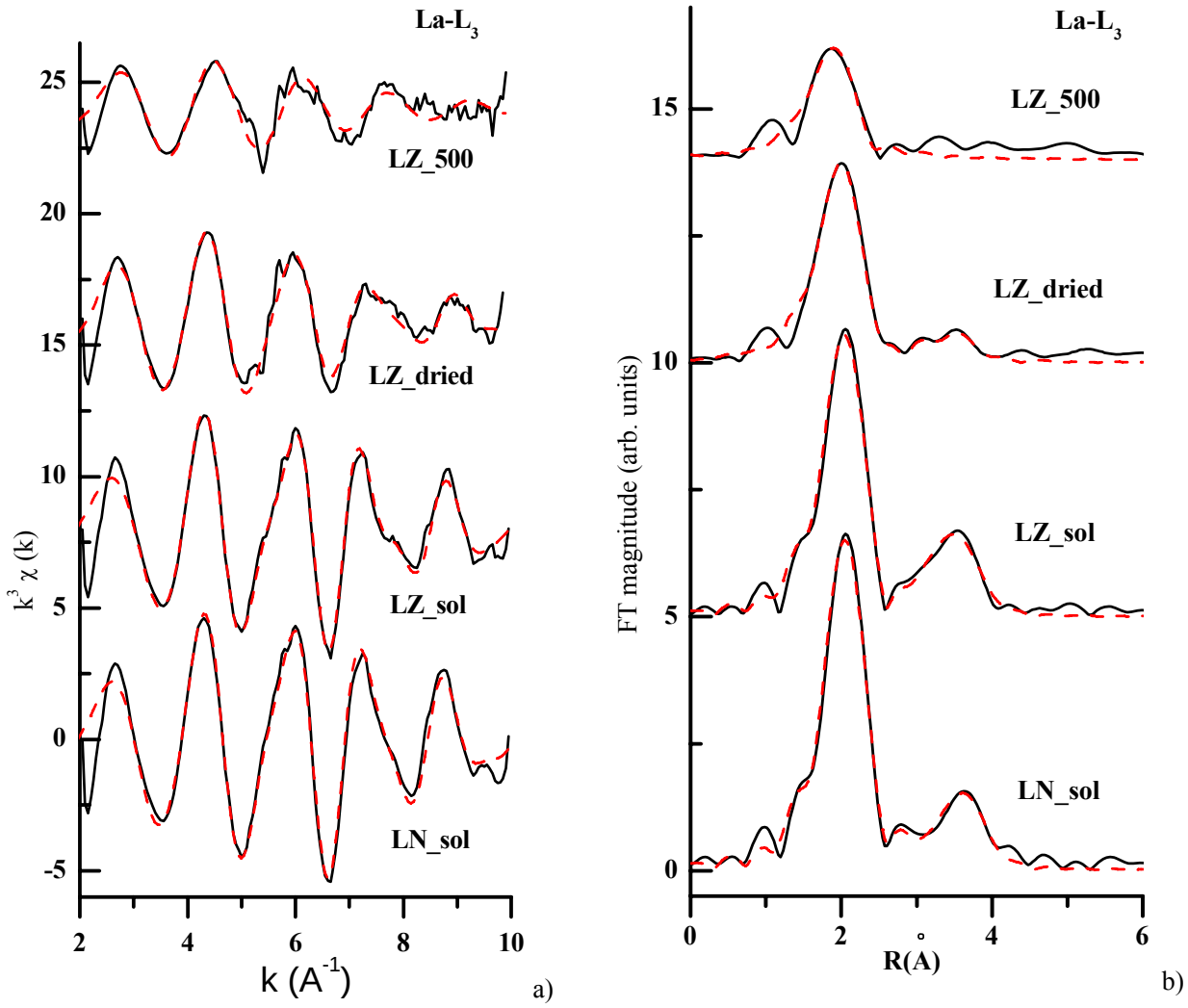

Figure 4.3-3. k^3 weighted La-L_3 data (a) and their k^3 weighted Fourier transforms (b) of LN_sol, LZ_sol, LZ_dried and LZ_500. Solid line – experiment, dashed line - - - EXAFS model.

Table 4.3-1. Parameters of nearest coordination shells around lanthanum atoms in LN_sol, LZ_sol, LZ_dried and LZ_500. Type of neighbour atom, their average number *N,* distances R and Debye Waller factors σ^2 are listed. Uncertainty is given as the absolute value or, when in parenthesis, in units of the last digit. For parameters that are kept fixed in the fit, the error brackets are omitted. The quality of the fit is indicated by R-factor (Ravel *et al.*, 2005).

Sample	Scattering atom	N	R(A)	σ^2	R-factor
	O	9.6(7)	2.577(2)	0.009	
LN sol	N	1.9(2)	3.11(1)		
	N	1.1(3)	3.45(3)	0.002	0.004
	O	5.8±1.0	3.95(1)	0.008	
	O	7.1±1.5	4.41(1)	0.008	
	O	9.3(7)	2.575(2)	0.009	
LZ sol	N	1.9(2)	3.11(1)		0.004
	N	1.1(3)	3.51(4)	0.005	
	O	7.3(8)	3.94(1)	0.007	
	O	6.0±1.3	4.40(1)	0.008	
	O	2.6(9)	2.45(2)	0.005	
	O	4.2(8)	2.59(4)	0.006	
	N, C	1.3(8)	3.21(4)		
LZ_dried	N, C	1.4±1.0	3.49(3)	0.003	0.011
	La	1.0(5)	4.17(3)	0.005	
	O	3.7±2.4	4.49(6)	0.008	
LZ_500	O	5.4(4)	2.48(1)	0.015	0.008

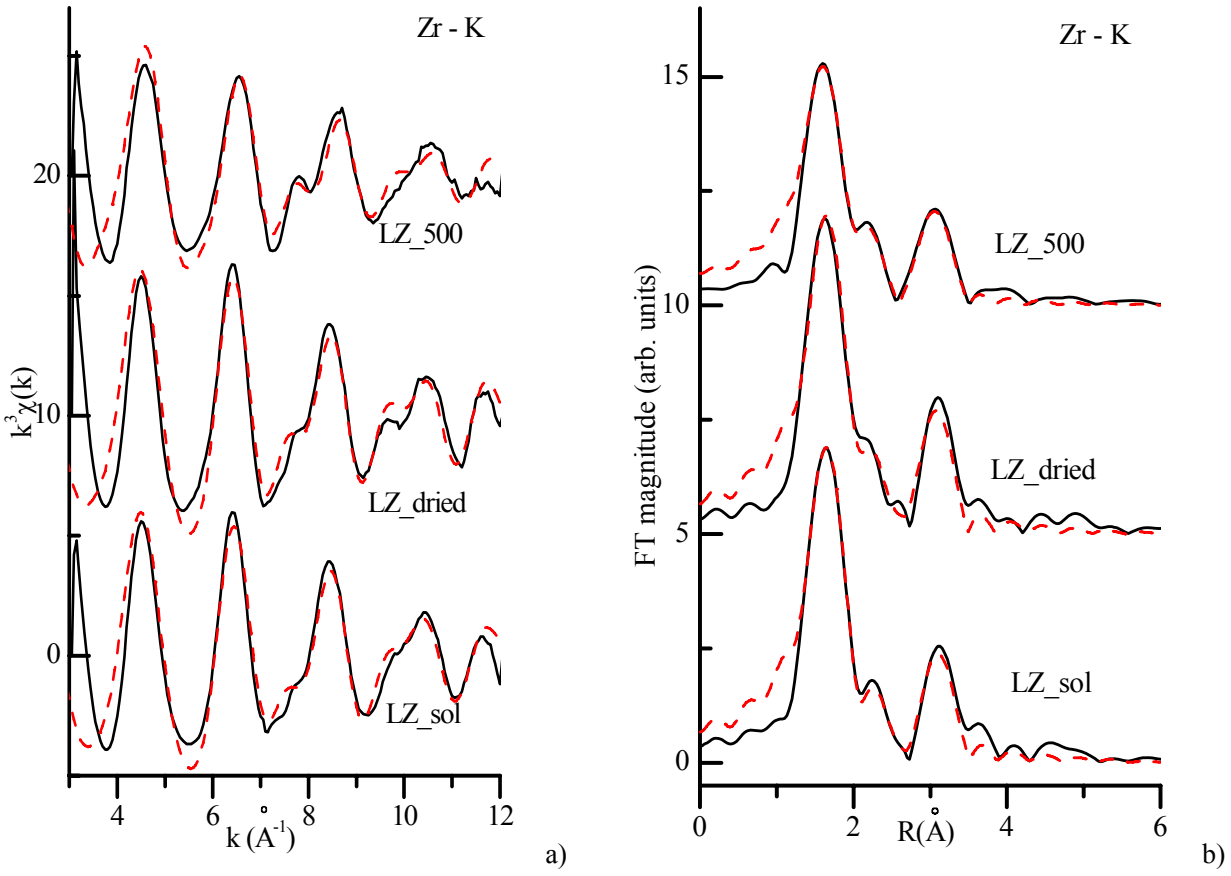

Figure 4.3-4. k^3 weighted Zr-K data (a) and their k^3 weighted Fourier transforms (b) of LZ sol, LZ dried powder and LZ powder heated at 500 °C / 1h. Solid line – experiment, dashed line - - - EXAFS model.

Table 4.3-2 Parameters of nearest coordination shells around zirconium atoms in LZ_sol, LZ_dried and LZ_500. Type of neighbour atom, their average number *N,* distances R and Debye Waller factors σ^2 are listed. Uncertainty is given as the absolute value or, when in parenthesis, in units of the last digit. For parameters that are kept fixed in the fit, the error brackets are omitted. The quality of the fit is indicated by R-factor (Ravel *et al.*, 2005).

Sample	Scattering atom	N	R(A)	σ^2	R-factor
LZ_sol	O	6.5(5)	2.12(1)	0.007	0.012
	C	1.7±1.2	2.73(5)	0.006	
	Zr	5.6±1.3	3.42(2)	0.014	
LZ_dried	O	7.0(6)	2.12(1)	0.008	0.015
	C	2.2±1.2	2.71(4)	0.004	
	Zr	5.8±1.4	3.40(2)	0.014	
LZ_500	O	6.3(6)	2.09(1)	0.010	0.012
	C	1.8±1.0	2.71(4)	0.004	
	Zr	5.5±1.2	3.37(3)	0.015	

The lanthanum environment in LN_sol, determined by EXAFS analysis, comprises first of about 10 O, 2 N at a shorter distance and 1 N at a larger distance and a large number of O atoms at a distance between 4 – 4.5 Å (Table 4.3-1). The distribution of the 10 O atoms and the 3 N atoms is consistent with a structure similar to those found in the early stages of $La(NO_3)_3 \cdot x\ H_2O$ decomposition (Gobichon *et al.*, 1996). The large number of more distant O could be explained by the presence of the C atoms which cannot be distinguished from O atoms in EXAFS analysis derived from the 2-methoxyethoxide groups coordinated to the La ions.

The IR analysis shows that the LN_sol spectrum contains characteristic bands of both $La(NO_3)_3 \cdot x\ H_2O$ and 2-methoxyethanol. The similarity of La environment in the LN_sol with the crystalline $La(NO_3)_3 \cdot 4\ H_2O$ points to the fact that $La(NO_3)_3 \cdot x\ H_2O$ was only partially dehydrated by dissolution and further distillation in 2-methoxyethanol, and nitrate ions remained strongly coordinated to the La ions. In the next step we synthesised the LZ_sol by the reaction of LN sol with the zirconium n-butoxide.
The IR analysis shows that the chemical environment of anions is very similar in the LN_sol and LZ_sol. The lanthanum environments in LN_sol and LZ_sol are very similar and not changed by Zr butoxide addition.

EXAFS analysis of LZ_sol reveals that the Zr environment is populated by ~ 7 O in the first shell and ~ 6 Zr atoms in the next shell. The high number of Zr around a central Zr atom is similar to the environment of Zr in polynuclear oxo-alkoxide complexes, often found in Zr alkoxide-based systems (Turova *et al.*, 2002; Malic *et al.*, 2006; Ion *et al.*, 2008). Even if residual lattice-coordinated water is still present (Gobichon *et al.*, 1996) we believe that it is not available to hydrolyse the alkoxide groups, since the thermal analysis shows that dehydration of LN_sol takes place at 140 ^oC, which is 17 ^oC higher that the reflux temperature (123 ^oC). In this case, the Zr polynuclear oxo-alkoxide species form by thermolysis during reflux. No La-La or La-Zr correlations were found therefore it is very probable that the LZ_sol is a pure mixture of LN_sol and zirconium n-butoxide.

4.3.2 Thermal decomposition, crystallization and morphology of LZ powder

The sol (0.1 M) was dried by heating at 150 ^oC. The photos recording the evolution of the powder are presented in Figure 4.3-5. After evaporation of the solvent, the sample started to swell (at the reference time 0), to foam and expanded its volume for more than 100 times, then it self-ignited and for a few seconds it burnt, yielding a grey spongy structure.

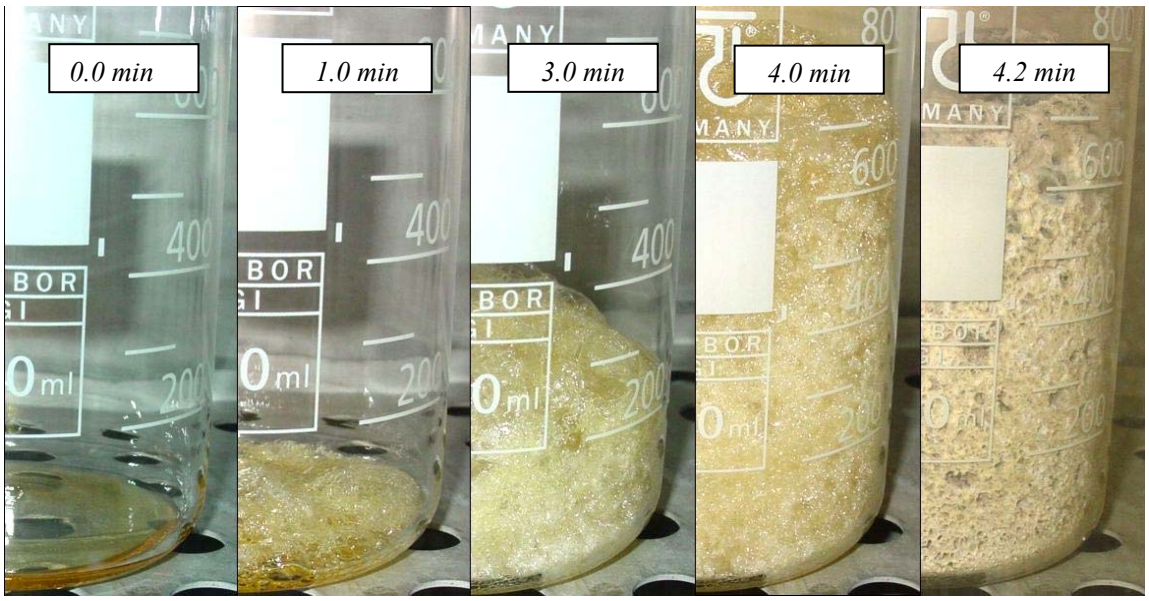

Figure 4.3-5. Sequence of the sol to powder evolution in time during drying at 150 °C; the time of each stage is specified.

The reaction between the alkoxides and the nitrates has not been studied, to the best of our knowledge. In our case the decomposition of the LZ sample starts with an exothermic reaction between the nitrates and the alkoxide groups, similar to the case of nitrates-citrates (Baythoun *et al.*, 1982; Schafer *et al.*, 1997) and nitrates-EDTA (Wang *et al.*, 1992; Wang *et al.*, 1994), where nitrates act as oxidizing agents for the organic groups and enable their removal.

The thermal behaviour of the powder dried at 150 °C for 12 h is presented in Figure 4.3-6. The TG curve shows a gradual decomposition, with a total mass loss of only 11.14 %. The first major mass loss accompanied by a small exothermic peak appears above 200 °C. This means that the residual functional groups are unable to initiate another exothermic reaction, and so they just decompose during the subsequent steps. Above 1000 °C no other mass loss or thermal event is observed.

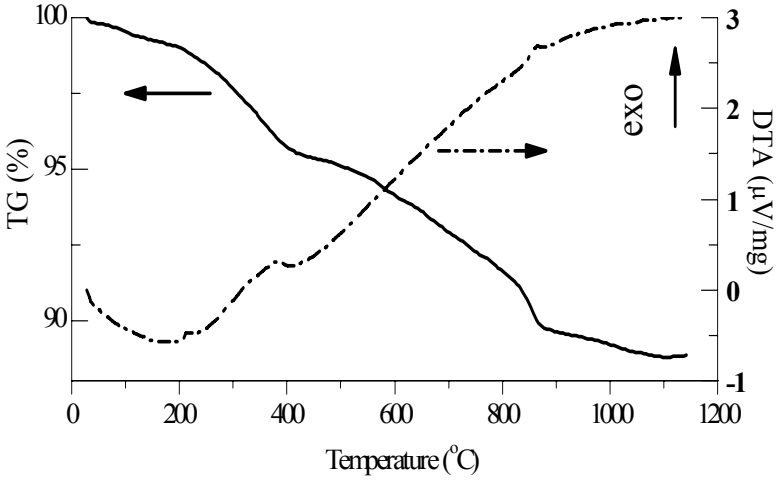

Figure 4.3-6. TG/DTA curves of LZ powder dried at 150 °C / 12h.

Figure 4.3-7 shows the XRD patterns of the dried powder and of the powder heat treated at 500 °C / 1h, 700 °C / 1h, 800 °C / 1h and 900 °C / 1h The spectra of the dried powder and of the powders heated at 500 °C / 1h and 700 °C / 1h consist of a broad peak around 30 ° confirming the amorphous nature of the powder. After heating at 800 °C / 1h the powder is completely crystallized into the $La_2Zr_2O_7$ phase (JCPDS 73-0444). The crystallite size calculated from the XRD peak-broadening for the powder heat treated at 900 °C for 1 h is 67 nm.

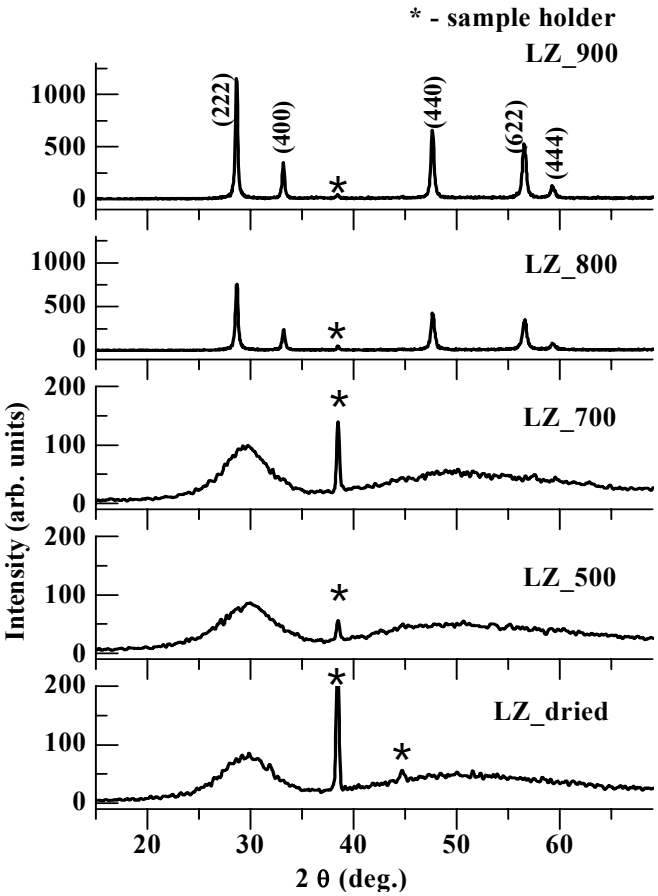

Figure 4.3-7. XRD patterns of LZ dried, LZ_500, LZ_700, LZ_800, and LZ_900.

The morphology of the dried powder and the powder heated at 900 ^{o}C / 1h is presented in Figure 4.3-8. The dried powder is composed of very porous fragments. By heating, the porous nature of the fragments is retained and distinguishable particles of about 70 nm size are observed in agreement with the crystallite size determined from XRD data.

Table 4.3-3 presents the specific surface area (SSA) and the calculated d_{BET} of the LZ powders after drying and heating at 900 ^{o}C / 1h. The d_{BET} of the dried powder is 105 nm, while the d_{BET} of the powder heated at 900 ^{o}C / 1h is 71 nm. We attribute the decrease of particle size to shrinkage/densification, in agreement with the SEM images and the crystallite size calculation.

Similar flake-like morphologies are usually found when the powders are prepared using a low-temperature combustion synthesis (LCS) (Luo *et al.*, 2003) or sol-gel combustion (Schafer *et al.*, 1997). In this case, the precursors are nitrates and a fuel is citric acid. Sometimes an oxidizing additive (NH_4NO_3) is required for the combustion. During the decomposition of the organic compounds, gases are released and these promote the formation of pores. When an oxidizing additive is used, the obtained powders are already crystalline without the need for any further heat treatment.

We propose that in our case the nitrate acts as the oxidizer for the decomposition of the alkoxide groups. However, as the reactants in our case are not in the proper ratio for the combustion synthesis, the as-dried powder, even if exhibiting a porous structure which is related to a violent decomposition of organics and the evolution of gaseous products, is amorphous, and only after heating at 800^{o}C the powder is well crystallized. The XRD spectra confirm that there is no segregation of phases and that lanthanum zirconate crystallizes as a pyrochlore phase.

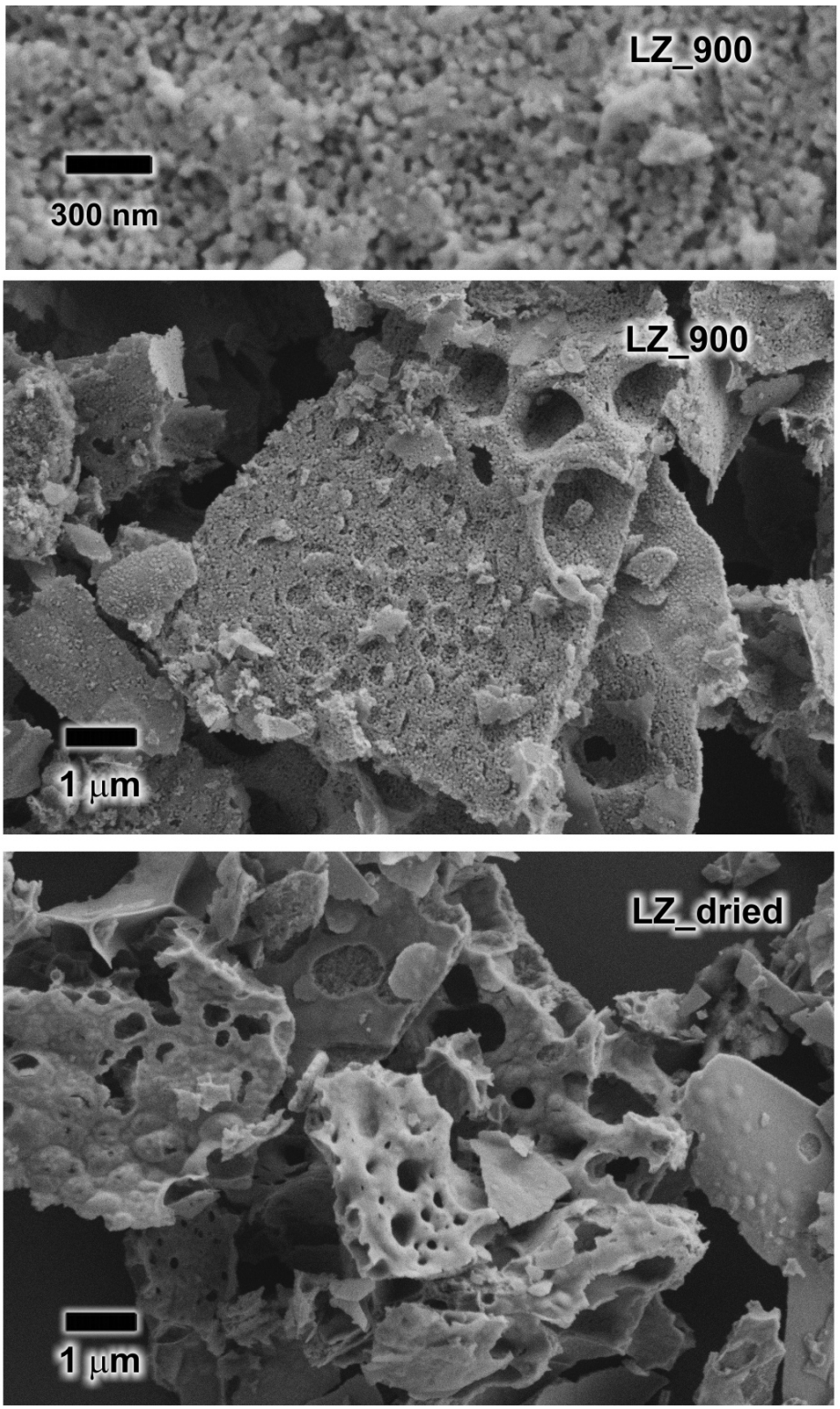

Figure 4.3-8. SEM images of the LZ-dried and LZ_900 powder heat treated at 900 ^{o}C for 1 h (top SEM image at high magnification).

Table 4.3-3. SSA and the calculated d_{BET} of LZ powders dried and heated at 900 ^{o}C / 1h.

	SSA (m^2/g)	d_{BET} (nm)
LZ_dried	19.0	105
LZ_900	14.0	71

4.3.3 Sinterability of $La_2Zr_2O_7$ powder

The sintering curve of the LZ pellet, prepared from the powder heated at 900 °C / 1h, and pressed at 100 MPa, expressed as the relative density versus temperature, is shown in Figure 4.3-9. The theoretical density (D_X) of lanthanum zirconate is 6.021 g / cm^3 (JCPDS 73-0444). Note that the relative density of the green pellet is very low, about 35 %, which we explain by taking into account the porous structure of the powder. The sintering curve shows that the densification of the compact starts at 1200°C and proceeds rapidly. At the maximum temperature of 1400 °C there is already an increase in density of about 10 %. The LZ powder compacts were pressed at 100 MPa and 500 MPa (CIP) and sintered at 1400 °C for 2 h.

The densities of the samples measured as a function of the compaction pressure are presented in Table 4.3-4. Increasing the compaction pressure leads to an increase in the sintered density: the 100 MPa-compact reaches 77.2 % and the 500 MPa-compact 87.5 % relative density, which means that the fragments present in the powder can be broken by the application of the compaction pressure.

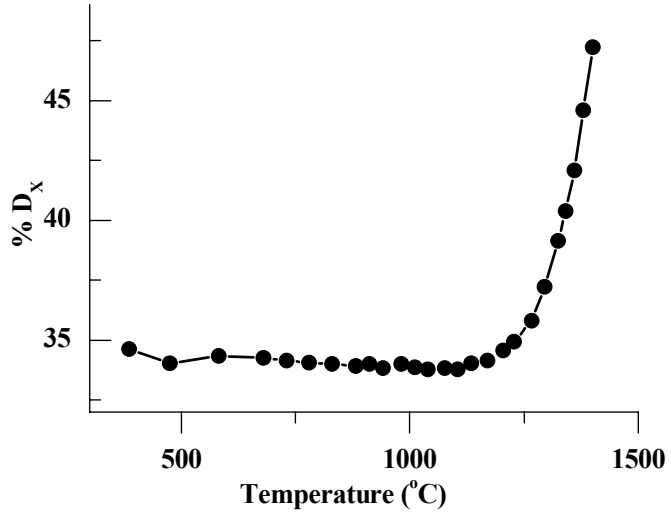

Figure 4.3-9. Sintering curve of the pellet prepared from the LZ powder, heat treated at 900 °C for 1 h and pressed at 100 MPa.

Table 4.3-4. Density (ρ) and relative density (ρ_r) of the pellets prepared from the unmilled LZ powder, sintered at 1400 °C for 2 h, as a function of the compaction pressure.

Pressure (MPa)	ρ (g / cm^3)	ρ_r (%)
100	4.64	77.2
500 CIP	5.26	87.5

SEM micrographs of LZ powders after heating at 900°C for 1 h (LZ_900) and additional milling (LZ_900_m) are presented in Figure 4.3-10. The figure also includes the microstructures of corresponding ceramics, sintered at 1400 °C.

The fragment-like morphology of the unmilled powder LZ_900 (refer to part 4.3.3) is reflected in the microstructure of the ceramics sintered at 1400 °C for 2 h which shows a relatively dense surface with a non-uniform porosity distribution.

The morphpology of the LZ powder, milled for 30 minutes, is uniform, with fragments in the micron size range. The large decrease in the size of the fragments to below 5 μm, achieved with only a short milling time, indicates that the original fragments are easily disintegrated.

The milled powder was pressed into pellets at 100 MPa and 500 MPa (CIP), which were sintered at 1400 °C for 2 h and 10 h. The densities of the pellets are shown in Table 4.3-5. We observe an increase in the relative density of the powder compacts pressed at 100 MPa and at 500 MPa (CIP) of around 20%, from 31.4 % to 49.1 %. The sintered density of the samples pressed at 100 MPa is about 85 % TD, while increasing the compaction pressure and the sintering time leads to an increase in density to 93% TD for 2 h

and to 97.9 % TD for 10 h at 1400 ^{o}C, as determined by hexane pycnometry in the latter case.

The microstructure of the pellet with the highest density (LZ_900_m_1400/10h) is presented in Figure 4.3-10. The uniform morphology of the powder is reflected in the uniform distribution of the pores observed in the microstructure.

Sintering at 1400 ^{o}C, well below the melting point of lanthanum zirconate (2280 ^{o}C from Phase Diagrams Fig. 05232), yields lanthanum zirconate ceramics with 97.9 % of theoretical density. The usually reported temperatures for pressureless sintering are around 1600 ^{o}C. (Labrincha *et al*, 1993) prepared $La_2Zr_2O_7$ by solid-state reaction, and the pellets sintered in air at 1600 –1650 ^{o}C have relative densities between 70 % and 92 %, and Zhou *et al.* (Zhou *et al.*, 2007) report 94.8 % density after sintering at 1600 ^{o}C. $La_2Zr_2O_7$ ceramics with 99.5 % relative density were obtained only by hot isostatic pressing for 2 h at 1500 ^{o}C and 196 MPa (Matsumura *et al.*, 1997).

The enhanced densification which we achieved in the present work, using neither a hot-pressing technique nor sintering close to the melting point, is attributed to the fine particle size of the powder prepared by a nitrate-modified alkoxide-based sol-gel route.

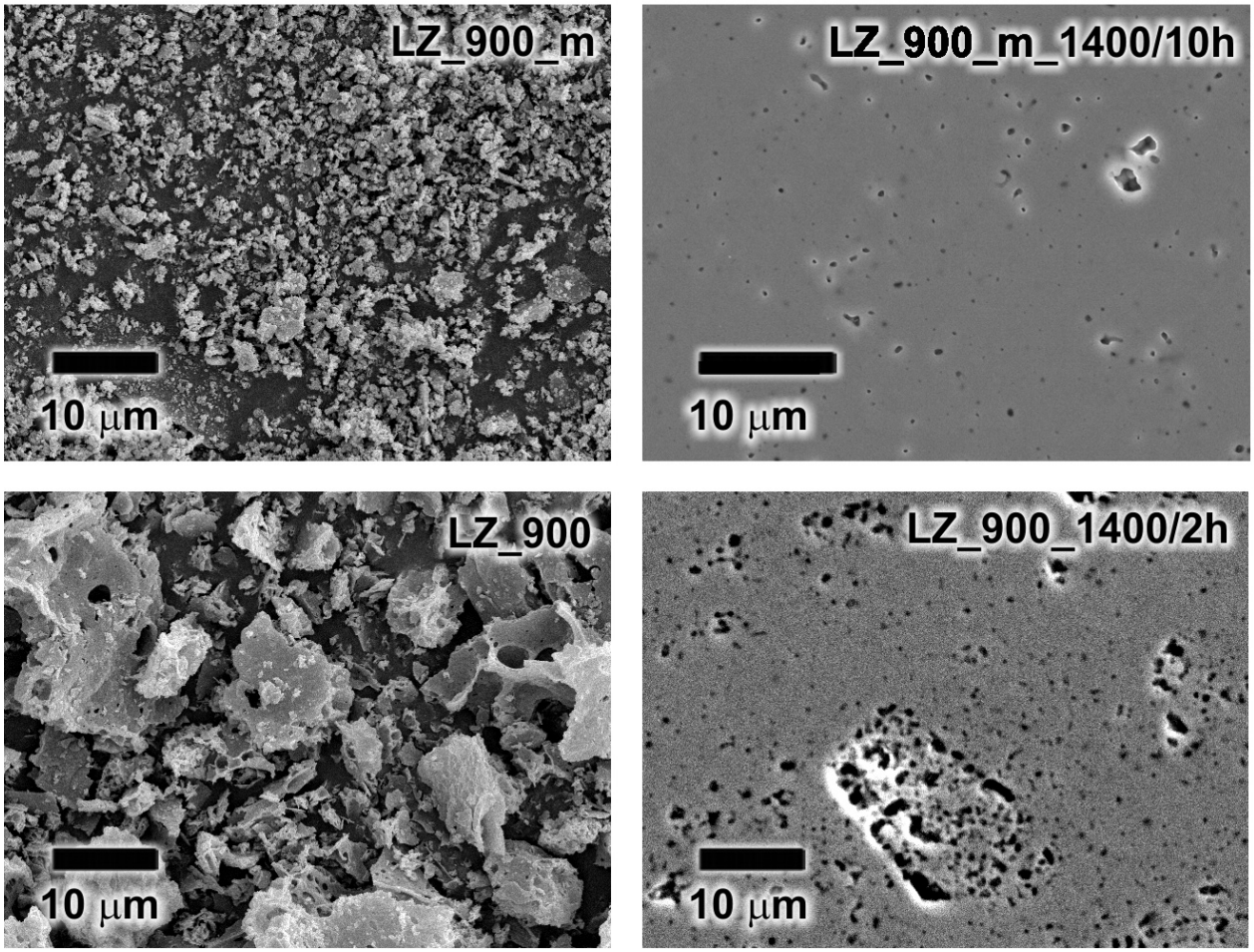

Figure 4.3-10. SEM micrograph of LZ powder, heat treated at 900 ^{o}C for 1 h (LZ_900) and milled (LZ_900_m) and their corresponding pellets, pressed at 500 MPa (CIP) and sintered at 1400 ^{o}C for 2 h (LZ_900_1400/2h) and at 1400 ^{o}C for 10 h (LZ_900_m_1400/10h), respectively.

Table 4.3-5. The density (ρ) and the relative density (ρ_r) of the pellets prepared from the milled powder, as a function of the compaction pressure and the sintering conditions.

Pressure (MPa)	Temperature (^oC)	Time (hours)	ρ (g/cm^3)	ρ_r (%)
100	-	-	1.89	31.4
500 CIP	-	-	2.95	49.1
100	1400	2	5.07	84.2
100	1400	10	5.23	85.5
500 CIP	1400	2	5.61	93.1
500 CIP	1400	10	[#] 5.90	[#] 97.9

[#] -determined by n-hexane pycnometry

4.3.4 Summary

We have demonstrated a nitrate-modified alkoxide-based sol-gel route for preparing single phase $La_2Zr_2O_7$ nanoparticles. The sol was prepared from a dehydrated lanthanum nitrate and zirconium n-butoxide in 2-methoxyethanol. The summary of the most important results is collected in Table 4.3-6.

The analysis of the precursors and their reaction products in the lanthanum zirconate synthesis, prepared by a nitrate modified alkoxide-based sol-gel route was performed by TG/DTA, EXAFS, FTIR, XRD and SEM analyses. The lanthanum nitrate sol in 2-methoxyehanol and the lanthanum nitrate salt follow different decomposition pathways. We explain this by a possible coordination of 2-methoxyethanol to the lanthanum atoms in the sol. The IR analysis shows that lanthanum nitrate remains strongly associated in the solvent. The lanthanum environment of the lanthanum nitrate sol points to a similar structure as that of the salt.

The decomposition of the LZ_sol starts with a strongly exothermic reaction between the nitrates and the organic groups. The nitrates act as an oxidizing agent for the organic groups of the precursor and enable their removal.

The IR analysis of the dried powders shows the presence of carbonate species which we attribute to $La_2O_2CO_3$, an intermediary compound in the decomposition of $La(NO_3)_3$ (Gobichon *et al.*, 1997). According to the XRD analysis, the dried powder is amorphous. During exothermic decomposition of nitrates and organic groups, the temperature can increase locally to higher values than the drying temperature, promoting local formation of carbonate species.

EXAFS analysis of La-L_3 edge spectra of LZ_dried shows that the La environment is populated by about 7 O atoms; next there are about 2 light atoms such as N or C, and at further distance 1 La and about 4 O atoms (Table 4.3-1). The presence of nitrogen atoms could be explained by the presence of some residual nitrate groups and carbon atoms are also possible due to the presence of the carbonate species confirmed by IR analysis. We decided to introduce lanthanum in the EXAFS model and to exclude Zr as the heavy element, due to the possible presence as traces of $La_2O_2CO_3$. EXAFS analysis of La –L_3 spectra of LZ_500 shows mainly a single peak composed of O atoms. It is obvious that the carbonate species formed during drying in the exothermic decomposition are unstable and by further heating they decompose. The analysis of Zr –K spectra shows very similar environments of Zr atoms in LZ_sol, LZ_dried and LZ_500. During drying at 150^{o}C the dehydration of $La(NO_3)_3$ takes place and the resulting water could hydrolyse the alkoxide groups. However, the Zr polynuclear oxo-alkoxide species, once formed during the sol synthesis, are little affected by the hydrolysis and the Zr-O-Zr links are stable in the investigated temperature range. No link between La and Zr species was established in the early stages of the synthesis.

The reaction between metallic species proceeds as a solid-state reaction when long range diffusion becomes available. The powder crystallizes after heating at 800 ^{o}C / 1h in pure pyrochlore phase. The powder heat treated at 900 ^{o}C for 1 h is composed of friable agglomerates of about 60-nm-sized nanoparticles. The ceramics obtained from the powder milled in acetone for 30 minutes has 97.9 % of the theoretical density after firing at 1400 ^{o}C for 10 h under atmospheric pressure, which is well below the usually reported temperatures for atmospheric sintering of this material.

Table 4.3-6. Summary of the most important results obtained in the synthesis and sintering of LZ powders.

	TG/DTA	IR	EXAFS		XRD	Morphology	Sintering
			La	Zr			
$La(NO_3)_3 \cdot 5.6H_2O$	Typical endothermic decomposition	$\nu(OH)$, $\nu(NO_3^-)$			-	-	-
LN_sol	Totally different from the salt, exothermic decomposition	ν(La nitrate) + ν(2MOE)	3x La-O-N	-	-	-	-
LZ_sol	Exothermic decomposition	ν(La nitrate) + ν(2MOE)	3x La-O-N	6xZr-O-Zr	-	-	-
LZ_dried	Gradual decomposition without major thermal events	$\nu(OH) + \nu(CO_3^{2-})$ + traces of $\nu(NO_3^-)$	3xLa-O-(N,C) + 1xLa-O-La	6xZr-O-Zr	-	Porous structure	-
LZ_500	-	-	5xLa-O	6xZr-O-Zr	Am	-	-
LZ_800	-	-	-	-	Pure Py	-	-
LZ_900	-	-	-	-	Pure Py	Friable agglomerates	ρ_r = 97.9 %

2MOE – 2-methoxyethanol

5 Conclusions

5.1 The impact of the B-site cation on homogeneity, decomposition pathway and morphology of $PbZrO_3$ and $PbTiO_3$ powders

Some of the inherent differences of Zr and Ti are presented in Table 5.1-1. The difference in the atomic numbers is reflected in different covalent radii, 9.84 % larger for Zr than Ti. The ionic radii are between 10 % and 30 % larger for Zr than for Ti, depending on respective coordination numbers. Zirconium n-butoxide and titanium n-butoxide form dimers and trimers, respectively, when dissolved in the parent alcohol. Ti has an about 2 % larger electronegativity than Zr which consequently induces a 4 % larger partial charge for Zr than for Ti in respective n-butoxides.

Table 5.1-1. Inherent differences between Zr and Ti.

	Zr	Ti	Reference
Atomic number	40	22	
Covalent radius (Å)	1.45	1.32	"Properties of Solids" in
Ionic radii (Å) for the most common coordination numbers (CN) of the 4+ oxidation state			*CRC Handbook of Chemistry and Physics,*
CN=4	0.59	0.42	88th Edition (Internet
CN=6	0.72	0.61	Version 2008)
CN=8	0.84	0.74	
Oligomerization of $M(OC_4H_9)_4$ in C_4H_9OH	Dimer*	Trimer#	*Peter *et al.*, 1994 #Babonneau *et al.*, 1988
Electronegativity	1.29	1.32	Livage, 1998
Partial charge of M in $M(OC_4H_9)_4$	0.6322	0.6064	Present work

Both $PbZrO_3$ (PZ) and $PbTiO_3$ (PT) sols are obtained by reactive dissolution of lead acetate in respective butoxides, dissolved in butanol, with a partial elimination of butyl-acetate.

One of the differences between PZ and PT sols is in the acetate content; about 75 % of the initial amount of acetate groups is still present in the PZ sol, while the amount of acetate groups in the PT sol is only about 50 %.

Table 5.1-2 presents a summary of EXAFS results from the present work and selected literature on PZ and PT sols and dried powders.

EXAFS analysis of the PZ sol shows that Pb is linked to about two Zr atoms and Zr is linked to about two Pb atoms, which means that the Pb-Zr correlations are in a 1:1 stoichiometry (Tables 4.1-2, 4.1-3). A high coordination number of Zr, about eight, and a relatively large number of Zr-Zr correlations, about six, suggest the formation of Zr oxoalkoxides. In the transition from the sol to the amorphous powder the coordination number of Zr decreases from eight to seven and also the number of Zr-Zr correlations reduces from six to about five (Table 4.1-3). The large number of Zr neighbours suggests clustering of Zr species in the studied range of hydrolysis conditions.

EXAFS analysis of the PT sol prepared from lead acetate and titanium n-propoxide in 2-methoxyethanol revealed the existence of Pb-Ti correlations in a 1:1 ratio (Arcon *et al.*, 1998). There is no available data on titanium environment in a butoxide/butanol based PT sol. By EXAFS analysis of the dried lead titanate precursor prepared from lead acetate and titanium butoxide in n-butanol, Malic *et al.* (Malic *et al.*, 1997b) proposed a trimeric structure of titanium atoms analogous to the one determined in Ti n-butoxide (Babonneau *et al.*, 1988). In the cyclic trimer, Ti atoms are coordinated by about five O atoms in the first coordination shell and about two Ti atoms in the second coordination shell, and Pb atoms are bonded to Ti atoms via oxobridges. We believe that such oligomeric structure was formed already during the synthesis.

Table 5.1-2. Summary of the EXAFS results from the present work and literature of PZ and PT sols and dried powders.

	PZ	PT	Reference
Sol	CN_{Zr}=8, CN_{Pb}=2, 6x Zr-O-Zr, 2x Pb-O-Zr	/	Ion et al. 2008
Dried powder	CN_{Zr}=7, CN_{Pb}=2, 5x Zr-O-Zr, 1x Pb-O-Zr	CN_{Ti}=5, CN_{Pb}=2, 2x Ti-O-Ti, 1x Pb-O-Ti	PZ: Ion et al. 2008 PT : Malic et al. 1997b

The partial charge model was used to predict the stability of PZ and PT alkoxide-acetate based complexes during hydrolysis and condensation. Calculations were performed for the complexes which were hydrolysed with R_w = 2 and R_w = 4, corresponding to partially and fully hydrolysed products, respectively. Figure 5.1-1 presents the partial charges of zirconium and titanium atoms and OH groups in the partially or fully hydrolysed PZ and PT intermediate products depending on the extent of condensation. The partial charge of Zr in the partially hydrolysed PZ product, equal to 0.7038, is 6 % higher than that of Ti in corresponding PT sample, which means that the former is more reactive. We observe that the difference in partial charges of Zr and Ti atoms in PZ and PT samples is larger than the difference between the partial charges in corresponding butoxides (Table 5.1-1). The partial charges of the OH groups are similar in all cases, with values between - 0.3 and - 0.2. Therefore the OH groups are nucleophilic enough to initiate further condensation. We assume that condensation stops predominantly due to the steric hindrance.

The situation is different for Ti and Zr hydrolysed species in water: the partial charges of OH groups in $(Ti(OH)_2(OH_2)_4)^{2+}$ and $(Zr(OH)_2(OH_2)_6)^{2+}$ are - 0.01 and - 0.07, respectively. The nucleophilic power of OH groups in $(Ti(OH)_2(OH_2)_4)^{2+}$ is close to 0, therefore the condensation is inhibited, while in $(Zr(OH)_2(OH2)_6)^{2+}$, the OH groups are nucleophilic enough to initiate further condensation (Livage et al., 1988).

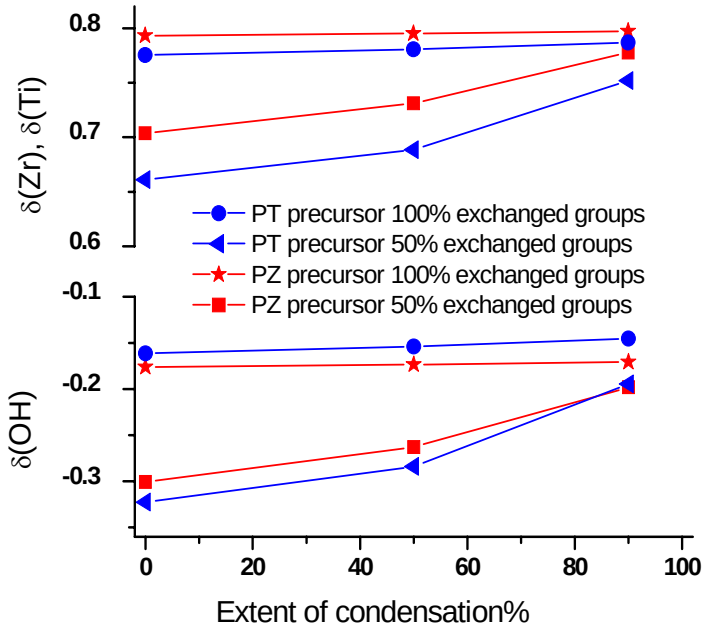

Figure 5.1-1. Partial charges of Zr and Ti and OH groups contained by the complex species of PZ and PT n-butoxide-based precursor during the condensation reaction. The lines are guide to the eye.

The study of the PZ and PT sols, hydrolysed with R_w 15 in alkaline medium (0.02 M, PZ_d10 and PT_d10), revealed that the surface charge of the particles after hydrolysis is close to the isoelectric point in both cases. We determined by PCS that PZ and PT samples are composed of about 100 nm sized particles, which are the building blocks of agglomerates of about 400 nm for PZ and about 500 nm for PT (Table 4.1-6, Table 4.2-3).

The sedimentation curves of the PZ and PT samples are plotted in Figure 5.1-2. We observe a small difference in their sedimentation fronts: PT sediment deposition is slightly faster than the PZ deposition, in agreement with the results of PCS: the larger the agglomerates, the faster the deposition. PZ_d10 compacts more efficiently than PT_d10 with almost 5 % higher volume shrinkage.

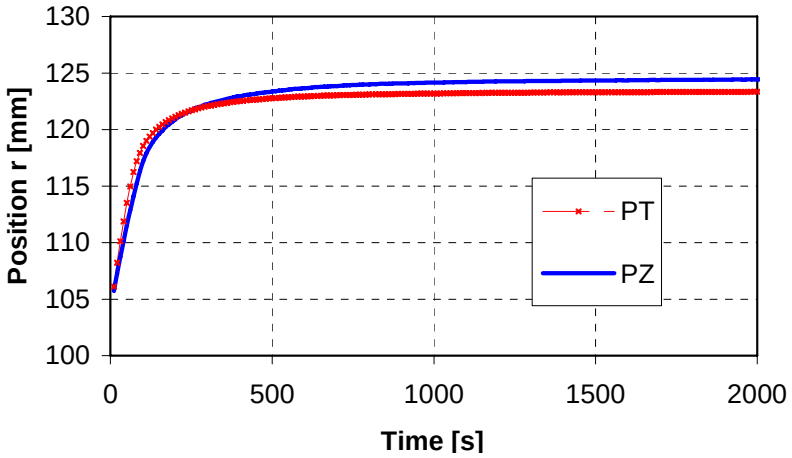

Figure 5.1-2. Sedimentation curve recorded by centrifuging under 1000 rpm of PZ_d10 and PT_d10 hydrolysis product.

Figure 5.1-3 presents the SEM images of a few drops of PZ_d10 and PT_d10 samples after solvent evaporation. The PZ_d10 fragments are composed of tiny fibres connected in a dense network, while the PT_d10 is composed of a very porous network of small particles. The dense arrangement of PZ fibres explains the larger shrinkage of the PZ_d10 sample in comparison to PT_d10.

The dried powder, prepared from the 0.02M PZ sol has a low SSA, equal to 4.7 m^2 / g, corresponding to d_{BET} of about 400 nm, while the SSA of PT is about twenty times higher, with the d_{BET} of about 20 nm (Table 4.2-6).

The SSA and morphology of the dried PZ powders, obtained by hydrolysing the 0.2 M sol, strongly depend on the hydrolysis conditions. Dense gel fragments with a low SSA of 0.53 m^2 / g are obtained at R_w = 2, while by increasing the R_w to 15, the powder is composed of porous fragments and has a high SSA of 118.41 m^2 / g. At R_w 15 and at pH 11, the powder consists of porous fragments and particles, and the SSA is 178.13 m^2 / g (Figure 4.1-10, Table 4.1-8).

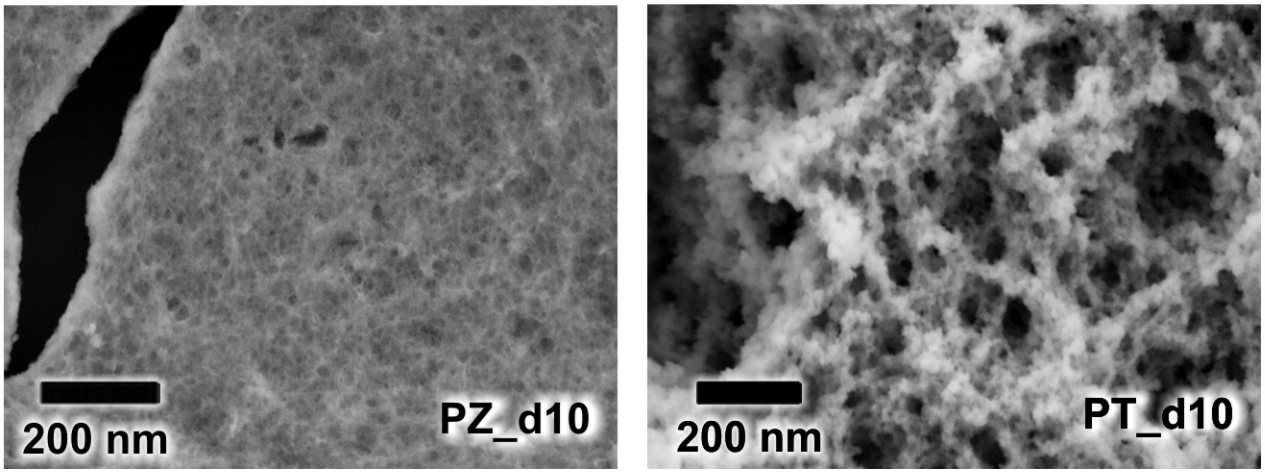

Figure 5.1-3. SEM images of a few drops of PZ_d10 and PT_d10 hydrolysis products spread on a substrate, after the evaporation of the solvent.

A different behaviour was observed in the dried PT powders, where the morphology only slightly depended on the hydrolysis conditions; loosely connected particles were obtained in all cases (Figure 4.2-5).

We can conclude that the PZ and PT sols have different structures and different reactivities; consequently they follow different hydrolysis and condensation pathways which results in different morphologies of the powders. A strong impact of the hydrolysis conditions is observed for PZ but not for PT.

The impact of the powder morphology on the homogeneity during heating is assessed next. The total mass losses of PZ and PT dried powders upon heating are about 16 % and 12 %, respectively.

Figure 5.1-4 presents a summary of mass losses of PZ and PT dried powders, prepared at different hydrolysis conditions (in neutral medium: R_w2, R_w5, R_w15 and in alkaline medium: $11R_w15$), in selected temperature ranges. The evolved gases, corresponding to the mass losses in different temperature ranges during thermal decomposition, are marked on the graphs.

In the 25-220 °C range the water evolves from all samples. The mass losses of PZ samples are higher than those of PT at all hydrolysis conditions, between 5-6 % and 3-4 %, respectively. In the range 220 - 400 °C water, acetone and carbon dioxide are evolved for all investigated samples. The mass loss of PZ increases with increasing R_w from 8.5 % to about 11 %, while in the case of PT it is 8.5-9 % for all R_w.

Between 400 °C and 640 °C, the mass loss of about 3 % and 0.5 %, observed only in the PZ samples prepared at $R_w = 2$ and 5, respectively, is accompanied by carbon dioxide evolution.

We connect different decompositions of PZ samples to their morphologies. In dense gel fragments characteristic for PZ prepared at $R_w = 2$ and 5, the alkoxide and acetate groups decompose between 220 and 400 °C with intermediate carbonaceous residues. Consequently lead segregates in a locally reducing atmosphere as determined by XRD (Figure 4.1-14). The porous morphology of PZ precursors prepared at $R_w = 15$ facilitates the oxidation of organic groups and in this case the homogeneity is retained on the level of XRD.

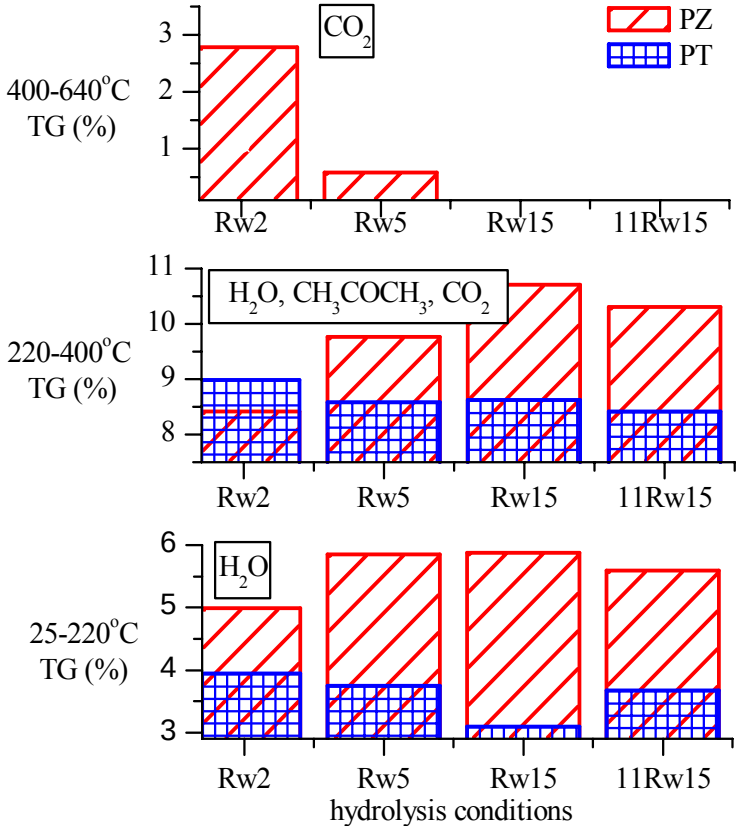

Figure 5.1-4. The mass losses of PZ and PT precursor powders prepared at different hydrolysis conditions (in neutral medium: R_w2, R_w5, R_w15 and in alkaline medium: $11R_w15$) in different temperature ranges. The evolved gasses in the investigated temperature range

EXAFS analysis of the PZ powder heated at 400 °C / 1h shows that the Pb-Zr correlation determined in the dried powder is completely lost, while the Zr-Zr correlations remain unchanged. In PZ there are no links between A and B- site cations. To regain the homogeneity during crystallization into the desired perovskite phase, the species must react by a solid state reaction.

There is no literature data on Ti environment in PT powder similar to ours, except Sengupta's report on EXAFS study of PT amorphous gel, prepared from Pb acetate and Ti isopropoxide in 2-methoxyethanol, and heated at 375 °C, which shows that there are no Pb-Ti correlations (Sengupta *et al.*, 1995). It should be noted that the authors did not analyse the sol or the precursor powder heated at a lower temperature.

The major phases identified in PZ and PT powders, prepared under different hydrolysis conditions and heated at selected temperatures, are presented in Table 5.1-3. The PZ powders, heated at 460°C, are amorphous or with presence of metallic lead, depending on hydrolysis conditions. At 500 °C they crystallize in pyrochlore phase and transform to perovskite phase at 700 °C.

The pyrochlore phase formation is predominantly related to the solution synthesis route. The PT powders crystallize directly in perovskite phase without any intermediate phase, in agreement with literature (Merkle *et al.*, 1998; Polli *et al.*, 2000). The pyrochlore phase is typical predominantly for PZ or Zr-rich PZT precursors and since a pronounced homocondensation is typical for Zr species, we can assume that Zr-Zr links, which are stable also at 400 ^{o}C, are the reason for the persistence of the transitory pyrochlore-type phase upon thermal treatment.

PT usually crystallizes upon heating at about 500 ^{o}C, which is about 200 ^{o}C lower than PZ. The melting points of PT and PZ are 1285 ^{o}C and 1570 ^{o}C, respectively (Jaffe *et al.* 1971). Chandratreya *et al.* found that enthalpy of the perovskite formation from constituent oxides is endothermic for PZ and exothermic for PT (Chandratreya *et al.*, 1981).

Table 5.1-3. Major phases in PZ and PT powders prepared under different hydrolysis conditions and heated at selected temperatures identified by XRD.

Hydrolysis conditions	PZ			PT	
	460^{o}C	500^{o}C/1h	700^{o}C/1h	500 ^{o}C / 1h	700 ^{o}C / 1h
R_w2	Am+Pb	Py	PE	PE	PE
R_w5	Am	Py	PE	PE	PE
R_w15	Am	Py	PE	PE	PE
11 R_w15	Am	Py	PE	PE	PE

Table 5.1-4 summarises the morphology of PZ and PT powders prepared with different hydrolysis conditions and heated at 700^{o}C. We observe that the powders preserve the morphology obtained upon drying: dense gel fragments at low R_w or porous fragments prepared at high R_w for PZ, and agglomerated particles in PT notwithstanding the hydrolysis conditions. Densification or particle growth takes place in all powders, which reflects in the decrease of the SSA upon heating (Table 4.1-13-15, Table 4.2-8).

Table 5.1-4. Summary of the morphology of PZ and PT powders, prepared with different hydrolysis conditions, and heated to 700 ^{o}C / 1h.

Hydrolysis conditions	PZ	PT
R_w2	Dense gel fragments	Agglomerated particles
R_w5	Gel fragments with low porosity	Agglomerated particles
R_w15	Porous gel fragments	Agglomerated particles
11 R_w15	Strongly agglomerated particles	Agglomerated particles

In Table 5.1-5 we summarise selected characteristics of PZ and PT sols, dried and heated powders. We observe a strong impact of the B-site cation on morphology of PZ and PT powders. The differences could stem from different condensation pathways of the hydrolysed species, which then result in different morphologies.

Beside the choice of the catalyst, the three condensation pathways, alcoxolation, oxolation and olation, have a strong impact on the morphology of the final product: olation results in dense, and oxolation in microporous structures, respectively (Henry 1998).

In our case, the inherent differences between Zr and Ti can lead to different condensation pathways in PZ and PT sols. Since solvent molecules contribute to the coordination expansion of Zr in PZ sol, we expect that olation, which yields dense structures, is a more probable condensation pathway than alcoxolation or oxolation.

In the PT sol, the trimers consisting of three Ti atoms linked by bridging alkoxide groups condense by alcoxolation or oxolation, depending on the R_w. The latter, as written above, yields microporous structures.

PZ sol contains more acetate groups than PT sol, as concluded from the NMR of the distillates. The analysis revealed that about 25 % and 50 % of acetates were removed by distillation of PZ and PT sol, respectively. The presence of bridging acetate groups in the dried powders has been also confirmed by FTIR (Figure 4.1-15, Figure 4.2-8). The acetate ligands are not sensitive to hydrolysis and are often used as alkoxide modifiers. Zr oxoalkoxides confirmed by EXAFS (Table 4.1-2) are formed during the sol synthesis by the ether elimination, therefore reducing the fraction of alkoxide groups bonded to the Zr atoms We assume that a larger fraction of acetates, and consequently a lower fraction of alkoxide groups, in the PZ sol as compared to PT may slow down the hydrolysis and therefore favour condensation (Brinker *et al.* 1990).

Table 5.1-5. Summary of selected characteristics of PZ and PT sols and of dried and heated powders.

	PZ	PT
Sol	-High amount of organics (75% of acetate groups) -2x Pb-O-Zr, 6x Zr-O-Zr	-High amount of organics (50% of acetate groups) - /
Hydrolysis product	400 nm agglomerates of 120 nm building blocks, connected in a dense network.	500 nm agglomerates of 90 nm building blocks, connected in a porous network.
Dried powder	-Strong impact of the hydrolysis conditions on powder morphology: dense fragments at low R_w, porous fragments at high R_w, emphasized by the increase of pH -1x Pb-O-Zr, 5x Zr-O-Zr	-Weak impact of the hydrolysis conditions on powder morphology: agglomerated particles at all investigated R_w and pH. - /
Powder heated at 400 ^oC	Homogeneity at atomic level is lost although the powder is homogeneous according to XRD.	- /
Crystalline powder	-Strong impact of the hydrolysis conditions on powder morphology is preserved from the dried powder.	-Weak impact of the hydrolysis conditions on powder morphology is preserved from the dried powder.

5.2 Local environment of Zr in $PbZrO_3$ and $La_2Zr_2O_7$ precursors

In this part we compare local environments of Zr along the $PbZrO_3$ (PZ) and $La_2Zr_2O_7$ (LZ) synthesis pathways.

In the synthesis of PZ, the reaction between acetate and butoxide results in the formation of an oxygen bridge between the Pb and Zr (Eq. 4.1-1, Eq. 4.1-2). EXAFS analysis of the sol revealed that each Pb atom is connected through an oxygen bridge to two Zr atoms and Zr atom is connected through an oxygen bridge to two Pb atoms (Table 4.1-1, Table 4.1-2). Upon hydrolysis and drying only one Pb-Zr link is preserved, and in the powder heated at 400 ^oC the correlation between Pb and Zr is completely lost.

In the synthesis of LZ, a reaction between La nitrate and Zr butoxide with the formation of an oxygen bridge between La and Zr was expected. However, the La L_3-edge EXAFS analysis reveals that the lanthanum environment is very similar to that of lanthanum in the nitrate, so we concluded that no connection between La and Zr was established during the sol synthesis (Table 4.3-1; Table 4.3-2). No link between La and Zr was determined in the dried powder or in the powder heated at 500 ^oC.

Table 5.2-1 presents a summary of Zr-K EXAFS analyses of the PZ and LZ sols, dried powders and the powders heated at 400 ^oC and 500 ^oC, respectively.

The local environment of zirconium in PZ sol is composed of about eight O atoms distributed between 2.10 Å and 2.25 Å. At larger distances about one C atom is found. About six Zr are present at 3.49 Å and two Pb neighbours, distributed at 3.45 Å and 3.58 Å. In the transition from the sol to the dried powder, the Zr coordination is reduced from about eight to seven, the distance Zr-Zr is 0.3 Å shorter than in the sol, the number of Zr-Zr correlations is reduced to about five, and one Zr-Pb link is lost. Upon increasing the heating temperature, the O, C and Zr shells remain almost the same; only the Zr-Pb correlation is completely lost.

The local environment of Zr atoms in the LZ sol is described by about seven O atoms at 2.12 Å, two C at 2.73 Å and six Zr atoms at 3.42 Å. The local environment of Zr of the dried LZ powder is similar: seven O at 2.12 Å, two C atoms at 2.71 Å and six Zr at 3.40 Å. The analysis of the LZ heated at 500 ^oC reveals that the Zr neighbourhood is composed of six O at 2.09 Å, two C at 2.71 and six Zr at 3.37 Å, which is slightly shorter than Zr-Zr distance in the sol and dried powder.

In both cases the Zr environment is similar and follows a similar evolution in the transition from the sol to amorphous powders. Zr oxo-alkoxide complexes form during the synthesis both in PZ and in LZ independent of the synthesis conditions. The as-formed Zr-O-Zr links persist upon further drying and heating, as evidenced by the EXAFS results. To obtain the final product, lead or lanthanum zirconate, the reaction between individual metal compounds takes place as a solid-state reaction upon heating.

Table 5.2-1. Zr neighbours (number, element) at selected distances obtained from Zr-K EXAFS results at different stages of the evolution from the sol to the amorphous powders in PZ and LZ.

		2.09 – 2.25 Å	2.60 - 2.75 Å	3.37 - 3.58 Å
Zr in PZ	Sol	~ 8 O	~ 1 C	~ 6 Zr + ~ 2 Pb
	Dried	~ 7 O	~ 1 C	~ 5 Zr + ~ 1 Pb
	400°C	~ 7 O	~ 1 C	~ 5 Zr
Zr in LZ	Sol	~ 7 O	~ 2 C	~ 6 Zr
	Dried	~ 7 O	~ 2 C	~ 6 Zr
	500°C	~ 6 O	~ 2 C	~ 6 Zr

5.3 Summary

The study of $PbZrO_3$ (PZ), $PbTiO_3$ (PT) and $La_2Zr_2O_7$ (LZ) prepared by alkoxide sol-gel synthesis is described.

The first aim was to understand the correlations between the hydrolysis conditions, morphology and homogeneity of PZ and PT.

The partial charge of Zr in the partially hydrolysed PZ product is higher than that of Ti in corresponding PT sample, which means that the former is more reactive. The partial charges of OH groups are similar in all cases, with negative values; therefore the OH groups are nucleophilic enough to initiate further condensation. We assume that condensation stops predominantly due to the steric hindrance.

Dried PZ powder consists of dense gel fragments with specific surface area (SSA) of 0.53 m^2 / g, corresponding to particles with a d_{BET} = 3760 nm when hydrolysed at R_w = 2. By increasing the R_w to 15 the powder is composed of porous fragments with SSA= 118.41 m^2 / g and a corresponding d_{BET} of 16 nm. The highest SSA of 178 m^2 / g (d_{BET} = 11 nm) is achieved when hydrolysis is performed at R_w = 15 and in alkaline medium.

The PZ powders, prepared at R_w = 2 and 5, decompose upon heating with intermediate carbonaceous residues forming a locally reducing atmosphere, resulting in a partial lead segregation from the amorphous matrix at 460 °C. The porous structure of the precursors prepared at R_w = 15 facilitates the oxidation of organic groups, we observe no segregation of lead.

The morphology of the dried powder is retained upon heating at 700 °C, when powders prepared under all hydrolysis conditions crystallize in perovskite phase with traces of pyrochlore-type phase. Agglomerated particles of about 60 nm are obtained at R_w = 15 and alkaline pH.

The dried PT powder obtained at R_w = 15 and alkaline pH is composed of a porous network of 8 nm particles. The morphology of PT powders is not influenced by the hydrolysis conditions.

The decomposition of organic groups in PT dried powders upon heating occurs in a single step between 220 °C and 400 °C. The powders crystallize in perovskite phase at 500 °C. They are composed of agglomerates of particles of about 50 nm under all hydrolysis conditions.

The decomposition of the LZ sol starts with a strongly exothermic reaction between the nitrates and the organic groups. The nitrates act as an oxidizing agent for the organic groups of the precursor and enable their removal. During exothermic decomposition of nitrate and organic groups, the temperature increases locally to higher values than the drying temperature, promoting formation of carbonate species. The powder crystallizes after heating at 800 °C / 1h in pure pyrochlore phase. The powder heat treated at 900 °C for 1 h is composed of friable agglomerates of about 70-nm-sized nanoparticles. The ceramics obtained from the powder milled in acetone for 30 minutes has 97.9 % relative density after heating at 1400 °C for 10 h under atmospheric pressure, which is well below the usually reported temperatures for atmospheric sintering of this material.

A further aim of this work was to investigate the structural evolution from the sol to the amorphous dried and heat treated PZ and LZ powders.

In the PZ sol, the lead environment is dominated by two Pb-O-Zr links, while the initial dimeric Zr n-butoxide results during thermolysis in Zr oxo-alkoxide complex, where the Zr environment is populated by six Zr-O-Zr links. A reaction takes place between lead and zirconium species leading to a complex, most probably with a homogenous distribution of the Pb-O-Zr and Zr-O-Zr links.

After hydrolysis of the sol, one of the two Pb-O-Zr links is retained while the Zr - Zr correlations are retained regardless the hydrolysis conditions.

In the powder heated at 400 °C / 1h there is no Pb-Zr correlation, while the Zr-Zr correlations remain

almost unchanged. Atomic homogeneity is partially lost in the process of hydrolysis and condensation and completely upon heating.

The lanthanum environment in lanthanum nitrate sol and LZ sol is similar to that in lanthanum nitrate hydrate. The local environment of lanthanum in the dried powder resembles to the lanthanum nitrate and lanthanum carbonate.

The Zr environment in LZ sol is populated by six Zr-O-Zr links and it remains almost unchanged in the transition from the sol to the dried and heated powder. The Zr species form polynuclear oxo-alkoxide complexes by thermolysis in the course of the synthesis of the sol. No links between La and Zr species are formed.

Both in PZ and LZ systems, the Zr environment is similar and follows a similar evolution in the transition from the sol to amorphous powders. Zr oxo-alkoxide complexes form during the synthesis both in PZ and in LZ independent of the synthesis conditions. The as-formed Zr-O-Zr links persist upon further drying and heating, as evidenced by the EXAFS results. To obtain the final product, lead or lanthanum zirconate, the reaction between individual components takes place as a solid-state reaction upon heating.

6 Acknowledgements

Here I would like to thank most sincerely to all the people who contributed in the realisation of this research work and especially to:

Prof. Dr. Marija Kosec, head of Electronic Ceramics Department (K5), Jožef Stefan Institute, for giving me the opportunity to pursue my PhD at Jožef Stefan International Postgraduate School with the financial support of EU Centre of Excellence SICER (G1MA-CT-2002-04029) and Slovenian Research Agency (P2-105),

Asst. Prof. Dr. Barbara Malič, the supervisor of my thesis, for her continual and valuable guidance along this work, for encouragements, support, endless patience and help in correction of the thesis manuscript,

Prof. Dr. Iztok Arčon (University of Nova Gorica), the co-supervisor of my thesis, for his patience in introducing me into the field of XAFS and especially to the EXAFS analysis, for fruitful discussions and guidance in my work,

Prof. Dr. Alojz Kodre (Faculty of Mathematics, University of Ljubljana) and Prof. Jana Padežnik Gomilšek (Faculty of Mechanical Engineering, University of Maribor), for interesting discussions and wonderful time spent during EXAFS measurements,

Dr. Paul Bowen (Powder Technology Laboratory, EPFL, Lausanne), for being his guest during one-month scientific exchange (STSM – COST 539 – 01864), for his advices in my work and encouragements and to the staff of the same laboratory for help in experimental work,

Dr. Stojan Stavber (Department of Physical and Organic Chemistry, Jožef Stefan Institute), for NMR analysis,

Dr. Bojan Budič (National Institute of Chemistry, Ljubljana), for ICP-AES analysis,

Prof. Dr. Primož Šegedin and Dr. Bojan Kozlevčar (Faculty of Chemistry, University of Ljubljana), for fruitful discussion and help in IR spectra acquisition, respectively.

Jena Cilenšek and Silvo Drnovšek (K5) for help in the experimental work,

Dr. Marijan Bele, Milena Zorko and Gregor Kapun (National Institute of Chemistry, Ljubljana) for advices in handling the FE-SEM,

My colleagues from the K5 department,

My family and my friends.

7 References

Arcon, I., B. Malic, et al. (1998). "*Study of the lead environment in liquid and as-dried precursor of PZ, PT, PZT thin films*." J. Sol-Gel Sci. Tech. **13:** 861-864.

Babonneau, F., S. Doeuff, et al. (1988). "*XANES and EXAFS study of titanium alkoxides.*" Inorg. Chem. **27:** 3166-3172.

Baythoun, M. S. G. and F. R. Sale (1982). "*Production of strontium-substituted lanthanum manganite perovskite powder by the amorphous citrate proce*ss." J. Mater. Sci. **17:** 2757-2769.

Bolech, M., E. H. P. Cordfunke, et al. (1997). "*The heat capacity and derived thermodynamic functions of $La_2Zr_2O_7$ and $Ce_2Zr_2O_7$ from 4 to 1000 K.*" J. Phys. Chem. Solids **58**(3)**:** 433-439.

Bradley, D. C., R. C. Mehrotra, et al. (1978). *Metal Alkoxides*. London: Academic Press.

Brinker C. J. and G. W. Scherer (1990). *Sol-Gel Science, the physics and chemistry of sol-gel processing*. New York: Academic Press.

Budd, K. D., K. S. Dey, et al. (1985). "*Sol-gel processing of $PbTiO_3$, $PbZrO_3$, PZT, and PLZT thin films.*" Proc. Br. Ceram. Soc. **36:** 107-121.

Campion, J.-F., D. A. Payne, et al. (1991). "*Synthesis of bimetallic barium titanium alkoxide as precursors for electrical ceramics. Molecular structure of the new barium titanium oxide alkoxide $Ba_4Ti_{13}(\mu_3\text{-}O)_{12}(\mu_5\text{-}O)_6(\mu_1\text{-}\eta^1\text{-}OCH_2CH_2OCH_3)_{12}(\mu_1,\mu_3\text{-}\eta^2\text{-}OCH_2CH_2OCH_3)_{12}$.*" Inorg. Chem. **30:** 3244-3245.

Cao, X.Q., R.Vassen, et al. (2004). "*Ceramic materials for thermal barrier coatings.*" J. Eur. Ceram. Soc. **24:** 1-10.

Cakare, L., M. Kosec, et al. (2000). "*Sol-Gel Processing of $PbZrO_3$ thin films.*" J. Sol-Gel Sci. Techn. **19:** 603–606.

Chandler, C. D., C. Roger, et al. (1993). "*Chemical aspects of solution routes to perovskite-phase mixed-metal oxides from metal-organic precursors.*" Chem. Rev. **93:** 1205-1241.

Chandratreya, S. S., R. M. Fulrath, et al. (1981). "*Reaction mechanisms in the formation of PZT solid solutions.*" J. Am. Ceram. Soc. **64:** 422-425.

Chen, D. and R. Xu (1998). "*Hydrothermal synthesis and characterization of $La_2M_2O_7$ (M = Ti, Zr) powders.*" Mater Res. Bull. **33:** 409-417.

Coffman, P. R., S. K. Barlingay, et al. (1996). "*Structure evolution in the $PbO\text{-}ZrO_2\text{-}TiO_2$ sol-gel system: part II – pyrolysis of acid and base-catalyzed bulk and thin film gels.*" J. Sol-Gel Sci. Techn. **6:** 83-106.

CRC Handbook of Chemistry and Physics, 88th Edition (Internet Version 2008), David R. Lide, editor. Boca Raton, FL: CRC Press/Taylor and Francis.

Dey, K. S., K. D. Budd, et al. (1987). "*Structure of polymeric $PbTiO_3$ gels.*" J. Am. Ceram. Soc. **70:** C-295-C-296.

Day, V. W., T. A. Eberspacher, et al. (1993). "*Dodecatitanates: a new family of stable polyoxotitanates*." J. Am. Chem. Soc. **115:** 8469-8410.

Feth, M. P., A. Weber, et al. (2003). "*Investigation of the crystallization behaviour of lead titanate (PT), lead zirconate (PZ), lead zirconate titanate (PZT) by EXAFS–spectroscopy and X-ray diffraction.*" J. Sol-Gel Sci. Tech. **27:** 193-204.

Gatehouse, B. M., S. E. Livingstone, et al. (1957). "*Infrared spectra of some nitrato-co-ordination complexes.*" J. Chem. Soc. **1957:** 4222-4225.

Gatehouse, B. M., S. E. Livingstone, et al. R.S. (1958). "*The infrared spectra of some simple and complex carbonates.*" J. Chem. Soc. **1958:** 3137-3142.

Gmehling, J., J. Menke, et al. (2008). "*Azeotropic data for binary mixtures.*" **6:** 155-173 in CRC Handbook of Chemistry and Physics, 88th Edition (Internet Version 2008), David R. Lide, editor. Boca Raton, FL: CRC Press/Taylor and Francis. See also: http://www.hbcpnetbase.com/.

Gobichon, A. E., M. Louer, et al. (1996). "*Structure determination of two polymorphic phases of*

$La(NO_3)_3 \cdot 4H_2O$ from X-ray powder diffraction." J. Solid State Chem. **126:** 127-134.

Gobichon, A. E., J. P. Auffredic, et al. (1997). "*Thermal decomposition of neutral and basic lanthanum nitrates studied with temperature dependent powder diffraction and thermogravimetric analysis.*" Solid State Ionics **93:** 51-64.

Guha, C., J. M. Chakraborty, et al. (2003). "*The structure and thermodynamics of ion association and solvation of some thiocyanates and nitrates in 2-methoxyethanol studied by conductometry and FTIR spectroscopy.*" J. Phys. Chem. **B:** 12814-12819.

Gurkovich, S. R., J. B. Blum (1984). *Preparation of monolithic $PbTiO_3$ by a sol-gel process.* In: Hench, L.L., Ulrich D.R., editors. Ultrastructure processing of ceramics, glasses and composites. New York: John Wiley and Sons. p. 152 – 160.

He, X., Y. Thomann, et al. (2006). "*Iridescent colors from films made of polymeric core-shell particles.*" Polymer Bulletin **57:** 785–796.

Hench, L. L. and J. K. West (1990). "*The sol-gel process.*" Chem. Rev. **90:** 33-72.

Henry, M. (1998). "*Retrosynthesis in inorganic crystal structures: application to nesosilicate and inosilicate networks.*" Coord. Chem. Rev. **178-180:** 1109-1163.

Hubert-Pfalzgraf, L. G., S. Daniele, et al. (1997). "*Solution routes to lead titanate: synthesis, molecular structure and reactivity of the Pb–Ti and Pb–Zr species formed between various lead oxide precursors and titanium or zirconium alkoxides. Molecular structure of $Pb_2Ti_2(\mu_4\text{-}O)(OAc)_2(OPr^i)_8$ and of $PbZr_3(\mu_4\text{-}O)(OAc)_2(OPr^i)_{10}$.*" J. Mater. Chem. **7:** 753–762.

Jaffe, B., W. R. Cook Jr., H. Jaffe (1971). Piezoelectric Ceramics. London: Academic Press.

JCPDS data file no. 87-0570 ($PbZrO_3$).

JCPDS data file no. 78-0298 ($PbTiO_3$).

JCPDS data file no. 73-0444 ($La_2Zr_2O_7$).

JCPDS data file no. 65-2873 (Pb).

Ion, E. D., B. Malic, et al. (2007a). "*Characterization of $PbZrO_3$ prepared using an alkoxide-based sol–gel synthesis route with different hydrolysis conditions*." J. Eur. Cer. Soc. **27:** 4349-4352.

Ion, E. D., B. Malic, et al. (2007b). "*Lanthanum zirconate nanoparticles and ceramics by nitrate-modified alkoxide synthesis route.*" J. Sol-Gel Sci. Tech. **44:** 203-209.

Ion, E. D., B. Malic, et al. (2008). "*Structural evolution from the sol to the $PbZrO_3$ (PZ) precursor powders prepared by an alkoxide-based sol-gel route.*" J. Sol-Gel Sci. Tech. **45**: 213-218.

Kido, H., S. Komarneni, et al. (1991). "*Preparation of $La_2Zr_2O_7$ by sol-gel route.*" J. Am. Ceram. Soc. **74:** 422-24.

Klingenberg, B., M. A. Vannice (1996). "*Influence of Pre-treatment on Lanthanum nitrate, Carbonate, and Oxide Powders.*" Chem. Mater. **8:** 2755-2768.

Kodre, A., I. Arcon, et al. (1994). "*Double photoexcitation [2(s,p)4(p,d)] in the Xe-isoelectronic series Cs^+, Ba^{2+}, La^{3+}.*" J. Phys. IV **4:** 397-400.

Kolar, D. (1993). Tehnična keramika (Technical Ceramics), Zavod Republike Slovenije za šolstvo in šport, Ljubljana, p. 110.

Kosec, M. and B. Malic (1994). *Chemical homogeneity and morphology of alkoxide-derived PZT powders.* In: Waser R. and Hoffmann S., editors. Proc. Electroceramics IV, vol. 2. Aachen: Augustinus Buchhandlung. p. 1245-1250.

Kosec, M. and B. Malic (1995). *Sol-gel synthesis and sintering of PZT based powders.* In: Gusmano, G., Traversa, E., editors. Fourth Euro Ceramics vol. 5. Faenza: Gruppo editoriale Faenza Editrice. p. 9-16.

Kuscer, D., J. Holc, et al. (1995). "*Interactions between a thick film $LaMnO_3$ cathode and YSZ SOFC electrolyte during high temperature ageing.*" Solid State Ionics **78:** 79-85.

Kuscer, D., J. Holc, et al. (2001). "*Correlation between the defect structure, conductivity and chemical stability of $La_{1-y}Sr_yFe_{1-x}Al_xO_{3-\delta}$ cathodes for SOFC.*" J. Eur. Ceram. Soc. **21:** 1871-1820**.**

Kuhn, L. P. and R. A. Wires (1963). "*The hydrogen Bond. VI. Equilibrium between hydrogen bonded and nonbonded conformation of α, ω–diol monomethyl ethers.*" J. Am. Chem. Soc. **86:** 2161-2165.

Labrincha, J. A., J. R. Frade, et al. (1993). "*$La_2Zr_2O_7$ formed at ceramic electrode/YSZ contacts.*" J. Mat. Sci. **28:** 3809-3815.

Lakeman, C. D. E., Z. Xu, et al. (1995). "*On the evolution of structure and composition in sol-gel-derived lead zirconate titanate thin layers.*" J. Mater. Res. **8:** 2042-205.

Landillon V., D. Cassan, et al. (2008). "*Flowability, cohesive, and granulation properties of wheat powders.*" J. Food Eng. **86:** 178–193.

Lange, F. F. (2001). "*Shape forming of ceramic powders by manipulating the interparticles pair potential.*" Chem. Eng. Sci. **56:** 3011-3020.

Langford, J. (1992). *I. NIST Special Publication 846.* In: Prince E. and Stalick J. K., editors. Proceedings of the International Conference Accuracy in Powder Diffraction II, Gaitherburg, MD, May 26-29. p.110-126.

Livage, J., M. Henry, et al. (1988). "*Sol-gel chemistry of transition metal oxides.*" Prog. Solid St. Chem. **18:** 259-341.

Livage, J., M. Henry, et al. (1990). "*Chemical synthesis of fine powders.*" Mater. Res. Soc. Bull. **1:** 18-25.

Livage, J. (1998). "*Sol-gel synthesis of heterogeneous catalysts from aqueous solutions.*" Catalysis Today **41:** 3-19.

Luo, S., Z. Tang, et al. (2003). "*Low-temperature combustion synthesis and characterization of nanosized tetragonal barium titanate powders.*" Microel. Eng. **66:** 147-152.

Malic, B., M. Kosec (1992). *Analysis of the thermal decomposition of various Pb-Zr alkoxide derived precursors.* In: S. Amon and M. Kosec, editors. MIEL-SD'92 Proceedings, Ljubljana: MIDEM. p. 437-442.

Malic, B., M. Kosec, et al. (1995). "*Effect of precursor type on the decomposition of alkoxide derived lead zirconate.*" Silicates Industriels **60:** 163-166.

Malic, B., I. Arcon, et al. (1997a). "*A study of amorphous precursors for $PbZrO_3$-$PbTiO_3$ based ceramic materials.*" J. Sol-Gel Sci. Tech. **8:** 343-346.

Malic, B., I. Arcon, et al. (1997b). "*A structural study of amorphous alkoxide-derived lead titanium complexes.*" J. Mater. Res. **12:** 2602-2611.

Malic, B., I. Arcon, et al. (1999). "*EXAFS study of amorphous precursors for Pb(Zr, Ti)O_3 ceramics.*" J. Sol-Gel Sci. Tech. **16:** 135-141.

Malic, B., M. Kosec (2002). "*Solution synthesis of Pb(Zr, Ti)O_3 ceramic nano-powders.*" Inf. MIDEM **32:** 231-237.

Malic, B., M. Kosec, et al. (2005). "*Homogeneity issues in chemical solution deposition of Pb(Zr, Ti)O_3 thin films.*" J. Eur. Ceram. Soc. **25:** 2241-2246.

Malic, B., I. Arcon, et al. (2006). "*Homogeneity of Pb(Zr, Ti)O_3 thin films by chemical solution deposition: Extended x-ray absorption fine structure spectroscopy study of zirconium local environment.*" J. App. Physics **100:** 051612-1-8.

Masson, O., Peakoc, *Profile fitting computer program, version 0.51, February 2000*, SPTCS Limoges, France (olivier.masson@unilim.fr).

Matsumura, Y., M. Yoshinaka, et al. (1997). "*Formation and sintering of $La_2Zr_2O_7$ by the hydrazine method.*" Solid State Comm. **104:** 341-345**.**

Merkle, R. and H. Bertagnolli (1998). "*Investigation of the crystallization of lead titanate and lead zirconate titanate with x-ray diffraction and differential thermal analysis.*" Ber. Bunsenges. Phys. Chem. **102:** 1023-1031.

Morosin, B. (1977). "*Molecular configuration of tridecazirconium oxide-methoxide complex.*" Acta Cryst. B **33:** 303-305.

Nair, J., P. Nair, et al. (1999). "*Sintering of lanthanum zirconate.*" J. Am. Ceram. Soc. **82:** 2066-2072.

Nakamoto K. (1997). *Infrared and Raman Spectra of Inorganic and Coordination Compounds*, 5th ed., New York: John Wiley&Sons.

NIST (2005). NIST Mass Spec Data Center, S.E. Stein, director, "*Infrared Spectra*" in NIST Chemistry WebBook, NIST Standard Reference Database Number 69. P.J. Linstrom and W.G. Mallard, editors. National Institute of Standards and Technology, Gaithersburg MD, 20899 (http://webbook.nist.gov).

Noheda, B., J. A. Gonzalo, et al. (2000). "*Tetragonal-to-monoclinic phase transition in a ferroelectric perovskite: The structure of $PbZr_{0.52}Ti_{0.48}O_3$.*" Phys. Rev. B **61:** 8687-8695.

Ota, A., Y. Matsumura, et al. (1998). "*Formation and sintering of 8 mol % Y_2O_3-substituted $La_2Zr_2O_7$ by*

the hydrazine method." J. Mater. Sci. Lett. **17:** 199-201.

Patil, K. C., G. V. Chandrashekhar, et al. (1968). "*Infrared spectra and thermal decomposition of metal acetates and dicarboxylates.*" Can. J. Chem. **46:** 257-265.

Phase Diagrams for Ceramists, Fig. 05232 "*System ZrO_2-La_2O_3*". In: R. S. Roth, T. Negas, L.P. Cook, editors. The American Ceramic Society. Vol. 4. 1981. (after Rouanet, A., Rev. Int. Hautes Temp. Refract., 8 161-180, 1971, Foex, M. Rev. Int. Hautes Temp. Refract., 3 309-326 (1966). Cabannes, F., Simonato, J., Foex, M., and Coutures, J. P., High Temp. – High Pressures, 4 589-596 (1972). Foex, M., and Traverse, J. P., Rev. Int. Hautes Temp. Refract., 3 429-453 (1966)).

Peter, D., T. S. Ertel, et al. (1994). "*EXAFS study of zirconium alkoxides as precursor in the sol-gel process: I. Structure investigation of the pure alkoxides.*" J. Sol-Gel Sci. Tech. **3:** 91-99.

Polli, A. D. and F.F. Lange (1995). "*Pyrolysis of $Pb(Zr_{0.5}Ti_{0.5})O_3$ Precursors: avoiding lead partitioning.*" J. Am. Ceram. Soc. **78:** 3401-3404.

Polli, A. D., F. F Lange, et al. (2000). "*Metastability of the fluorite, pyrochlore and perovskite structure in the PbO-ZrO_2-TiO_2 system.*" J. Am. Ceram. Soc. **83:** 873-881.

Ravel, B. and M. Newville (2005). "*ATHENA, ARTEMIS, HEPHAESTUS: data analysis for X-ray absorption spectroscopy using IFEFFIT.*" J. Synchrotron Rad. **12:** 537-541.

Rao, K. K., T. Banu, et al. (2002). "*Preparation and characterization of bulk and nano particles of $La_2Zr_2O_7$ and $Nd_2Zr_2O_7$ by sol–gel method.*" Mater. Lett. **54:** 205-210.

Rehr, J. J., R. C. Albers, et al. (1992). "*High-order multiple-scattering calculations of x-ray-absorption fine structure.*" Phys. Rev. Lett. **69:** 3397-3400.

Sanchez, C., J. Livage, *et al.* (1988). "*Chemical modification of alkoxide precursor.*" J. Non-Cryst. Solids **100:** 65-76.

Schafer, J., W. Sigmund, et al. (1997). "*Low temperature synthesis of ultrafine $Pb(Zr,Ti)O_3$ powder by sol-gel combustion.*" J. Mat. Res. **12:** 2518-2521.

Schwartz, R. W. (1997). "*Chemical Solution Deposition of Perovskite Thin Films.*" Chem. Mater. **9:** 2325-2340.

Sengupta, S. S., L. Ma, et al. (1995). "*Extended x-ray absorption fine structure determination of local structure in sol-gel-derived lead titanate, lead zirconate, and lead zirconate titanate.*" J. Mater. Res. **10:** 1345-1348.

Sirio, C., L. G. Hubert-Pfalzgraf, et al. (1997). "*Facile thermal desolvation of $Ce_2(OPr^i)_8(Pr^iOH)_2$: Characterization and molecular structure of $Ce_4(\mu_4\text{-}O)(\mu_3\text{-}OPr^i)(\mu\text{-}OPr^i)_4(OPr^i)_8$.*" Polyhedron **16:** 1129-1136.

Slunecko, J., M. Kosec, et al. (1998). "*Morphology and crystallization behavior of sol–gel-derived titania.*" J. Am. Ceram. Soc. **81:** 1121–24.

Stewart, D. F. and W. W. Wendlandt (1959). "*The solubility and heat of solution of lanthanum nitrate 6-hydrate in non-aqueous solvents.*" J. Phys. Chem. **63:** 1330.

Shulman, G. P., M. Trusty, et al. (1963). "*Thermal decomposition of aluminium alkoxide.*" J. Org. Chem. **28:** 907-910.

Turova, N.Y., E.P. Turevskaya, et al. (2002). *The Chemistry of Metal Alkoxides*, Boston: Kluwer Academic.

Vioux, A. (1997). "*Nonhydrolytic sol-gel routes to oxides.*" Chem. Mater. **9:** 2292-2299.

Wang, H. W., D. A. Hall, et al. (1992). "*Phase homogeneity and segregation in PZT powders prepared by thermal decomposition of metal-EDTA complexes derived from nitrate and chloride solutions.*" J. Am. Ceram. Soc. **75:** 124-130.

Wang, H. W., D. A. Hall, et al. (1994). "*A thermoanalytical study of the metal nitrate-EDTA precursors for lead zirconate titanate ceramic powders.*" J. Thermal Anal. Calor. **41:** 605-620.

Wendlandt, W.W. (1956). "*The thermolysis of the rare earth and other metal nitrates.*" Anal. Chim Acta **15:** 435-439.

Wu, A., P. Vilarinho, et al. (2000). "*Sol–gel preparation of lead zirconate titanate powders and ceramics: effect of alkoxide stabilizers and lead precursors.*" J. Am. Ceram. Soc. **83:** 1379–1385.

Zhang, Q., R. Whatmore (1999). "*A comparison of the nanostructure of lead zirconate, lead titanate and lead zirconate titanate sols.*" J. Sol-Gel Sci. Tech. **15:** 13-22.

Zeng, X., Y. Liu, et al. (2002). "*Preparation of nanocrystalline $PbTiO_3$ by accelerated sol–gel process.*" Mat. Chem. and Phys. **77:** 209–214.

Zhou, H., D. Yi, et al. (2007). "*Preparation and thermophysical properties of CeO_2 doped $La_2Zr_2O_7$ ceramic for thermal barrier coatings.*" J. Alloy Comp. **438:** 217-221.

Yoldas, B. E. (1986a). "*Zirconium oxides formed by hydrolytic condensation of alkoxides and parameters that affect their morphology.*" J. Mater. Sci. **21:** 1080-1086.

Yoldas, B. E. (1986b). "*Hydrolysis of titanium alkoxide and effects of hydrolytic polycondensation parameters.*" J. Mater. Sci. **21:** 1087-1092.

8 Appendix

8.1 Partial charge model

Livage *et al.* (Livage *et al.*, 1988) developed a partial charge model which allows the prediction of chemical reactivity of any complex based on the partial charge distribution. When two atoms A and B combine, a partial electron transfer occurs so that each atom *i* acquires a positive or a negative partial charge δ_i.

The electronegativity of an atom in a molecule changes linearly with its charge (Eq. 8.1-1).

$$\chi_i = \chi_i^0 + k\sqrt{\chi_i^0}\,\delta_i \qquad \text{Eq. 8.1-1}$$

where: χ_i - the electronegativity of an atom *i* in a molecule,
χ_i^o - the electronegativity of the neutral atom,
k - a constant that depends on the electronegativity scale (k= 1.36 for Pauling's scale).

The charge transfer between atoms A and B stops when the electronegativities of the constituent atoms are equal to the mean electronegativity χ.

$$\chi = \frac{\Sigma_i \sqrt{\chi_i^0} + 1.36z}{\Sigma_i 1/\sqrt{\chi_i^o}} \qquad \text{Eq. 8.1-2}$$

where: *z* - the net charge of the molecular species.

The partial charge of an atom *i* in a molecule can be calculated as:

$$\delta_i = (\chi - \chi_i^0)/1.36\sqrt{\chi_i^0} \qquad \text{Eq. 8.1-3}$$

The partial charge model does not take into account the structure of the species, the resonance effects and π overlapping and it is difficult to account for coordination variation which may occur during a chemical reaction.

9 Index of Figures

10 Index of Tables

11 Personal bibliography

• Elena-Daniela Ion, Barbara Malic, Iztok Arcon, Alojz Kodre, Marija Kosec, Structural evolution from the sol to the $PbZrO_3$ precursor powders prepared by an alkoxide-based sol-gel route. Journal of Sol-Gel Science and Technology, (2008), 45, 213-218.

• Elena-Daniela Ion, Barbara Malic, Marija Kosec, Lanthanum zirconate nanoparticles and ceramics by nitrate-modified alkoxide synthesis route. Journal of Sol-Gel Science and Technology, (2007), 44, 203-209.

• Elena-Daniela Ion, Barbara Malic, Marija Kosec, Characterization of $PbZrO_3$ prepared using an alkoxide-based sol-gel synthesis route with different hydrolysis conditions. Journal of European Ceramic Society, (2007), 27, 4349 – 4352.

• L. Rosu, C.N. Cascaval, C. Ciobanu, D. Rosu, E. Ion, C. Morosanu, M. Enachescu, Effect of UV radiation on the semi-interpenetrating polymer networks based on polyutethane and epoxy-maleate of bisphenol A. Journal of Photochemistry and Photobiology A: Chemistry, (2004), 169, 177-185.

• E. Dimitriu, E. D. Ion, S. Constantinescu, M. N. Grecu, Eu-doped PT-type ceramics. I. Preparation and structural investigation. Ferroelectrics, (2003), 294, 85 – 92.

• R. Cristescu, G. Socol, I.N. Mihailescu, M. Popescu, F. Sava, E. Ion, C.O. Morosanu, I. Stamatin, New results in pulsed laser deposition of poly-methyl-methacrylate thin films. Applied Surface Science, (2003) 208-209, 645-650.